Università degli Studi di Pisa

Corso di Laurea Magistrale in Fisica

Tesi di Laurea Magistrale

Time resolved magneto-optical measurements of ultrafast demagnetization dynamics

Candidato **Martina Giovannella**

Relatori **Stefan Eisebitt**
Clemens von Korff Schmising
(TU Berlin)

Anno Accademico 2012/2013

Contents

Introduction

The availability of ultrashort pulsed laser source technology allows the investigation of dynamics in materials and the study of non equilibrium effects. At the moment, laser sources which provide tens or few hundreds of femotsecond laser pulses are commercially available. This pushes the investigation limit to the sub-ps range and gives access to the so called ultrafast dynamics. Investigation of ultrafast dynamics is applied to ferromagnetic metals in this thesis.

The common configuration to achieve this kind of investigation is the pump and probe technique. A femtosecond pump pulse triggers the dynamics and a femtosecond probe pulse allows to study the induced non-equilibrium effects. When applied to ferromagnetic metals, experimental results raised fundamental questions attracting the attention of the scientific community for over a decade.

In 1996 Beaurepaire et al. published a paper [1] which gained the attention of the ultrafast dynamics community. The magnetic material excited with a femtosecond laser source showed a reduction of the magnetization within the first picosecond and a subsequent recovery within a few picoseconds. It was the first time that the magnetic order was manipulated in the sub-ps range, in an all-optical process.

How fast can the magnetic order be manipulated? Which processes take place in the femtoseconds dynamics of a ferromagnetic metal? Which dissipation channel of angular momentum can lead to an ultrafast magnetization reduction?

There is a fundamental interest in giving answers to these questions, but there are also strong technology interests in the ultrafast manipulation of magnetic order. The first and wider application of magnetic material is magnetic data storage. The possibility to control the magnetic order through an applied magnetic field and the ability of these materials to keep their magnetization state under certain conditions led to the development of magnetic recording technology. In the present days, time scales for the process of reading and writing are in the nanoseconds range, but the possibility to reach a magnetization reversal of a bit in 200 ps has been shown [2]. The constant

progress of technology requires an evolution of magnetic data storage to higher density (smaller bits) and to faster manipulation. The latter goal does not seem reachable with the usual way of controlling magnetic materials, solely through an applied magnetic field. [3]

Despite of this fundamental and technology interest and the several theoretical and experimental efforts made in the last fifteen years to understand the ultrafast dynamics, a satisfying and complete model to describe it has not been developed yet. The main theoretical challenge is to describe the dissipation of angular momentum. In Chapter 1 the most important models developed to answer this quest are discussed.

The model which is considered to describe this process most successfully is the microscopic three temperature model (M3TM), by Koopmans et al. [4] [5] [6]. Within this model the lattice acts as an ultrafast dissipation channel for the angular momentum. The microscopic mechanism underlying the ultrafast demagnetization is considered to be the Elliott-Yafet spin flip electron phonon scattering. In this picture, a finite spin flip probability a_{sf} is associated to each electron phonon scattering event. With large enough a_{sf}, an ultrafast demagnetization can be achieved. The predictions of the model have been tested through experimental data.

There is no full agreement in the ultrafast magnetism community whether this effect alone can explain the ultrafast demagnetization process or not. For instance the calculations for a_{sf} available in literature disagree with each other. [6] [7]

In 2010 Battiato et al. introduced a model where superdiffusive spin transport is the responsible mechanism for ultrafast demagnetization [8]. The main effect behind this model is the spin dependent velocity and lifetime of excited electrons in ferromagnetic materials. The majority excited electrons have an higher mobility than minority ones and this causes a depletion of majority spins in the excited area and a magnetization reduction. This model is very appealing because of the simplicity of the basic idea behind it and because there is no need to enhance usually slow angular momentum dissipation mechanisms. For this reason, since the publication of superdiffusive theory, experimental work has supported or confuted the role of superdiffusive spin transport in ultrafast demagnetization dynamics [9] [10] [11] [12] [13]. It is an open debate which of these two models (M3TM and superdiffusion) plays the main role in demagnetization processes and whether specifically tailored sample geometries may favour one of them. Theoretical and experimental efforts are needed to give a unique understanding of the ultrafast dynamics in ferromagnetic metals. This is also the goal of this thesis through the experimental investigation of specifically designed samples.

Measurement and analysis of demagnetization curves

A powerful method to study non-equilibrium ultrafast magnetization dynamics is to perform pump and probe measurements on magnetic material via the time resolved (TR) magneto-optical Kerr effect (MOKE). MOKE describes the change of the polarization state of linearly polarized light reflected off a magnetized sample. The induced polarization state is directly proportional to the magnetization of the sample and is used to measure hysteresis loop and implemented in a pump and probe configuration aimed at exploring magnetization dynamics.
In this thesis, the TR-MOKE set up available at the Technische Universitaet Berlin has been improved in order to meet the measurement requirements, as reported in Chapter 2. The set up allows us to acquire demagnetization curves which describe the evolution of magnetization on a femtosecond timescale. The most important information they give is the demagnetization time constant τ_M, describing the reduction rate of magnetization, and the remagnetization time constant τ_E, which describes the recovery towards an equilibrium. These two parameters are very important. They characterize the demagnetization process and are used to compare different samples and geometries. Here, they will be measured in specifically designed samples to infer information on the mechanism underlying the demagnetization. In spite of the important role played by τ_E and τ_M, there is not a unique and recognized model in the literature to fit demagnetization curves. This is mostly due to the fact that this process is not fully explained and no simple analytical model presently exists. For this reason, before starting the data analysis on the samples it was necessary to take into account the different models and to compare the results they give when the same set of data is analysed. This is the topic of Chapter 3.

Motivation of the samples

Once the model has been chosen the samples are investigated and their demagnetization curves are analysed. In one set of samples, discussed in Chapter 4, gold gratings are nanostructured onto the surface of a magnetic Co/Pt multilayer (ML). When light impinges on the structured surface, the gold grating absorbs and reflects almost all the incident light and the underlying magnetic layer is not excited. Hence, the excitation is not uniform but it is modulated by the presence of the gold stripes. A lateral gradient is produced on a length scale relevant for spin superdiffusion. Note, that lateral diffusion

usually does not play any role since the dimension of the excited area is larger than the probed area, and is also much larger compared to the relevant length scale of the problem. The geometry of this samples allows also an enhancement and localization of the field, whose effect in demagnetization process are discussed.
In Chapter 5, demagnetization curves are analysed taken on samples based on the same Co/PT ML, grown on different substrates. The substrate has separate and different roles in superdiffusive spin transport and in M3TM, especially comparing insulating and conducting substrates. Spin polarised current cannot flow in an insulating substrate: in such samples demagnetization due to superdiffusive spin transport is inhibited. In the framework of the M3TM, coupled equations which describe the evolution of the system are developed and optimized for bulk Co. These coupled differential equations are numerically solved for the configuration analysed in the experiment. The aim is to compare the experimental results with the prediction of the M3TM and to explore the role of superdiffusive spin transport.

Chapter 1

Theoretical background

1.1 Ultrafast manipulation of magnetic ordering

Ultrafast dynamics in ferromagnetic metals is a subject intensely studied, because of its great potential in technology application and the ongoing efforts to understand the fundamental processes taking place during the non-equilibrium state of electrons, phonons and spins.

In a paper of 1996, Beaurepaire et al [1] showed that when a magnetic material is excited with a laser pulse of 60 femtoseconds (fs), a reduction in magnetization is observed within the first picosecond (ps). The following recovery takes a few picoseconds and is dominated by the dissipation of energy to the surrounding bath. In figure 1.1 the demagnetization curve detected with a magneto-optic set up is shown.

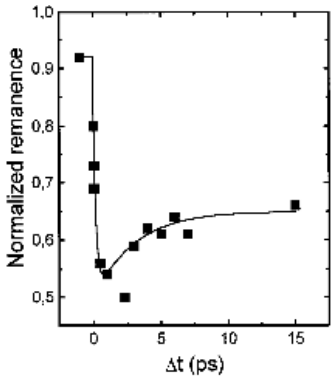

Figure 1.1: Longitudinal MOKE signal of a Ni(20 nm)/MgF_2(100 nm) film for 7 mJ cm^{-2} pump fluence. The signal is normalized to the unpumped signal and the line is a guide to the eye. This figure is taken from [1]

This discovery attracted the attention of the scientific community because for the first time magnetic order was manipulated in a sub-ps range. It is now established that in 3d transition magnetic metals, as cobalt and nickel, an optical excitation provides a demagnetization with typical time constants of 100-300 fs.
However, a complete theoretical understanding of the processes involved in this effect has not been achieved.
Beaurepaire et al. introduced a Three Temperature Model (3TM). It considers the material composed of three subsystems, electrons, spins and lattice, and analyses the energy transfer among the source term and the three subsystems.
This model does not give any microscopical explanation of the process and does not consider the conservation of angular momentum.
To fulfil this necessity, Koopmans et al. [4] developed the so-called Microscopic Three Temperature Model (M3TM), which treats the lattice as the angular momentum dissipation channel. The microscopic mechanism involves electron-phonon and electron-impurity scattering events, each of them with a finite probability for the electron to flip its spin.
For a decade, M3TM was the most widely accepted theory, but in 2010 Battiato et al. [8] proposed a new model which does not consider the lattice as the storage medium for angular momentum. Superdiffusive spin transport induced by spin-dependent velocity and lifetimes is used to explain the process leading to an ultrafast demagnetization.
These two models will be discussed in details in the following.

1.2 Three Temperature model (3TM)

To start with, the macroscopic explanation given by Beaurepaire et al., since the first observation of ultrafast demagnetization [1], will be summarized. This model is useful to fit experimental demagnetization curves as pointed out in references [14] and [15].

In this model the material is divided in three subsystems, electrons, spins and lattice, each of them is assumed to be in internal equilibrium, with its own temperature (T_e, T_s, T_l) and heat capacity (C_e, C_s, C_l).
In particular it is possible to define a temperature for the spin system thanks to the relation between the equilibrium magnetization and temperature, which is shown in figure 1.2 and is valid below the Curie temperature T_C.

The evolution of the system is described by three differential equations, which introduce the coupling constants between the 3 subsystems, G_{el}, G_{es}, G_{sl}. This coupling provides the thermalization of the system, through exchange of energy between the

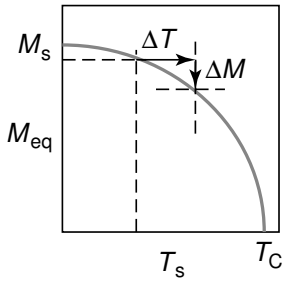

Figure 1.2: Equilibrium magnetization M_{eq} as a function of spin temperature T_s for a magnetic material below the Curie temperature T_C. In the figure it is shown how a change in temperature ΔT can be related to a change of magnetization amplitude ΔM. Figure taken from [14]

three subsystems.

$$C_e \frac{dT_e}{dt} = -G_{el}(T_e - T_l) - G_{es}(T_e - T_s) + P(t) \tag{1.1}$$

$$C_l \frac{dT_l}{dt} = -G_{el}(T_l - T_e) - G_{sl}(T_l - T_s) \tag{1.2}$$

$$C_s \frac{dT_s}{dt} = -G_{es}(T_s - T_e) - G_{sl}(T_s - T_l) \tag{1.3}$$

$P(t)$ represents the source term, referred to the energy absorbed by the electronic system. In Beaurepaire et al.'s paper [1], the free parameters are varied to reproduce the experimental curves in figure 1.3(a). $P(t)$ influences the maximum rise of electronic temperature. The spin temperature follows the electronic temperature, through G_{es}, and the lattice temperature, through G_{sl}. Its rise is due to the initial increase of T_e, for this reason the parameter which induces the fast increase is G_{es}.

Even if this model is still widely used in literature (it will be used in this thesis, in particular in Chapter 3), some limitations are undeniable.

It is not clear when one can define an electronic temperature, since electrons are in a highly non equilibrium state after the excitation. The same is true for the phonon and the spin systems, both of them may not be in internal equilibrium.

Regarding the spins, in [16] it is shown that after the excitation the Curie temperature can be reached by the spin system. Since the sample is not fully demagnetized, this means that this subsystem is not in internal equilibrium. To make things worse, the one-to-one relation between equilibrium magnetization and temperature, necessary to define T_s, is valid only below T_C.

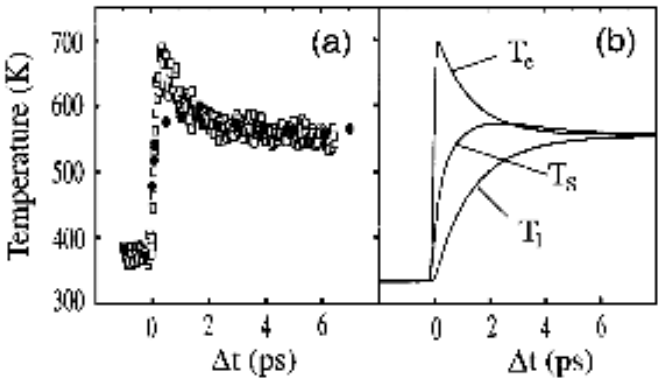

Figure 1.3: Results from [1]. In (a): squares refers to experimental T_e, deduced from transmittance measurement; circles refers to experimental T_s obtained through magnetization signal. In(b) simulated T_e, T_s and T_l.

1.3 A look through the possible channels for angular momentum dissipation

In this section the problem of conservation of angular momentum will be discussed.
As explained in the previous section, the magnetic metallic material can be divided into three reservoirs which can store energy. The electron, spin and lattice reservoirs can also store angular momentum. Its conservation and transfer must be taken into account. If a reduction of magnetization is observed within the first ps after an optical excitation, the angular momentum lost by the spin reservoir must flow into another subsystem.
This problem has been examined by Dalla Longa in [15].
The total angular momentum is composed by

$$\mathbf{J} = \mathbf{L}_e + \mathbf{S}_e + \mathbf{L}_{phonon} + \mathbf{L}_{photon}. \tag{1.4}$$

where $\mathbf{L}_e$ and $\mathbf{S}_e$ represent the orbital and the spin moment of electron; then the angular momentum carried by the phonon system $\mathbf{L}_{phonon}$ and by the laser field $\mathbf{L}_{photon}$ are considered.
The possible transfer between the spin and angular part of the electronic system is now considered. The magnetization is given by the spatial average of the atomic magnetic moment: $\boldsymbol{\mu} = \mu_B(\mathbf{L}_e + g\mathbf{S}_e)$ where $g \approx 2$ and $\boldsymbol{\mu} \approx g\mu_B\mathbf{S}_e$ (with μ_B the Bohr magneton) because of the quenching of orbital angular momentum in 3d transition metals. For this

property a transfer from $\mathbf{S}_e$ to $\mathbf{L}_e$ would lead to a maximum reduction of magnetization of 50 %, while a greater reduction has been observed. Apart from this semi-qualitative understanding, X-ray magnetic circular dichroism (XMCD) permits to separate the dynamics of the orbital and spin parts of electronic angular momentum. Using this approach transfer from spin to orbital electronic angular momentum has been excluded [17] [18].
In [19] Dalla Longa also demonstrates that the photon angular momentum has no role in the ultrafast demagnetization. Circularly polarized (CP) photons are used, each of them carrying a quantum of angular momentum along or opposite to the propagation direction. If the helicity and magnetization are parallel, a transfer of momentum from the photons to the spins would lead to an increase of demagnetization; if they are antiparallel then a decrease would be observed. In [19] the same sample is demagnetized using both right (RCP) and left (LCP) circularly polarized photons. No difference is seen in the time resolved MOKE response due to the pump helicity. Therefore, photon angular momentum does not contribute to ultrafast demagnetization.
The only reservoir which may sustain angular momentum transfer is thus the lattice. The fact that magnetization and the associated spins carry an angular momentum has been known since 1915, demonstrated by the experiment conducted by Einstein and de Haas [20]. A ferromagnetic rod inside a coil, where electric current can flow, is used to show the macroscopic transfer of angular momentum between spin and lattice. Changing the magnetization through the electric current leads to a rotation of the rod, preserving angular momentum.
What is the microscopic process which drives this effect in the femtoseconds world? The next section is dedicated to answer this question.

1.4 Ultrafast demagnetization through Elliot-Yafet spin flip scattering - Microscopic 3TM

The previous considerations lead Koopmans et al. to develop a microscopic model [4], where the angular momentum flows out of the electronic system into the lattice.
As we learned from the 3TM, electrons store the pump energy and thermalize through interaction with the colder lattice. The microscopic mechanism of demagnetization is identified in the Elliot-Yafet type of scattering [21] [22], where a finite spin-flip probability a_{sf} is associated to each electron phonon scattering event. The spin orbit coupling (SOC) is responsible for the possibility to have a spin flip during a scattering

event and for a non zero a_{sf}. Because of SOC, spin is not a good quantum number for a single electron eigenstate. Each Bloch eigenstate is a mixture of the two possible spin states $|\uparrow\rangle$ and $|\downarrow\rangle$:

$$|\psi^{\uparrow}_{\mathbf{k}n}\rangle = a^{\uparrow}_{\mathbf{k}n}|\uparrow\rangle + b^{\uparrow}_{\mathbf{k}n}|\downarrow\rangle \tag{1.5}$$

$$|\psi^{\downarrow}_{\mathbf{k}n}\rangle = a^{\downarrow}_{\mathbf{k}n}|\downarrow\rangle + b^{\downarrow}_{\mathbf{k}n}|\uparrow\rangle \tag{1.6}$$

where n is a band index, $b^{\uparrow\downarrow}_{\mathbf{k}n}$ are non zero only with the SOC, and the $b^{\uparrow\downarrow}_{\mathbf{k}n}$ components are generally smaller than the $a^{\uparrow\downarrow}_{\mathbf{k}n}$ components. They represent indeed the degree of spin mixing induced by the SOC. In his derivation Elliott [21] calculates $a_{sf} \propto \langle b^2 \rangle$, the latter being the spin mixing parameter, obtained averaging all the eigenstate spin mixing at the Fermi surface.
In the following, the microscopic model developed by Koopmans' et al. will be explained, as can be found in the supplementary information of [6]. The starting point is the Hamiltonian, which considers the three subsystems and their interaction.

$$\mathcal{H} = \mathcal{H}_e + \mathcal{H}_s + \mathcal{H}_l + \mathcal{H}_{ee} + \mathcal{H}_{el} + \mathcal{H}_{es} \tag{1.7}$$

Each of the Hamiltonian term is now identified. The electron system is modelled as a spinless Fermi sea with a constant density of states D_F; it can be described by Bloch functions $|\psi_{\mathbf{k}}\rangle = \frac{1}{\sqrt{N}} \sum_j e^{i\mathbf{k}\mathbf{r}_j}|u_j\rangle$, where N is the number of lattice site, j is the lattice site index and $\mathbf{k}$ the wave vector. The electronic Hamiltonian is thus:

$$\mathcal{H}_e = \sum_{\mathbf{k}} E(\mathbf{k}) c^{\dagger}_{\mathbf{k}} c_{\mathbf{k}} \tag{1.8}$$

where $c^{\dagger}_{\mathbf{k}}$ and $c_{\mathbf{k}}$ are the creation and annihilation operator for electrons in state $\mathbf{k}$, respectively. A lattice of N sites is described as an ensemble of identical oscillators, following the Bose-Einstein statistics, with a constant density of states D_p per atomic site and dispersion relation $\omega(\mathbf{q})$

$$\mathcal{H}_l = \sum_{\mathbf{q}}^{ND_p} \hbar\omega(\mathbf{q}) \left(\frac{1}{2} + a^{\dagger}_{\mathbf{q}} a_{\mathbf{q}} \right) \tag{1.9}$$

with $a^{\dagger}_{\mathbf{q}}$ and $a_{\mathbf{q}}$ being the creation and annihilation operator for phonons in state $\mathbf{q}$, respectively. The spin bath is described as formed by two level systems with a density of state D_s per atomic site (total number $N_s = ND_s$) and obeying the Boltzmann

statistics.

$$\mathcal{H}_s = \Delta_{ex} \sum_{j=1}^{N_S} S_{z.j} \tag{1.10}$$

where, for each two level system, $S_z = \pm\frac{1}{2}$ refers to spin up and spin down respectively. Δ_{ex} is the energy separation between spin up and spin down states and depends in a self consistent way on the average spin moment $\overline{S}$. Indeed, according to the mean field Weiss model [23], $\Delta_{ex} = g\mu_B H_{eff}$ where H_{eff} is the effective field, sum of the applied field and the Weiss molecular field, proportional to the magnetization.
At this point, interactions must be considered, starting with the interaction between electrons.

$$\mathcal{H}_{ee} = \frac{U}{N^2} \sum_{\mathbf{k}} \sum_{\mathbf{k'}} \sum_{\mathbf{k''}} \sum_{\mathbf{k'''}} c^\dagger_{\mathbf{k'''}} c^\dagger_{\mathbf{k''}} c_{\mathbf{k'}} c_{\mathbf{k}} \tag{1.11}$$

Where it is summed over all the initial $\mathbf{k}$, $\mathbf{k'}$ and final $\mathbf{k''}$, $\mathbf{k'''}$ states. U is the screened coulomb potential and it is taken to be so efficient that the electron system is always in internal equilibrium. The electronic occupation is thus described by a Fermi-Dirac distribution for all times.
An usual electron phonon interaction is considered, through a coupling constant λ_{ep}.

$$\mathcal{H}_{el} = \frac{\lambda_{ep}}{N} \sum_{\mathbf{k}} \sum_{\mathbf{k'}} \sum_{\mathbf{q}}^{nD_p} c^\dagger_{\mathbf{k}} c_{\mathbf{k'}} (a^\dagger_{\mathbf{q}} + a_{\mathbf{q}}) \tag{1.12}$$

The following is the one which describes the spin flip in a electron phonon scattering, responsible for the demagnetization.

$$\mathcal{H}_{es} = \sqrt{\frac{a_{sf}}{D_S}} \frac{\lambda_{ep}}{N^{\frac{3}{2}}} \sum_{\mathbf{k}} \sum_{\mathbf{k'}} \sum_{\mathbf{q}}^{ND_p} \sum_{j}^{N_S} c^\dagger_{\mathbf{k}} c_{\mathbf{k'}} (s_{j,+} + s_{j,-})(a^\dagger_{\mathbf{q}} + a_{\mathbf{q}}) \tag{1.13}$$

here a_{sf} is the Elliot-Yafet scattering probability; $s_{j,+}$ and $s_{j,-}$ are spin raising and lowering term at site j.
The excitation is expressed as an initial electronic temperature $T_e(0) = T_0 + \Delta T_e(0)$. The interaction Hamiltonian terms enter in the Fermi's golden rule and the rate equations are solved. After calculation (not shown here) the following rate equation for the magnetization of the system $m(t)$ is found:

$$\frac{dm(t)}{dt} = Rm(t)\frac{T_l}{T_C}\left(1 - m(t)coth\left(\frac{mT_c}{T_e}\right)\right) \tag{1.14}$$

where m with no temporal dependence is the equilibrium magnetization relative to the equilibrium magnetization at T=0: $m = \frac{M_{eq}(T)}{M_{eq}(0)}$, where T is the ambient temperature. The constant R is

$$R = \frac{8 a_{sf} G_{el} k_B T_C^2 V_{at}}{(\mu_{at}/\mu_B) E_D} \tag{1.15}$$

where E_D is the Debye energy, V_{at} the atomic moment and μ_{at} the atomic magnetic moment.

The magnetization change depends on electron and lattice temperature, which can be obtained through the Two Temperature Model, which is analogue to the 3TM, but considers only the electron and lattice subsystems.

Since the first attempt [4] it has been established that with high enough a_{sf} parameter, the peak in the spin temperature is faster then energy relaxation, as shown in figure 1.4.

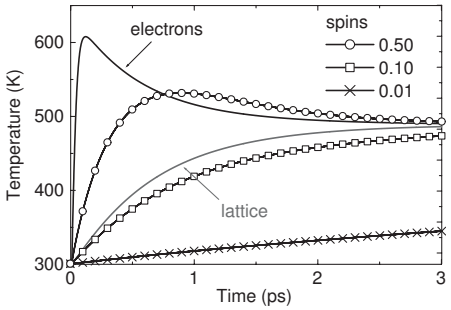

Figure 1.4: Simulated electrons, spins, lattice temperature in Ni at 100 fs after laser excitation [4]. Spin temperature is reported for different a_{sf}, as shown in the legend, while T_e an T_l only for $a = 0.50$.

With the analytical solution for $m(t)$ in 1.14 it is possible to get a_{sf} as a fitting parameter from experimental data. Results are reported in [6]: for Ni it is found $a_{sf} = 0.19 \pm 0.03$ and for Co $a_{sf} = 0.150 \pm 0.015$. It can be argued that these values are too high to be reasonable, since they mean that more than 10% of the electron-phonon scattering events leads to an electron spin flip. Experimental spin flip probability is available for several metals [22] but not for ferromagnetic transition metals. It was found to scale with Z^4 [5]. A material with very similar Z as Co and Ni is Cu, which has $a_{sf} = 0.001$. However, it has been demonstrated that band crossing at the Fermi level can enhance this parameter by two orders of magnitude [24].

Ab initio calculation for a_{sf} in Co and Ni has been performed in [6] by Koopmans et al. and confirm their fitting parameter value.

This model has successfully explained several experimental results [6] [25]. In addition it can explain the different demagnetization dynamics in Gd, whose demagnetization is several order of magnitudes slower, τ_M=80-100 ps [26] [27]. Indeed, equation 3.22 through the parameter $R \propto a_{sf}\frac{T_C^2}{\mu_{at}}$ predicts two types of dynamics according to the magnitude of R. Large R correspond to a more efficient and faster demagnetization, small R to a slower one. This depends on the material through the ratio $\frac{T_C^2}{\mu_{at}}$. Value found in [6] are $R(\mathrm{Co}) = 25.3\mathrm{ps}^{-1}$, $R(\mathrm{Ni}) = 17.3\mathrm{ps}^{-1}$, $R(\mathrm{Gd}) = 0.092\mathrm{ps}^{-1}$.
To close this section, it must be noted that this model has its own limitations: it considers the three subsystems to be in internal equilibrium, which is not necessarily true. In particular, as regard the electrons, the source term excites just a part of the electron system, but the internal thermalization time is here neglected, taking a Fermi-Dirac distribution as electronic occupation for all times. However, electrons thermalization can take almost the same amount of time necessary for demagnetization, as it has been shown soon after the first observation of ultrafast demagnetization by Hohlfeld et al. [28]; electron thermalization time for Ni is found to be about 100 fs in [14]. In spite of this, the approximation of an instantaneous thermalization has a fundamental role in all the derivations, since the electronic system is described by a Fermi Dirac distribution. It is also doubtful whether Fermi golden rule is a reasonable approximation, since it relies on known phonon energies, which are only defined after a phonon period, i.e. a time that will in general exceed the ultrafast scattering processes.
In addition in [7], Carva et al. performed an *ab initio* calculation of the electron spin flip induced by electron phonon interaction in 3d transition ferromagnetic metals, without employing Elliott approximations and derivation. In particular they consider both a thermalized and a non equilibrium electron distribution. Results showed that a thermalized distribution cannot provide a demagnetization, since the spin flip probability is negligible. For a non equilibrium distribution, the increasing spin flip scattering events are not balanced with the decreasing ones and a demagnetization is possible. However, only a very small spin flip probability is found even in this case and it cannot sustain the experimental demagnetization process.

1.5 Superdiffusive spin transport and its role in ultrafast demagnetization

In the last three years a new model has been developed to describe the ultrafast dynamics in ferromagnetic materials and the fs-scale demagnetization. Within this new picture there is no need to enhance the usual channel for angular momentum dissipation; the main mechanism responsible for ultrafast demagnetization does not include transfer between the angular momentum reservoirs, nor an internal dissipation in the electronic system.
After a laser excitation, excited electrons thermalize through scattering with other electrons, the lattice and impurities. Meanwhile, they also diffuse inside the material. Battiato et al. [8] [29] has performed an analysis of the electron transport in the fs range. They have built a model for this superdiffusive transport, different from the usual transport models: brownian and ballistic.
This model not only helps in describing the diffusion in the fs time range for thin layers, but can also explain the observed sub-ps demagnetization, through the spin dependent electron life time.
In ferromagnetic materials, majority electrons have a higher mobility and a longer life time than minority ones. This causes a depletion of majority electrons in the excited (and then probed) area; thus the measured magnetization of the sample decreases.

To start with, it is shown why the two limits of transport, ballistic and standard diffusion (Brownian motion), are not used in this picture. The ballistic transport considers the mean electron lifetime to go to infinity, and no scattering events to happen during transport. On the contrary, standard diffusion assumes the particle mean free path to be negligible, $\lambda \to 0$. Excited electrons in sp-like bands have a velocity of 1 nm fs^{-1} [8]. The electron lifetimes are about few tens of fs [30] [31], within the temporal range of interest; the mean free path is of tens of nanometers, usually comparable with the material dimension. For this reason both transport models do not correctly represent dynamics in magnetic metallic layers after optical excitation. In figure 1.5 a visual representation of the two limits of transport is shown (black for brownian motion and blue for ballistic), as well as the dynamics in the general experimental condition (red) in ultrafast magnetism experiments.

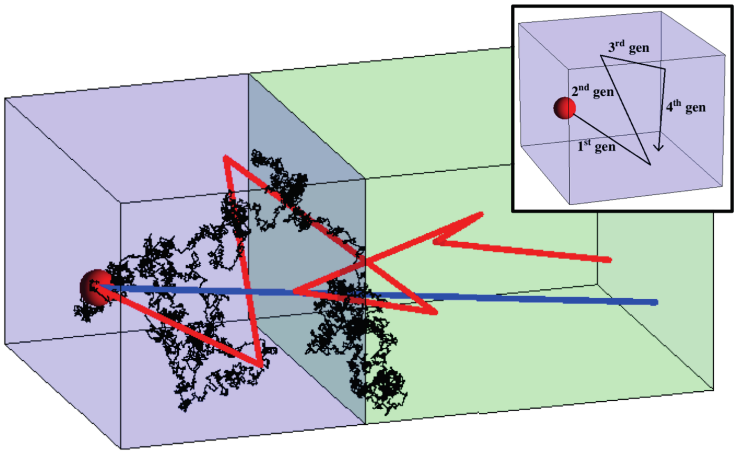

Figure 1.5: Different diffusion regime in a sample composed of two different materials. The black line represents the standard diffusion with $\lambda \to 0$, the blue line the ballistic transport $\lambda \to \infty$ (no scattering events). On the contrary, in the temporal range of interest in ultrafast magnetism and with the usual sample dimension, excited electrons experience a finite, non zero scattering events, as in the red line. In the inset it is pointed out that electron electron scattering leads to generation of electron cascade. Picture taken from [32].

1.5.1 Non equilibrium electrons transport

In this section the regime of transport for excited electrons as derived in [29] is discussed. Let's start by explaining qualitatively what happens after a laser excitation in a magnetic material.

Electrons excited by the laser pulse acquire a velocity, the emission is isotropic, since the photonic momentum is negligible. The electron trajectory is a straight line until the electron scatters with other electrons, phonons or impurities. Scattering with phonons and impurities will be approximately elastic and the outgoing direction is random. Scattering events with other electrons below or at the Fermi energy can be inelastic and subsequently excite another electron, pushing it above the Fermi energy, which itself starts travelling and scattering. This type of excited electrons are called the second generation electrons, which can excite third generation electrons and so on. The generation of an electron cascade is shown in the inset of figure 1.5. In electron-electron scattering, the outgoing direction depends on the ingoing direction, but in the calculation it is taken as isotropic. Battiato et al. [29] justifies this choice comparing in Ni the effective mass of the travelling *sp*-like electrons and of the larger effective mass of the electrons in the occupied d bands.

In the following the derivation of non equilibrium (NEQ) electron transport equation is summarized, a detailed derivation can be found in [29].
The model is developed for a sample with only transversal inhomogeneity, so all the quantities of interest depend on the z coordinate only. In particular the electron velocity and lifetime are energy and spin dependent, thus $v = v(z, \sigma, E)$ and $\tau = \tau(z, \sigma, E)$ and they can be derived with *ab initio* calculations [30] [31]. They are reported in figure 1.6 for Ni, as calculated in [30].

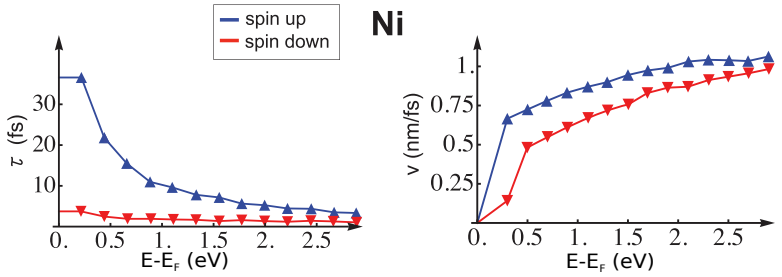

Figure 1.6: Electron lifetime and velocity in nickel obtained from *ab initio* calculations in [30]. These quantities are different for majority (blue) and minority (red) electrons, the former having better transport properties. Figure from [29].

In addition, in [33] and in [34] the majority and minority life time ($\tau^{\uparrow}$ and $\tau^{\downarrow}$ respectively) are measured in Co, the material used for the samples studied in this thesis. A ratio of $\frac{\tau^{\uparrow}}{\tau^{\downarrow}}$ =2 is found at 1 eV above the Fermi energy, decreasing at lower energy, in contradiction with results for Ni shown above. All of these values are known with some uncertainty.
The probability for an electron excited at the point s_0 to reach a point s without being scattered is thus

$$P(s) = exp\left[-\int_{s_0}^{s} \frac{\mathrm{d}s'}{\tau(s')v(s')}\right] \tag{1.16}$$

Focusing on just the first generation electron, an external source term S^{ext} may be defined, which depends on the laser intensity and absorption profile. This external source term gives the flux of first generation electrons $\Phi^{[1]}$, therefore an operator $\hat{\phi}$ can thus be defined $\hat{\phi}S^{ext} = \Phi^{[1]}$.
A continuity equation for the first generation electron density $n^{[1]}$ must now be considered

$$\frac{\partial n^{[1]}}{\partial t} = -\frac{\partial \hat{\phi} S^{ext}}{\partial z} - \frac{n^{[1]}}{\tau} + S^{ext} \tag{1.17}$$

where $\frac{n^{[1]}}{\tau}$ is the number of scattered first generation electrons, which, after scattering,

belong to the second generation electron.
It is thus possible to define a "source term" for the second generation electrons through the scattering term at all energies:

$$S^{[2]} = \sum_{\sigma'} \int p(\sigma, \sigma', E, E', z) \frac{n^{[1]}(\sigma', E', z, t)}{\tau(\sigma', E', z, t)} \mathrm{d}E' \tag{1.18}$$

$p(\sigma, \sigma', E, E', z)$ is the transition probability after a scattering, which takes into account that some of the electrons are stopped after scattering. As previously pointed out and used here, the outgoing and ingoing directions are taken not correlated. It is now useful to define an operator $\hat{S}$, which gives the "source term" for the second generation $\hat{S}n^{[1]} = S^{[2]}$. A continuity equation is written also for the second generation electrons and the scattered ones constitute a source term for the third generation electrons. This procedure can be iterated to obtain the transport equation for the full NEQ electrons density $n(\sigma, E, z, t) = \sum_{N=1,\infty} n^{[N]}(\sigma, E, z, t)$, performing the sum of the continuity equation for all the $n^{[N]}$.

$$\frac{\partial n}{\partial t} + \frac{n}{\tau} = \left(-\frac{\partial \hat{\phi}}{\partial z} + \hat{\phi} \right) (\hat{S}n + S^{ext}) \tag{1.19}$$

Hence, the generation operator applied to the ith electrons generation $n^{[i]}$ gives $\hat{S}n^{[i]} = S^{[i+1]}$, source term for $i+1$th generation. While the flux operator gives $\hat{\phi}S^{[i]} = \Phi^{[i+1]}$, the flux of $(i+1)$th generation electrons.
The last equation is thus the transport equation for NEQ electrons, obtained considering all the possible scattering events and above all it includes the thermalization of the electronic system, ignored in other descriptions of dynamics after laser excitation. This superdiffusive transport does not belong either to the standard diffusion regime or to the ballistic transport. Battiato et al shows in [29] that the class of transport to which 1.19 belongs depends on time. For times soon after the excitation it is ballistic, for longer times (1000 fs) Brownian. This can be expected since right after the excitation electrons have not experienced any scattering yet, for times longer than the lifetime this cannot be true any more.
Equation 1.19 is important for magnetization dynamics, because majority and minority electron density is different, and the magnetization value can be expressed through $M(E, z, t) = 2\mu_B[n(\uparrow, E, z, t) - n(\downarrow, E, z, t)]$.
Considering that the magnetic metal contains two types of carriers, majority and mi-

nority electrons, equation 1.19 successfully simulates the ultrafast demagnetization in ferromagnetic transition metals. Figure 1.7 shows result for 10 nm Ni grown on a conducting layer and on an insulator. The substrate has an influence on the magnetic response, because electrons can diffuse in the conductor and not in the insulator. The

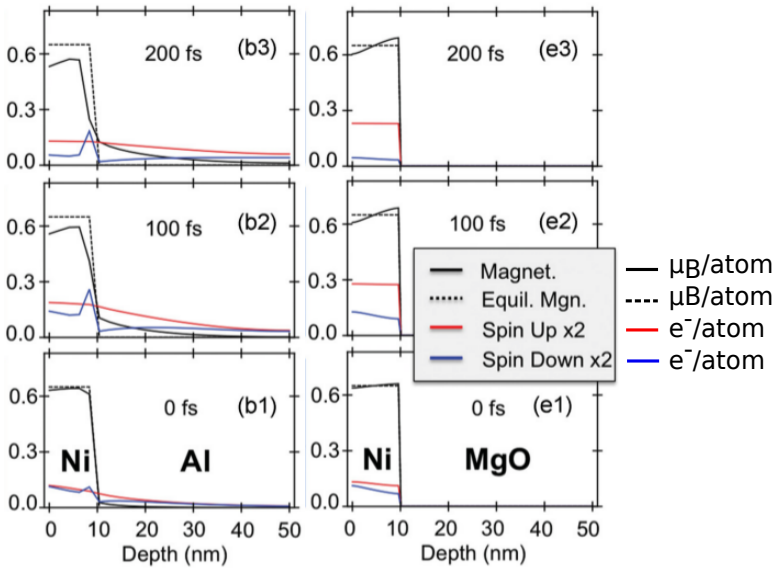

(a) density profile

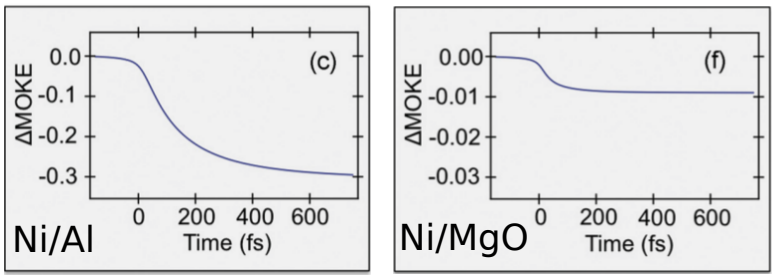

(b) demagnetization curve

Figure 1.7: a) Density profile for majority (red) and minority (blue) electrons. Black line refers to magnetization density, compared to the equilibrium magnetization (dash line). All these quantities are calculated for three different instant of time. b) Predicted time dependence of the normalized MOKE signal. Left panel refers to 10nm of Ni grown on Al, while the right to 10 nm of Ni grown on the insulating MgO. [29]

density profile in figure 1.7(a) shows that, for Ni on Al, spin majority electrons are distributed uniformly in both layers, while the minority ones are just in the magnetic layer. This leads to demagnetization in the Ni layer. The peak at the interface is due

to the minority electrons that are generated in Al and diffuse into the Ni layer, where their transport properties are far worse and they are blocked at the interface. An effect is seen even at around 0 fs due to the temporal width of the laser pulse (40 fs for the simulation). Fitting the demagnetization curve given by the normalized MOKE signal in figure 1.7(b), with a decreasing exponential, leads to a demagnetization time $\tau_M = 160fs$. As concerns the magnetic material grown on an insulator, spins cannot diffuse away from the former, so the density distribution is uniform. Hence, the net average magnetization is not changed. Its profile follows the laser density profile: in the surface the stronger excitation gives a demagnetization, while the magnetization increases in the depth because of the diffusion from the surface. Demagnetization is far weaker and $\tau_M = 60fs$. In this uniaxial model lateral diffusion is not considered and even in real case it does not have any role, because of the usually large excited area dimension ($\sim \mu m$) compared to the length scale interesting for diffusion (tens of nm).
It has been explained how superdiffusive motion and spin dependent velocity and lifetime can have a fundamental role in ultrafast demagnetization. The experimental ultrafast magnetism community is working to find evidence of this mechanism and some papers have already been published about that. [9] [10] [13] [35] [36]
Battiato et al.'s work on superdiffusion has an importance in magnetism dynamics that goes beyond the search for ultrafast demagnetization mechanism. The field of spintronics is having a fast development; in principle spin transport can be disconnected by charge transport preventing the Joule effect and its waste of energy and this possibility is appealing. In the picture here drawn of superdiffusive spin transport, the excitation is a very efficient process thanks to electron cascade: a single photon can excite several generations of electrons. There is in principle the possibility to exploit ultrafast spin transport, with high spin velocities of about 1 nm/fs, triggered by laser excitation in a very efficient way.

The two models here discussed explain the ultrafast demagnetization with two completely different mechanism.
Magnetization reduction through spin flip scattering has been assumed valid for over a decade and was successful in explaining experimental results.
However in the last two years, several groups have focused their attention of superdiffusive transport as a mechanism for ultrafast demagnetization and have given experimental evidence for it.
Recently, it has been shown that both mechanisms have an important role. In [11] a Ni and a Fe layer are separated by a non magnetic layer X, conducting or insulating

(Ni/X/Fe). The optical pump impinges on the Ni side and the magnetic signal is detected from both the Ni and the Fe. When X is conductor an increase in magnetization in the Fe layer is detected, due to the transport of majority electrons from Ni to Fe. When X is insulating, a demagnetization is still present in Fe layer, but now no spin current can flow into it. Knowing the atomic moment of both Ni ($0.65\mu_B$) and Fe ($2.2\mu_B$) a transfer of spin between the two should lead to a three times larger change in Fe. Experimental values do not confirm this prediction, because an additional demagnetization mechanism is taking place.
Both mechanisms are thus necessary to build a complete picture of the ultrafast dynamics in magnetic metals. Further theoretical and experimental efforts are necessary to quantify and describe in detail this coexistence.

Chapter 2

Experimental setup: time resolved magneto-optical Kerr effect

In this thesis the ultrafast dynamics of magnetic materials is investigated with a time resolved (TR) magneto-optical Kerr effect (MOKE) experimental set up. The MOKE effect refers to the change in the state of polarization when light impinges onto a magnetic material. It is used to measure the magnetization of the sample. It can be thus applied in pump and probe techniques to measure the effect of the pump excitation. When fs laser pulses are used, the sub-ps dynamics are accessible. In this chapter the MOKE effect is discussed in detail, then the experimental set up is described.

2.1 Magneto-optical Kerr effect (MOKE)

When light impinges on a magnetic material, the polarization state changes both in the transmitted beam (Faraday effect) and in the reflected one (MOKE). This change depends on the magnetization, a calibration enables measuring the magnetization through the change of polarization.
Since metals absorb light very efficiently, the transmitted signal is not high enough and it is preferred to measure the change in polarization of the reflected beam.
The effect of MOKE on linear polarized light is graphically depicted in figure 2.1: a rotation in the polarization plane θ_k and an acquired ellipticity ϵ_k appear. They form the complex Kerr rotation:

$$\vartheta_k = \theta_k + i\epsilon_k \tag{2.1}$$

These changes are due to the different response to the left circular polarized (LCP)

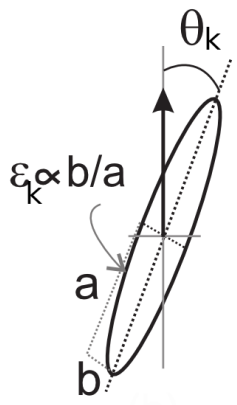

Figure 2.1: Schematic picture of the change in the state of polarization of linearly polarized light due to MOKE. θ_k refers to the rotation angle to the polarization plane; ϵ_k to the acquired ellipticity, defined as the ratio of the polarization axis length (a and b).

and right circular polarized (RCP) light. A linear polarized light field can be seen as a superposition of two circular polarized light fields, one RCP and the other LCP. The rotation of polarization plane θ_k is caused by different velocities of the two components. On the contrary the different absorption rate for the two leads to the ellipticity ϵ_k.
Macroscopically, this effect relies on the off-diagonal elements of the dielectric tensor, which are non zero if the propagation medium is magnetic. This gives different complex index of refraction for RCP and LCP. The real part determines the propagation velocity, the imaginary part the absorption.
From a quantum mechanical point of view the origin of the MOKE effect is the spin orbit coupling, which couples the electron spin with its motion, determining the optical properties. Both this pictures are discussed in this section.

2.1.1 Macroscopic picture: dielectric tensor

The wave equation that describes the propagation of an electromagnetic wave $\mathbf{E}(r,t)$ in a medium is the following [37]

$$\bigtriangledown \times \bigtriangledown \times \mathbf{E}(\mathbf{r},t) + \frac{1}{c^2}\frac{\partial^2 \mathbf{E}(\mathbf{r},\mathbf{t})}{\partial t^2} = -\frac{1}{\epsilon_0 c^2}\frac{\partial^2 \mathbf{P}(\mathbf{r},\mathbf{t})}{\partial t^2} \tag{2.2}$$

$\mathbf{P}(\mathbf{r},t)$ is the polarization vector and is defined taking the average of the dipole moment per atomic volume. It describes the response of the medium at the electromagnetic wave. Performing a Taylor expansion, it can be divided into the linear (the first order) and non linear term: $\mathbf{P}(\mathbf{r},t) = \mathbf{P}^L(\mathbf{r},t) + \mathbf{P}^{NL}(\mathbf{r},t)$. MOKE is a linear effect, therefore the non linear term will be neglected.
The response of the medium depends on the electrical susceptibility $\tilde{\chi}$:
$\mathbf{P}^L(\mathbf{r},t) = \epsilon_0\tilde{\chi}\mathbf{E}$, which is related to the dielectric tensor $\tilde{\epsilon}$: $\tilde{\chi} = (\tilde{\epsilon} - \tilde{1})$, where $\tilde{1}$ is the identity tensor. For an isotropic medium the dielectric tensor can be expressed as a constant, but the magnetization makes the medium anisotropic and the off diagonal elements of the dielectric tensor not zero.
Now, the different optical properties for RCP and LCP light will be derived. The wave equation 2.2 can be expressed through the dielectric tensor and using the property $\bigtriangledown \times \bigtriangledown \times \mathbf{E} = - \bigtriangledown^2 \mathbf{E} + \bigtriangledown(\bigtriangledown \cdot E)$

$$- \bigtriangledown^2\mathbf{E} + \bigtriangledown(\bigtriangledown \cdot E)(\mathbf{r},t) + \frac{\tilde{\epsilon}}{c^2}\frac{\partial^2\mathbf{E}(\mathbf{r},\mathbf{t})}{\partial t^2} = 0 \tag{2.3}$$

Inserting the solution for the electric field as $\mathbf{E} = \mathbf{E}_0 e^{(i\frac{\omega}{c}\mathbf{nr} - i\omega t)}$, where $\mathbf{n}$ is the index of refraction vector, and performing the calculation the Fresnel equation is obtained:

$$n^2\mathbf{E} - \mathbf{n}(\mathbf{nE}) = \tilde{\epsilon}\mathbf{E} \tag{2.4}$$

This linear system for the three component of the electric field has a non trivial solution if

$$det||n^2\delta_{ik} - n_i n_k - \epsilon_{ik}(\omega)|| = 0 \tag{2.5}$$

Solving the last equation leads to the eigenvalues of the problem, the index of refraction. Consequently, inserting them in eq. 2.4, the eigenvectors can be obtained, which are the different states of polarization.
Before that, it is necessary to define the dielectric tensor for a magnetic medium with a random magnetization orientation. [38]

$$\tilde{\epsilon} = \epsilon \begin{pmatrix} 1 & -iQm_z & iQm_y \\ iQm_z & 1 & -iQm_x \\ -iQm_y & iQm_x & 1 \end{pmatrix} \tag{2.6}$$

where m_x, m_y, m_z are the direction cosines of the magnetization $\mathbf{M}$, i.e. the cosine of the angle between the magnetization and the three axes. Q is the magneto-optical constant, which is proportional to the magnetization. $\epsilon_{xx} = \epsilon_{yy} = \epsilon_{zz} = \epsilon$ is taken for simplicity of calculus. With this dielectric tensor the two eigenvalues for Eq. 2.5 are $n_{R,L} = n(1 \pm \frac{Q}{2}\hat{\mathbf{m}}\hat{\mathbf{k}})$, which represents the refraction index for the two eigenvectors: the right and left circular polarization.
When a linear polarized light field travels with a propagation vector $\mathbf{k}$ a distance L in a magnetic medium with a random magnetization orientation (defined with the cosine direction $\hat{\mathbf{m}}$) the complex Kerr rotation is given by the complex difference of phase of the LCP and RCP components:

$$\vartheta_K = \frac{\pi L}{\lambda}(n_L - n_R) = -\frac{\pi L n}{\lambda} Q \hat{\mathbf{m}}\hat{\mathbf{k}} \tag{2.7}$$

Both the Kerr rotation and ellipticity are proportional to the magnetization.
In the following, the complex Kerr rotation will be expressed through the reflection coefficients, which is the most useful to be applied to an experiment.
The reflection matrix for a polarized field reflected by a sample is defined as follows:

$$\hat{\mathcal{R}} = \begin{pmatrix} r_{pp} & r_{ps} \\ r_{sp} & r_{ss} \end{pmatrix} \tag{2.8}$$

r_{ij} being the ratio of reflected i polarized light and incident j polarized light. S and P polarization are defined commonly as perpendicular and parallel with respect to the plane of incidence, respectively. The complex Kerr rotation for P polarized light ϑ_k^p and S polarized light ϑ_k^s is expressed as:

$$\vartheta_k^p = \frac{r_{sp}}{r_{pp}} \tag{2.9}$$

$$\vartheta_k^s = \frac{r_{ps}}{r_{ss}} \tag{2.10}$$

Such r_{ij} coefficients must thus be calculated in order to associate the Kerr rotation to known quantities, such as the index of refraction, the incident angle and the magneto-optical constant. Nowadays, the majority of the samples used in magneto-optics are optical thin multilayers (ML) formed by magnetic and non magnetic materials. All samples analysed in this thesis are indeed ML. It is thus necessary to derive expressions for Eqs. 2.9 and 2.10 valid in this configuration. This was done by Zak et al.

in [39], and it will be reported in the following.

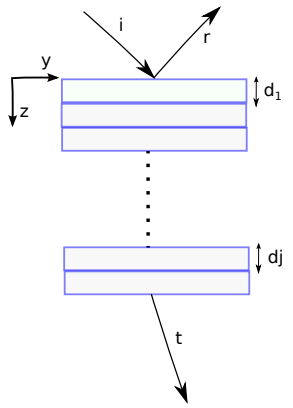

Figure 2.2: Sketch of light impinging onto a ML, where the jth layer has thickness d_j. The incident i, reflected r and transmitted t beams are shown.

Given a ML as in figure 2.2, two vectors are defined:

$$F = \begin{bmatrix} E_x \\ E_y \\ H_x \\ H_y \end{bmatrix} \qquad P = \begin{bmatrix} E_s^i \\ E_p^i \\ E_s^r \\ E_p^r \end{bmatrix}$$

The P vector for the incident medium P_i and the final medium P_t are:

$$P_i = \begin{bmatrix} E_s^i \\ E_p^i \\ r_{ss}E_s^i + r_{sp}E_p^i \\ r_{ps}E_s^i + r_{pp}E_p^1 \end{bmatrix} \qquad P_t = \begin{bmatrix} t_{ss}E_s^i + t_{sp}E_p^i \\ t_{ps}E_s^i + t_{pp}E_p^i \\ 0 \\ 0 \end{bmatrix}$$

where t_{ij} the ratio of transmitted i polarized light and incident j polarized light.
The main ingredients of Zak et al.'s derivation are the medium boundary A matrix and propagation D matrix.
The A matrix is defined through the relation $F_j = A_j P_j$ for the jth layer. It takes care of the boundary condition at each interface. Then the propagation in the layer must be taken into account. Hence, the D matrix relates the S and P components at the two surfaces of a layer. The P vector has a z dependence and for instance for the first layer one gets $P_1(0) = D_1 P_1(d_1)$. Considering reflection and propagation for all layers, the

following equation is obtained:

$$\begin{aligned} F_i &= A_i P_i \\ &= A_1 D_1 P_1 \\ &= A_1 D_1 A_1^{-1} A_1 P_1 \\ &= A_1 D_1 A_1^{-1} A_2 D_2 P_2 \\ &= ... = \prod_{m=1}^{N} (A_m D_m A_m^{-1}) A_t P_t \end{aligned} \tag{2.11}$$

The P vector in the incident medium can be related to the P vector in the final medium as in the following equation:

$$P_i = M P_t = A_i^{-1} \prod_{m=1}^{N} (A_m D_m A_m^{-1}) A_t P_t = \begin{pmatrix} G & H \\ I & J \end{pmatrix} P_t \tag{2.12}$$

The I and G values are of interest since it can be demonstrated [40] that

$$G^{-1} = \begin{pmatrix} t_{ss} & t_{sp} \\ t_{ps} & t_{pp} \end{pmatrix} \qquad IG^{-1} = \begin{pmatrix} r_{ss} & r_{sp} \\ r_{ps} & r_{pp} \end{pmatrix} \tag{2.13}$$

The completed calculus for A and D matrices can be found in [39]. They are then used to obtain I and G matrix, from those, thanks to 2.13, the complex Kerr rotation is inferred.

The results for the limit of ultrathin film, which means that the total optical length is small compared to the wavelength $\sum_i n_i d_i \ll \lambda$ [41] are now considered. All samples found in this thesis satisfy this property. The following results are referred to a ML where the initial and final media (having n_i and n_f refractive index, respectively) are not magnetic, the incident angle for the radiation λ is θ_i and the refraction angle in the final medium is θ_f. The mth layer has a thickness d_m and its magnetization direction

is arbitrary and described with the direction cosines m_x^m, m_y^m, m_z^m:

$$r_{pp} = \frac{n_f cos\theta_i - n_i cos\theta_f}{n_f cos\theta_i - n_i cos\theta_f} \tag{2.14}$$

$$r_{sp} = -\frac{4\pi}{\lambda} \frac{n_i cos\theta_i}{(n_i cos\theta_i + n_f cos\theta_f)(n_f cos\theta_i + n_i cos\theta_f} \times \left(cos\theta_f \sum_m d_m n_m^2 Q m_z^m + n_f n_i sin\theta_i \sum_m d_m Q m_y^m \right) \tag{2.15}$$

$$r_{ss} = \frac{n_1 cos\theta_i - n_f cos\theta_f}{n_i cos\theta_1 + n_f cos\theta_f} \tag{2.16}$$

$$r_{ps} = -\frac{4\pi}{\lambda} \frac{n_i cos\theta_i}{(n_i cos\theta_i + n_f cos\theta_f)(n_f cos\theta_i + n_i cos\theta_f} \times \left(cos\theta_f \sum_m d_m n_m^2 Q m_z^m - n_f n_i sin\theta_i \sum_m d_m Q m_y^m \right) \tag{2.17}$$

This is quite a valuable result thanks to the additivity in r_{sp} and r_{ps}: the Kerr signal given by a ML is the sum of the signals given by each magnetic layer, the non magnetic ones do not affect the signal.

In [38] the so obtained reflection coefficients are inserted in 2.9 and 2.10, and compared with experimental data on Co/Pd multilayer, showing accordance, as reported in figure 2.3. In the figure the polar configuration refers to the geometry for the Kerr angle acquisition: magnetization perpendicular to the sample surface and parallel to the plane of incidence. The possible geometries are described in section 2.2.

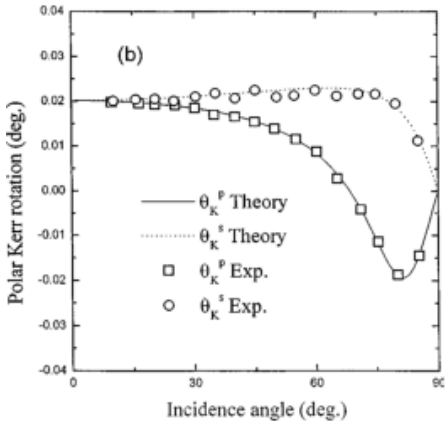

Figure 2.3: Comparison between experimental and theoretical Kerr rotation in a Co/Pt multilayer for polar configuration. After [38].

2.1.2 Quantum picture of MOKE

The difference in the response to RCP and LCP light is in this section discussed quantum mechanically. The detailed derivation found in [42] helps understanding why this effect is visible only in ferromagnetic metals, it depends indeed on the exchange splitting.
So far, the dielectric tensor has been considered. It is necessary now to recall the relation between the dielectric tensor $\tilde{\epsilon}$ and the conductivity tensor $\tilde{\sigma}$:

$$\tilde{\epsilon} = 1 + i\frac{4\pi}{\omega}\tilde{\sigma} \tag{2.18}$$

As well as for $\tilde{\epsilon}$, the off-diagonal elements of $\tilde{\sigma}$ cause the complex Kerr rotation. The imaginary part of the conductivity tensor describes the absorption of the medium. To calculate it the Fermi golden rule is used, to obtain [43]:

$$\sigma''_{xy}(\omega) = \frac{\pi e^2}{4\hbar\omega m^2\Omega}\sum_{i,f} f(E_i)[1 - f(E_f)][|\langle i|p_-|f\rangle|^2 - |\langle i|p_+|f\rangle|^2]\delta(\omega_{fi} - \omega) \tag{2.19}$$

here Ω is the volume, e and m the electron charge and mass. $f(E)$ is the Fermi-Dirac distribution at energy E, $p_\pm = p_x \pm ip_y$ and $\omega_{fi} = \frac{E_f - E_i}{\hbar}$ is the frequency correspondent to the energy separation between the two levels i and f. Each term of the sum represents an optical transition between an occupied state $|i\rangle$, with energy E_i, and an unoccupied state $|f\rangle$, with energy E_f. $\langle i|p_\mp|f\rangle$ is the dipolar transition matrix element for RCP and LCP light, respectively. Hence, $\sigma''_{xy}(\omega)$ is proportional to the difference of absorption probability for RCP and LCP light. Regarding to $\sigma'_{xy}(\omega)$, it can be calculated from $\sigma''_{xy}(\omega)$ using the Kramers-Kroenig relations.
It should be reminded that optical transitions are vertical in the reciprocal space, due to the small photon wave vector compared to the electronic state wave vector. $|i\rangle$ and $|f\rangle$ have thus the same $\mathbf{k}$. In addition, optical transition must obey selection rules:

$$\Delta l = \pm 1 \tag{2.20}$$

$$\Delta m_l = \pm 1 \tag{2.21}$$

The selection rule over l allows transition only between states with different parity. A transition with $\Delta m_l = +1$ is due to LCP light and $\Delta m_l = -1$ to RCP light.
In reference [42] a transition between $d_{xz,yz}$ level ($l = 2$, $m_l = \pm 1$) and p_z level ($l = 1$, $m_l = 0$) is considered to explain how the exchange interaction and spin orbit coupling

lead to a different absorption between RCP and LCP light. Transition between d and p state is allowed for parity. The majority and minority spin d levels in ferromagnetic metals are split by the exchange interaction of an energy Δ_{ex} [42]. The spin orbit coupling (SOC) splits the levels according to m_l: $d_{(x+iy)z}$ ($m_l = +1$) and $d_{(x-iy)z}$ ($m_l = -1$); the energy separation is Δ_{SO}. The $m_l = +1$ level has higher energy than $m_l = -1$, for majority spins, while $m_l = -1$ is the highest energy level for minority spins. In figure 2.4 levels are sketched and the absorption processes are shown, elucidating the difference in absorption processes of RCP and LCP light.

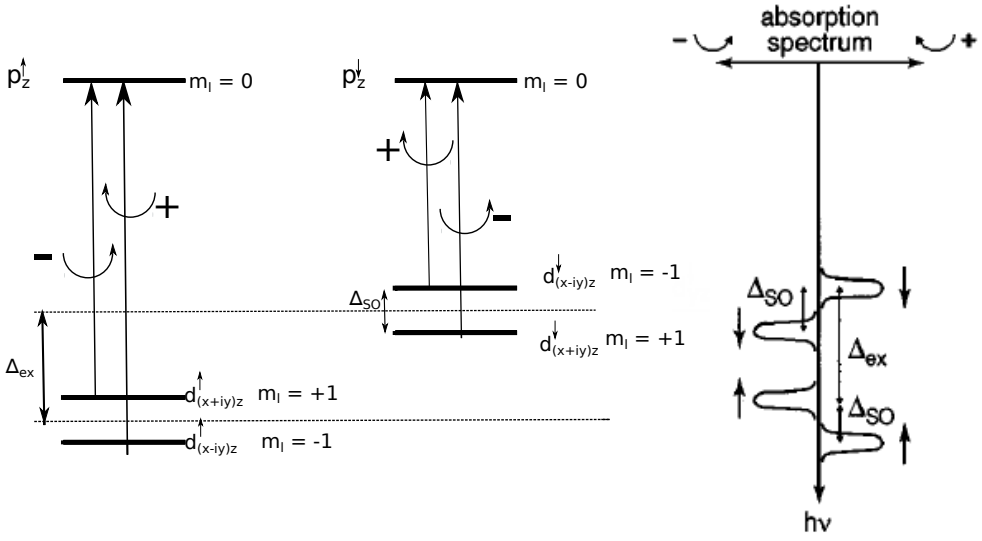

Figure 2.4: Left side: energy levels for a bulk ferromagnet reproduced from Ref. [42]. Transitions labelled with − correspond to absorption of RCP ($\Delta m_l = -1$); with + to absorption of LCP ($\Delta m_l = +1$). The arrow refers to majority (↑) or minority (↓) electron levels. Δ_{ex} is the exchange splitting, Δ_{SO} the spin orbit splitting. Right side: absorption spectra versus photon energy corresponding to the transition in the left side of the picture. For each absorption peak it is highlighted if it corresponds to a majority or minority spin transition.

2.1.3 Polarization modulation of incident light: the use of the Photoelastic Modulator

Usually the Kerr signal is very small, on the order of $\sim 10^{-3}$ degree. It is thus common to use a modulation technique to measure it. How this can be done with a photoelastic modulator (PEM) is described in this section from a theoretical point of view. In the experimental set up section it is reported how a PEM works.

A PEM provides with polarization modulation of light before it impinges onto the sample. In a PEM the birefringence of a crystal is manipulated thanks to the photoelastic effect. The birefringence causes a phase retardation between RCP and LCP light; for linear polarized light this leads to a phase shift. The effect of PEM can be described through the Jones matrix formalism. The electric field of light **E** is decomposed into S and P components: $\mathbf{E} = \begin{pmatrix} E_S \\ E_P \end{pmatrix}$. The action of PEM is represented by the following matrix:

$$\mathbf{O} = \begin{pmatrix} e^{i\frac{\phi}{2}} & 0 \\ 0 & e^{-i\frac{\phi}{2}} \end{pmatrix} \tag{2.22}$$

the phase ϕ is variable with time $\phi(t) = \phi_0 sin(\omega_M t)$. Through ϕ_0 the maximum phase retardation between RCP and LCP light can be controlled.
In the following a typical configuration [44] to measure the complex Kerr rotation with the use of PEM is analysed. It can be anticipated that within this configuration the first harmonic of the response signal is proportional to the Kerr ellipticity, while the second harmonic to the Kerr rotation.
The Jones formalism is used, the incident light is expressed with the vector $\mathbf{E}^i = \begin{pmatrix} E_S^i \\ E_P^i \end{pmatrix}$.

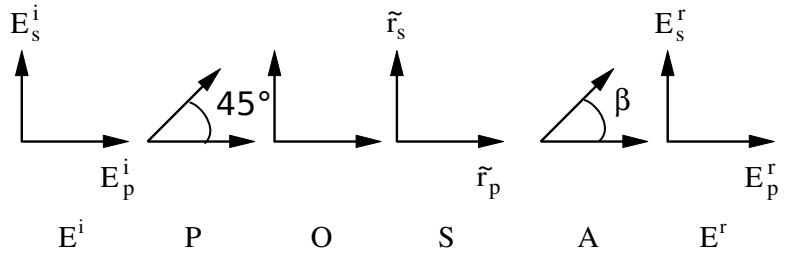

Figure 2.5: Description of the experimental configuration used to measure the Kerr effect. [45] For $\mathbf{E}^i$, incident, and $\mathbf{E}^r$, reflected, the two arrows represent the S and P components of the polarization, which are defined by the plane of incidence of the sample. **P** is a polariser with the axis at 45 degrees with respect to the plane of incidence. **O** refers to the PEM, **S** to the sample, only reflected light is considered. Finally **A** is an analyser with the axes at β angle.

The optical elements to be found in the path of light, reflected by the sample, are depicted in figure 2.5. This way to design them is useful for Jones formalism in which each optical element is represented by a matrix which describes how the S and P components are transformed after it. These matrices are now listed, the letters are associated to the optical elements as shown in figure 2.5. Matrix for **O** already written

in 2.22 is reported again for clarity

$$\mathbf{P} = \begin{pmatrix} \frac{1}{2} & \frac{1}{2} \\ \frac{1}{2} & \frac{1}{2} \end{pmatrix} \tag{2.23}$$

$$\mathbf{O} = \begin{pmatrix} e^{i\frac{\phi}{2}} & 0 \\ 0 & e^{-i\frac{\phi}{2}} \end{pmatrix}$$

$$\mathbf{S} = \begin{pmatrix} \tilde{r}_p & \tilde{r}_{ps} \\ \tilde{r}_{sp} & \tilde{r}_s \end{pmatrix} \tag{2.24}$$

$$\mathbf{A} = \begin{pmatrix} cos^2\beta & sin\beta cos\beta \\ sin\beta cos\beta & sin^2\beta \end{pmatrix} \tag{2.25}$$

For the reflectivity of the sample, the complex reflection coefficients can be expressed as:

$$\tilde{r}_A = r_A e^{i\delta_A} \tag{2.26}$$

where δ_A is the phase shift and $A = p, s, ps, sp$. For symmetry $\tilde{r}_{sp} = -\tilde{r}_{ps}$.
$\mathbf{E}^r$ is then found to be:

$$\mathbf{E}^r = \mathbf{ASOPE}^i \tag{2.27}$$

The calculation for the measured reflected light intensity $I^r = |E^r|^2$ can be found in [45] and is here reproduced. Performing the matrix calculation and defining $I^r = \tilde{I}\frac{I^i}{2}$, where $I^i = |E^i|^2$, it is found:

$$\begin{aligned} \tilde{I} = {} & r_p^2 cos^2\beta + r_s^2 sin^2\beta + r_{sp}^2 \\ & + r_{sp} sin2\beta[r_p cos(\delta_p - \delta_{sp}) - r_s cos(\delta_s - \delta_{sp})] \\ & + cos\phi[sin2\beta(r_s r_p cos(\delta_p - \delta_s) - r_{sp}^2) + \\ & + 2r_{sp}(r_s sin^2\beta cos(\delta_s - \delta_{sp}) + cos^2\beta cos(\delta_p - \delta_{sp}))] \\ & + sin\phi[r_s r_p sin2\beta sin(\delta_s - \delta_p) + \\ & + 2r_{sp}(r_s sin^2\beta sin(\delta_s - \delta_{sp}) + r_p cos^2\beta sin(\delta_p - \delta_{sp}))] \end{aligned} \tag{2.28}$$

To simplify the calculations the following parameters are defined:

$$A = r_p^2 cos^2\beta + r_s^2 sin^2\beta + r_{sp}^2 \tag{2.29}$$

$$+ r_{sp} sin2\beta[r_p cos(\delta_p - \delta_{sp}) - r_s cos(\delta_s - \delta_{sp})] \tag{2.30}$$

$$B = [sin2\beta(r_s r_p cos(\delta_p - \delta_s) - r_{sp}^2) \tag{2.31}$$

$$+ 2r_{sp}(r_s sin^2\beta cos(\delta_s - \delta_{sp}) + cos^2\beta cos(\delta_p - \delta_{sp}))] \tag{2.32}$$

$$C = [r_s r_p sin2\beta sin(\delta_s - \delta_p) \tag{2.33}$$

$$+ 2r_{sp}(r_s sin^2\beta sin(\delta_s - \delta_{sp}) + r_p cos^2\beta sin(\delta_p - \delta_{sp}))] \tag{2.34}$$

in order to obtain the following expression:

$$\tilde{I} = A + Bcos\phi + Ccos\phi \tag{2.35}$$

ϕ is time dependent: $\phi(t) = \phi_0 sin(\omega_M t)$ and expansion through the Bessel functions $J_k(k = 0, 1, 2...)$, of order k, gives:

$$sin(\phi_0 sin(\omega_M t)) = J_1(\phi_0) sin\omega_M t + 2J_3(\phi_0) sin3\omega_m t + ... \tag{2.36}$$

$$cos(\phi_0 sin(\omega_M t)) = J_0(\phi_0) + 2J_2(\phi_0) cos2\omega_m t + ... \tag{2.37}$$

Using eqns. 2.36 and 2.37 and keeping only terms up to the second harmonic, equation 2.35 becomes

$$\tilde{I} = \tilde{I}_0 + \tilde{I}_\omega sin\omega_M t + \tilde{I}_{2\omega} cos2\omega_M t \tag{2.38}$$

where

$$\tilde{I}_0 = A + BJ_0(\phi_0) \tag{2.39}$$

$$\tilde{I}_\omega = 2CJ_1(\phi_0) \tag{2.40}$$

$$\tilde{I}_{2\omega} = 2BJ_2(\phi_0) \tag{2.41}$$

To proceed, normal incident light is chosen, hence $r_p = r_s = r$ and $\delta_p = \delta_s = \delta$. A, B and C are now:

$$A = r^2 + r_{sp}^2 \tag{2.42}$$

$$B = sin2\beta(r^2 - r_{sp}^2) - 2rr_{sp}cos2\beta cos(\delta - \delta_{sp}) \tag{2.43}$$

$$C = 2rr_{sp}sin(\delta - \delta_{sp}) \tag{2.44}$$

The PEM phase amplitude $\phi_0 \approx 2.41$ corresponds to the zero of $J_0(\phi_0)$, the zero order Bessel function, that is $J_0(\phi_0) \approx 0$. With this choice and keeping in mind that $r_{sp}^2 \ll r^2$ and the definition for the complex Kerr rotation as in eqs. 2.9 2.10 it is obtained:

$$\frac{\tilde{I}_\omega}{\tilde{I}_0} = -4J_1(\phi_0)\epsilon_k^S \tag{2.45}$$

$$\frac{\tilde{I}_{2\omega}}{\tilde{I}_0} = 2J_2(\phi_0)\frac{sin^2 2\beta}{r} - 4J_2(\phi_0)cos2\beta\theta_k^S \tag{2.46}$$

The first harmonic signal is thus proportional to the Kerr ellipticity, while the second harmonic signal, if $\beta = 0$, is proportional to the Kerr rotation.

2.2 Experimental set up

Three possible geometries are used to detect the MOKE signal, as shown in figure 2.6. In the polar geometry the magnetization is perpendicular to the sample surface and parallel to the plane of incidence. In the longitudinal geometry the magnetization lies in the surface plane and is again parallel to the plane of incidence. The transversal mode has the magnetization parallel to the surface but perpendicular to the plane of incidence.

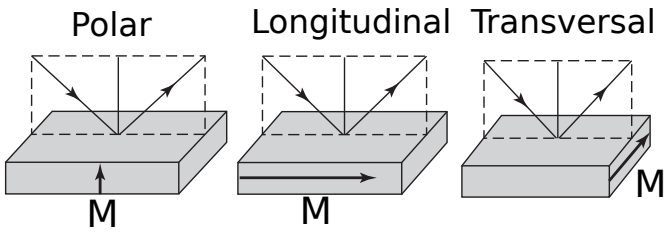

Figure 2.6: The three configurations for the detection of the MOKE rotation are shown. M refers to the magnetization. The dashed line represent the plane of incidence.

Measurements analysed in this thesis are taken in a polar geometry, with perpendicular

incidence.
MOKE is here used to investigate the magnetic samples in two configurations. In the static configuration the sample hysteresis loop is measured. The time resolved (TR) configuration is used to detect demagnetization curves of the sample. A pump and probe set up is implemented, where the probe beam measures the MOKE.
In this thesis mainly the TR configuration is used. For the sake of simplicity, the static configuration is first described, with all the optical elements which are necessary to detect a Kerr rotation. Then the further components necessary for TR measurement are discussed.

2.2.1 Static MOKE set up

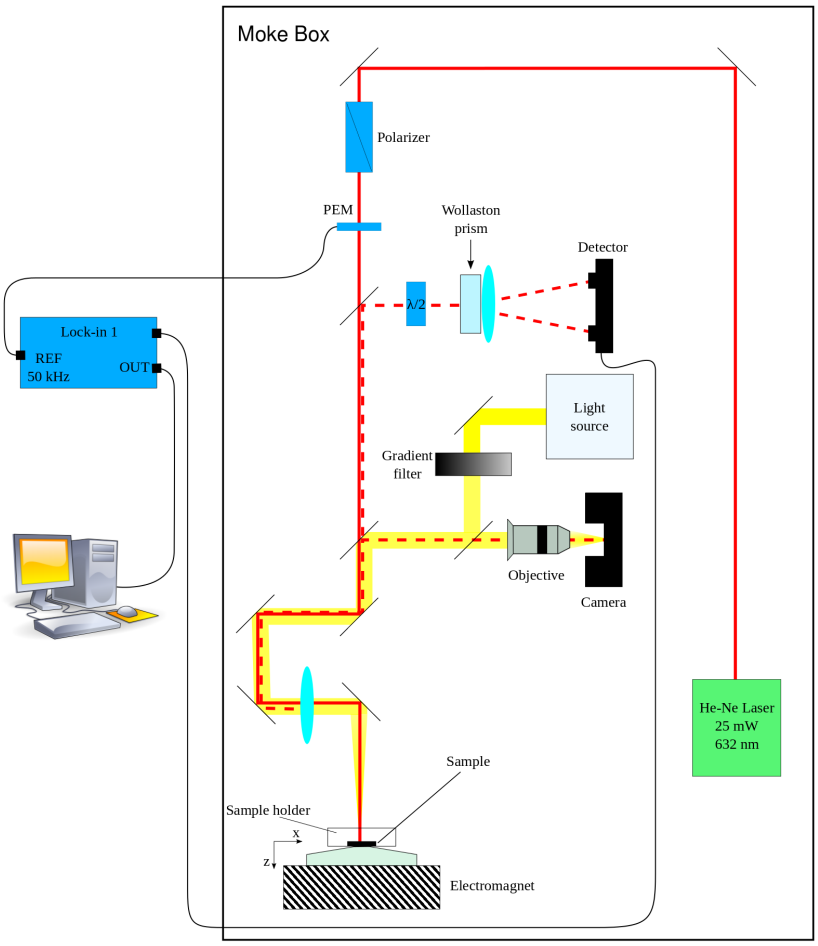

Figure 2.7: Experimental set up for the measurement of the static MOKE.

In figure 2.7 a sketch of the static configuration used to perform hysteresis loop measurements is reported. A He:Ne laser at 633 nm, 25 mW is used. It provides linear polarization. The first optical element in its path is a polariser with its axis at 45 degrees with respect to the optical table. It is followed by the PEM, which modulates the polarization of the laser field, as analysed in the previous section through the Jones formalism. This device is based on the photoelastic effect: some transparent material, for instance fused Silica, under strain becomes birefringent. The optical element is a bar of such a material, attached to a piezoelectric transducer that oscillates longitudinally with a frequency of 50 kHz, resonant to the mechanical oscillation of the system. Thanks to the polariser, the light sent to the PEM has a component both in the longitudinal axis of the PEM and in the vertical one. When the optical element is compressed, the longitudinal component is faster than the vertical, when it is stretched the contrary holds. This causes a phase retardation that oscillates with time, due to the strain oscillation. In figure 2.8 the case when the maximum of the phase retardation is equal to $\lambda/4$ ($\frac{\pi}{2}$ rotation) is shown. It acts as a $\lambda/4$ plate: when the phase retardation is at its maximum, the polarization is RCP, when at its minimum LCP. The intermediate states are elliptical and linearly polarized.

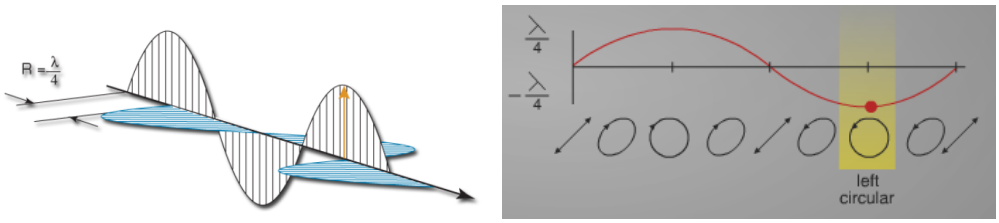

(a) (b)

Figure 2.8: Effect of the PEM. In (a) a phase retardation equal to $\lambda/4$ between the vertical and longitudinal component of the polarization is shown. In (b) the red sin function shows the phase retardation with respect to time. The effect of this retardation is sketched below. When the phase retardation crosses zero is linear, at the peak circular and between elliptical. Picture taken from http://www.hindsinstruments.com/knowlege-center/technology-primer/pem-100photoelastic-modulation/.

After the modulation, a lens focuses the laser beam, and the sample is positioned in its focus. The sample holder can be moved along the three axes. Close to the sample, an electromagnet produces a magnetic field perpendicular to the sample surface that magnetizes the sample. It is formed by an iron core and a coil around it and is controlled by a controller. The iron core ends with a tip, the sample is near this tip, where the

field is strong and uniform. This electromagnet can accept a current up to 50 A.
The sample is illuminated with white light, whose intensity can be varied by a graduated filter, allowing to image the sample surface. The white light is superimposed with the laser beam and it is focused onto the sample surface by the lens. The white light and laser radiation are reflected by the sample. When one wants to have an image of the sample, both are collected and detected by an objective and a camera.
During the measurement, the white light is off and the reflected laser beam, carrying the Kerr rotation, is sent into the detector line. The detecting technique has been installed during this thesis work. A balanced detector is used. It has two photodiodes and it measures the intensity difference between the light impinging onto the two of them. A Wollaston prism divides the S and P polarization, each of them is sent to one of the two photodiodes of the detector. The measurement of the Kerr rotation is made measuring the difference between the two components. The measurement of a difference instead of an absolute value reduces the signal to noise ratio. Before the Wallaston prism, a $\lambda/2$ allows to manually control the ratio between S and P polarised light and test the sensitivity of the detector.
The Kerr signal is modulated with 50 kHz by the PEM, a lock in amplifier extracts the first harmonic of the modulated signal. It was shown in the previous section that the first harmonic signal is proportional to the Kerr ellipticity.
The lock in output is sent to a computer, which communicates also with the magnet controller. A lab-view program allows to measure the hysteresis loops. Through a graphic interface, one can choose the current range and the number of steps for the measurement. In the same run, a hysteresis loop is measured several times. In this way, for each value of the current, the measured intensity is averaged all over the different measurements. The error associated to each point is the standard error. A calibration is

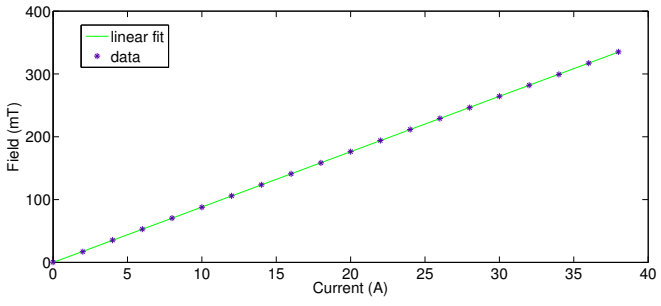

Figure 2.9: Calibration curve: applied magnetic field as a function of the current. Distance between the magnet tip and the sensor: 1.75 mm.

done to relate the current to the applied magnetic field, measured by a Gaussmeter. In figure 2.9 a calibration curve is shown, here the magnetic field corresponds to the field at a distance of 1.75 mm from the tip, which is usually the distance used to measure. A linear fit is also reported.
In figure 2.10 two examples of hysteresis loops measured with the set up just described are shown. In (a) 3 loops are averaged and in (b) 9 loops are averaged; errorbars refers to the standard error. Errorbars are very narrow and the ratio between the hysteresis loop amplitude and the maximum value for the standard error is 130 for 2.10(a) and 60 in 2.10(b). To obtain such narrow errorbars it is not required to average over a great number of loops, 3 seems enough. Such a low noise is due to the presence of the lock in amplifier and of the balanced detector.

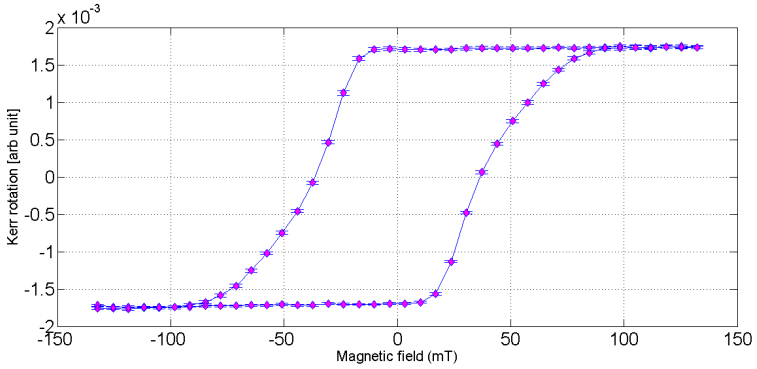

(a) Co/Pt ML with a 8.8 nm magnetic film thickness. In detail: [Pt(3 nm)/[Co(0.4 nm)/Pt(0.7 nm)]$_{\times 8}$/Pt(1.3 nm)] grown on Si_3N_4.

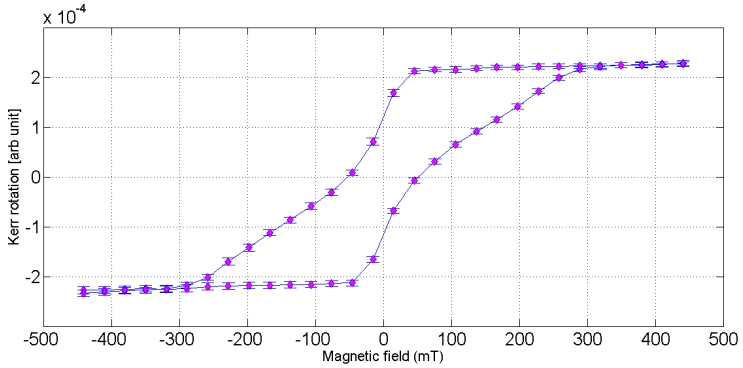

(b) Co/Pt ML with a 24.2 nm magnetic film thickness. In detail: [Ta(2 nm)/Pt(3 nm) /[Co(0.8 nm)/Pt(1.4 nm)]$_{\times 11}$/Pt(0.6 nm)] grown on Si wafer.

Figure 2.10: Hysteresis loop of two different Co/Pt ML acquired measuring the MOKE effect with the experimental set up shown in figure 2.7.

2.2.2 Time resolved (TR)-MOKE set up

The main difference in the TR configuration is the presence of two laser beams: 800 nm for the pump beam, which excites the sample, and 400 nm beam, which acts as the probe and measures the MOKE effect. Both of them must be pulsed to realise ultrafast dynamics measurements. The configuration useful for the TR measurement is shown in figure 2.11.
The short laser pulses are provided by a Titanium:sapphire (Ti:Sa) laser, which has a crystal of sapphire (Al_2O_3) doped with Titanium ions as the gain medium and is pumped by a 532 nm diode laser (4.5 W, Coherent, Verdi G). It gives laser pulses centred at 800 nm with a repetition rate of 54 MHz. These pulses are sent to a pulse switch working with an Acousto-Optic Modulator. In this way it is possible to have laser pulses with lower repetition rate but higher energy per pulse. The pulse switch cavity laser provides pulses with 40 nJ energy per pulse and temporal width of 120 fs, at a repetition rate of 545 kHz. The temporal width has been measured by an autocorrelator. The output radiation of the cavity is P polarised.
A beam splitter divides the beam in two beams, the reflected one will be used as the pump beam, while the transmitted beam, after doubling its frequency, as the probe. The two different paths are now described.
The transmitted beam is sent to a frequency doubler which works with a BBO (Barium Borate) crystal. The output of this cavity is the pulsed laser beam at 400 nm S polarised. The next optical element is a $\lambda/2$ plate, which rotates the S polarization to P polarization. A prism compressor compensates for the dispersion of optical elements such as the PEM and the microscopic objective, described in the following.
At this point it is sent to the MOKE optical table, where it is modulated by the PEM, as the He:Ne laser before.
Regarding the pump beam, after reflection by the beam splitter, it is reflected by two perpendicular mirrors, standing on a delay stage (Physik Instrumente, M-531.DD), whose position can be varied with a resolution of less than $1\mu m$. Moving this delay stage the optical path of the pump beam is changed, in this way the delay between the pump and the probe beam can be controlled. The spatial resolution of 1 μm for the delay stage movement correspond to a 3 fs temporal resolution for pump and probe delay. After the delay stage a $\lambda/2$ plate and a polariser can be found. With a fixed polariser position, movement of the $\lambda/2$ plate allows to control the pump power, or fluence (the fluence is defined as the ratio between pump pulse energy and spot area). Then two lenses form a telescope; the two focal lengths, f_1 and f_2, can be chosen to

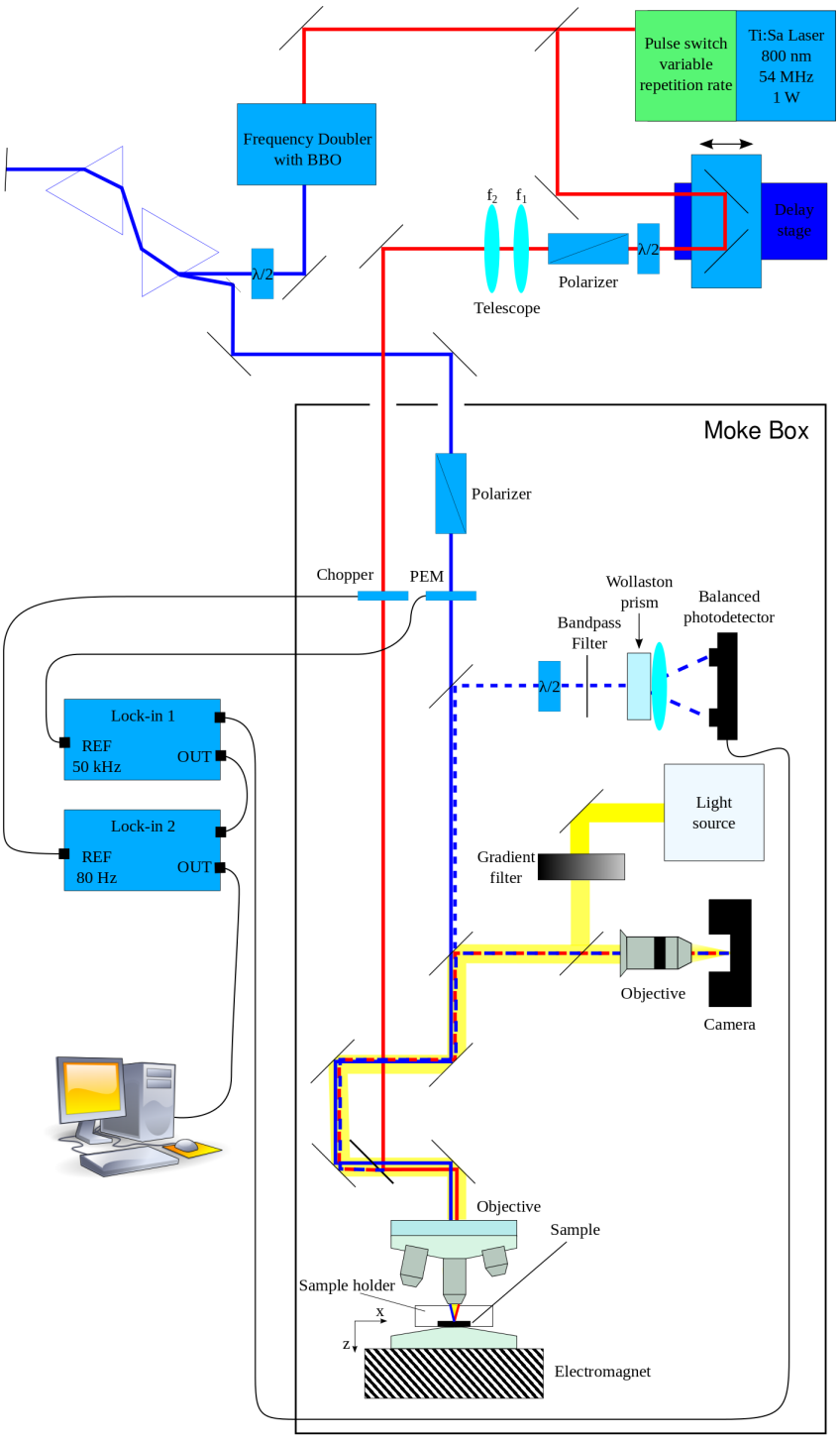

Figure 2.11: Experimental set up for the measurement of the TR-MOKE in a pump and probe technique. The read beam represent the 800 nm pump light; the blue beam represent the 400 nm probe light.

control the beam magnification $M = -\frac{f_2}{f_1}$. A chopper, rotating at 80 Hz, modulates the pump beam.
In the MOKE optical table, the path of the probe beam, after the PEM, and of the pump beam, after the chopper, become collinear, due to a system of mirrors. Both of them are focused onto the sample by a microscopic objective. The microscopic objective allows smaller focus size than a lens and has chromatic corrections to avoid different focal lengths for the two wavelengths. It gives also better imaging qualities. Unfortunately, it introduces a strong Faraday rotation. For the TR configuration this is not a problem, because only the polarization changes due to the pump excitation are detected. It cannot be used to measure hysteresis loops and does not allow to measure the absolute value of the demagnetization. Additionally it introduces significant dispersion, which is pre-compensated by the prism compressor.
The two beams at the sample surface have a temporal width of 200 fs, determined by an autocorrelation measurement.
The same system of sample holder, electromagnet, imaging and detection technique, described for the static configuration is used here. The electromagnet provides for the saturation field, necessary to magnetized the sample. In this case the imaging system has an additional role: it defines the distance between the microscopic objective and the samples. This distance is important because the sample must be in focus and the sample holder and the microscopic objective are frequently moved in the process of alignment. Once the desired distance between the two is optimized, by measuring the spot size in the z direction as it is reported in the next section, the camera is moved until the sample surface is in its focus. The camera is now kept fixed. To find the optimized distance between the microscopic objective and the sample it is now sufficient to adjust it until the camera image is in focus.
In this case, the signal is modulated by two frequencies, the 80 Hz of the chopper, and the 50 kHz of the PEM. Two lock-in amplifiers are employed to extract the double modulated signal. The detector output signal is sent to a lock-in, whose reference frequency is 50 kHz. Its output is the input of a lock-in with 80 Hz reference frequency. The 80 Hz lock-in output is the signal collected by the computer.

Running a measurement and data acquisition

Time resolved measurements are performed by changing the delay between the pump and probe beam step by step and acquiring the Kerr signal for each time-step. The measurement starts at a delay that corresponds to the temporal overlap, i.e. the time

zero. The two beams must be spatially overlapped, to be sure that the 400 nm beam probes only the excited area. For the spatial overlap, the power of the pump beam is increased and sent to the sample in order to burn a hole. Without moving the pump beam, the probe beam is then moved in the hole, with the help of the imaging system. The sample is translated to a fresh spot and with the two beams being spatially overlapped the measurement can start. Thanks to a lab-view program which communicates with the delay stage controller the different delay positions are set. For each position the detector signal is saved. Several loops are performed in order to take the average for each position.

2.3 Setting the focus spot size at the sample surface

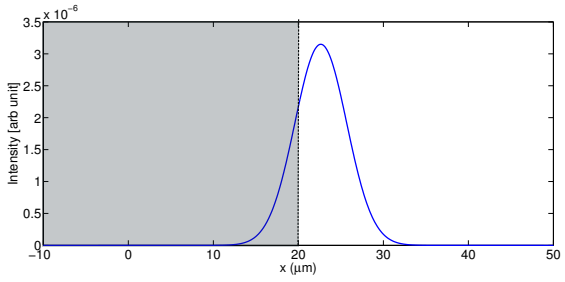

(a)

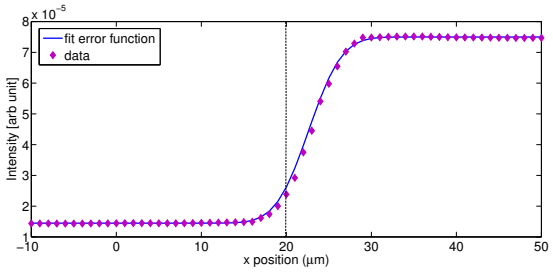

(b)

Figure 2.12: (a) Gaussian intensity profile in the x axis of the probe beam at a fixed z position. The vertical dashed line represent the knife edge and the grey part indicate the region of the beam covered by the knife. (b) Dotted points are the intensity measured scanning the gaussian. The dashed line refers to the same x position as in (a). The solid line is the fitted error function. The fit gives for the FWHM= $3\mu m$. The fit parameters were used to reconstruct the gaussian function in (a).

For the pump and probe scheme it is necessary for the probe spot size to be smaller than the pump spot size. In this way the former probes just the region previously

excited by the pump. The beam diameter of the two beams is measured with respect to the z-position (the axis are shown in figure 2.11) in order to be sure that this condition is satisfied. In addition knowing the dimension of the beam spot allows to quantify at what fluence the sample is excited.
For each z position, the beam intensity profile is assumed to be gaussian both in the x and in the y direction. To obtain the FWHM, a photodiode measures the beam intensity, while a sharp knife moves along x or y direction and progressively covers the beam. For each horizontal or vertical position the intensity that reaches the photodiode is measured. The knife is displaced thanks to a piezostage which can be moved in the three axis with nanometer precision. In figure 2.12(a) a gaussian curve is reported, it describes the intensity profile in the horizontal x direction, for a fixed z position. In figure 2.12(b) the measured intensity for each knife edge position is reported. It is the integral of a gaussian,hence it can be fitted with an error function and the FWHM is obtained as a fit parameter, FWHM= $3\mu m$ in the figure. Repeating these steps for

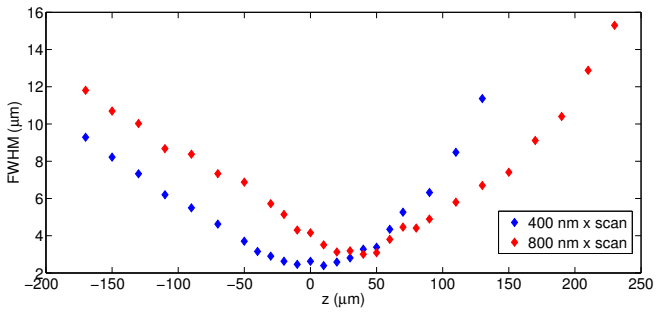

(a) Horizontal scan

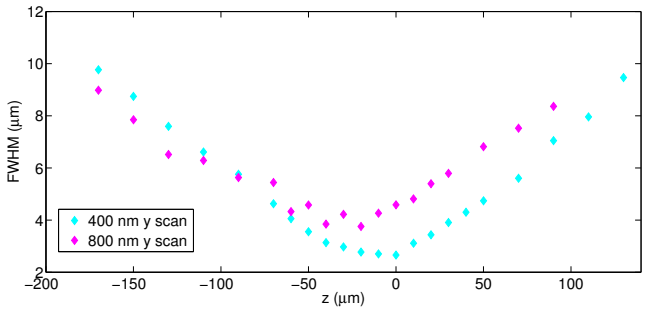

(b) Vertical scan

Figure 2.13: Beam diameter of the pump and the probe beam acquired scanning in the horizontal (a) and vertical (b) direction with respect to the z position. Measurement taken with telescope lens f_1=100 mm and f_2=-50 mm.

different z position gives the knowledge of the beam diameter in the x direction as a function of z.
The first measurement was run with the telescope formed by two lenses with focal length f_1=100 mm and f_2=-50 mm ($M = 0.5$). In figure 2.13 (a) the horizontal diameter for the two beams is shown, while in 2.13 (b) the vertical diameter. The pump diameter is not clearly larger than the probe diameter.
For a gaussian beam of wavelength λ and beam diameter D, focused by a lens with focal length f, the focus size $F.S.$ is

$$F.S. = \frac{4\lambda f}{\pi D} \tag{2.47}$$

To increase it the beam diameter D before the microscopic objective must be smaller. The telescope lenses are then changed: f_1=250 mm and f_2=-100 mm; now $M = 0.4$. In addition, the position of the telescope lenses are varied to tune the divergence of the beam and change the focus position of the microscopic objective. Figure 2.14 shows that now the pump beam is safely bigger than the probe, the $z = 0$ has been chosen to fulfil this requirement in such a way that this condition is satisfied even if the z position slightly changes.
The beam diameters (FWHM) in the x and y direction are now:

$$D_x(@400nm) = 2.7\mu m \qquad D_y(@400nm) = 2.5\mu m \tag{2.48}$$

$$D_x(@800nm) = 6.7\mu m \qquad D_y(@800nm) = 7\mu m \tag{2.49}$$

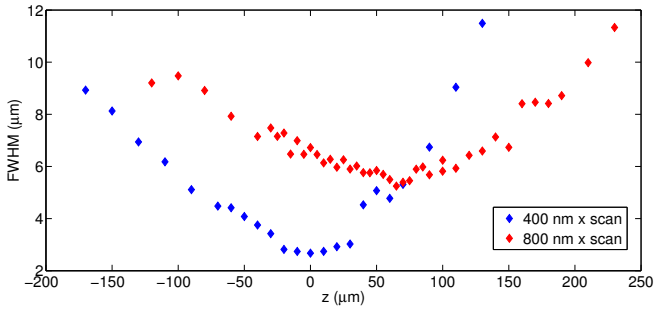

(a) Horizontal scan

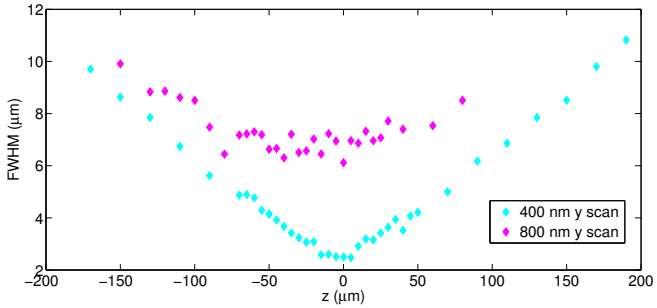

(b) Vertical scan

Figure 2.14: Beam diameter of the pump and the probe beam acquired scanning in the horizontal (a) and vertical (b) direction with respect to the z position. Measurement taken with telescope lens f_1=250 mm and f_2=-100 mm.

Chapter 3

Fitting and features of demagnetization curves

3.1 Motivation and contents

The most important and revealing parameters in ultrafast demagnetization process in ferromagnetic materials are the demagnetization (τ_M) and remagnetization time constants (τ_E).
Since the Beaurepaire et al. paper [1] was published, a lot of experimental and theoretical works have tried to explain this process. The extremely low demagnetization timescale revealed that the usual channels for dissipation of angular momentum were not enough. In literature, values of τ_M given in different papers are compared, to infer trends and differences. For instance, Vodungbo et al. in [10] give experimental evidence for the role of superdiffusion, observing a faster local demagnetization in each domain than what is usually observed in uniformly magnetized samples.
It is thus of fundamental importance to pay attention to the models used to obtain these time constants and to define when different results can be compared. In addition the dependence on fluence of typical timescales must be investigated in order to let the different groups working on this process compare each other's results.

Examples of demagnetization curves at different pump fluences acquired in the present work are shown in figure 3.1. To start with, such curves must be fitted in order to obtain the time constants for demagnetization and remagnetization processes. Since the process of ultrafast demagnetization is not fully understood, it is not clear which is the best function to fit demagnetization curves. Examples can be found in literature, mostly based on the Three temperature model (3TM). [15]

This problem is not unknown in the ultrafast magnetism community, Koopmans in [14] has already mentioned it, giving examples of the incongruity of different models.
The aim of this chapter is to exploit this problem in a systematic way, using different functions to fit the data shown in figure 3.1. It will be discussed later that results are different from one model to another, especially for the demagnetization time scale, even if the goodness of fitness parameters is satisfying for all the reported models.

In the second part of the chapter, the typical behaviour of these curves with respect to pump fluence are highlighted.

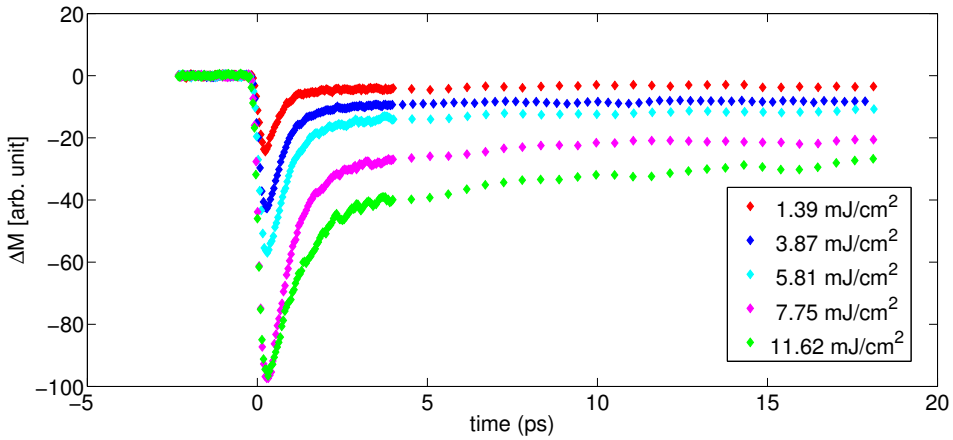

Figure 3.1: Demagnetization curves measured on a 24.2 nm Co/Pt ML.

3.2 Fitting demagnetization curves

Roughly speaking, when you want to fit experimental curves, two different approaches can be followed: choosing an empirical function that enables a good approximation of your data or following a model which describes the system under study.
Regarding demagnetization curves, a model exists for early times: the 3TM.

3.2.1 Electron and spin dynamics after a laser pulse excitation.

What happens in a metal after it is excited by a laser pulse?
3TM describes the macroscopic dynamics of a system after a laser excitation. The main idea of this model was presented in Chapter 1 together with the coupling equations for electron (T_e, C_e), lattice (T_l, C_l) and spins (T_s, C_s) system. These equations are in the following reported again for clarity.

$$C_e \frac{dT_e}{dt} = -G_{el}(T_e - T_l) - G_{es}(T_e - T_s) + P(t) \quad (3.1)$$

$$C_l \frac{dT_l}{dt} = -G_{el}(T_l - T_e) - G_{sl}(T_l - T_s) \quad (3.2)$$

$$C_s \frac{dT_s}{dt} = -G_{es}(T_s - T_e) - G_{sl}(T_s - T_l) \quad (3.3)$$

Subsequently the macroscopic analysis of the 3TM given in [14] is followed to discuss the excitation and relaxation processes, considering the internal dynamics of each subsystem.

Electron-electron scattering

When laser light impinges on a metal, its energy is taken by the electron system. To start with, the dynamics of this system is thus considered.
Figure 3.2 depicts the density of states (DOS) as a function of energy for electrons after an optical excitation.
Exciting a metal with a visible or near visible light source causes excitation of the electrons, which occupy the states above the Fermi energy(Fig. 3.2(I)). The system experiences at this stage a non equilibrium between "hot" electrons, the ones above the Fermi energy, and "cold" electrons, which are under the Fermi level; and between "hot" electrons and the lattice.

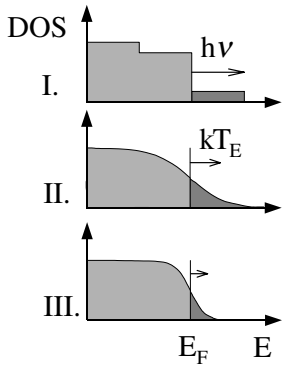

Figure 3.2: Electron distribution in the process of light excitation of electrons and the following relaxation. I) Electrons are excited above the Fermi energy. II) Electron distribution after internal thermalization at a higher temperature T_e. III) Electron distribution after electron thermalization with the lattice. Figure taken from [46]

The process of internal thermalization of electronic system (figure 3.2II) cannot be

described by the 3TM because there is no equilibrium between electrons and they do not have a temperature.
In spite of this, a temperature $T_{e,E}$ is often defined [14] from the excess energy E_{ex} given to the system, through the relation between it and temperature: $E_{ex} = \frac{1}{6}\pi^2 D_F (k_B T_{e,E})^2$, which is true for a metal with a constant density of states D_F.
An electron temperature $T_{e,F}$ can be alternatively defined using the slope of the electron distribution function $f(E)$ at the Fermi energy, in analogy with an electron thermalized distribution. The increase in the electron temperature would then be:

$$\Delta T_{e,F} = \left(4k_B \frac{df(E)}{dE}\bigg|_{E_F} \right)^{-1} \tag{3.4}$$

If $T_{e,E}$ increases instantaneously after the laser excitation, this is not true for $T_{e,F}$, which increases with a typical time scale τ_T. τ_T can be understood as the thermalization time for the electronic system.
The following empirical equation can thus be used to describe the evolution of $T_{e,F}$ [14]:

$$\Delta T_{e,F} = \Delta T_1 [1 - e^{\frac{-t}{\tau_T}}] \tag{3.5}$$

ΔT_1, the rise of electron temperature, depends on the absorbed energy.

Electron-phonon scattering

Electron-phonon scattering processes recovers the equilibrium between these two subsystems(figure 3.2III).
This can be also described by the 3TM; using some approximations it is also possible to obtain equations which have an analytical solution. [15]
We assume

- C_e and C_l to be constant, which is a good approximation for low fluences.
- negligible specific heat of the spin system ($C_s = 0$). The magnetic contribution to the specific heat diverges for temperature value near T_C. For low enough temperature, which means again low fluence, this approximation is safe.
- any role for electron diffusion or heat diffusion, which means thin samples on insulating substrate. The importance of this approximation will be further discussed.

Particular attention is necessary for C_e, since it is proportional to the electron temperature through a proportionality parameter γ. Being Q the heat which flows into the system:

$$C_e(T_e) \equiv \frac{\partial Q}{\partial T_e} = \gamma T_e \tag{3.6}$$

Integrating the previous relation we obtain that if one gives to the system an energy of ΔQ, the increase in electronic temperature is

$$\Delta T_e = \sqrt{\frac{2\Delta Q}{\gamma}} \tag{3.7}$$

With a fluence of F=20 J m^{-2} and a penetration depth of $\delta = 13$ nm, values in the range used in the present work, the density of energy given to the system is $\frac{F}{\delta}$. For cobalt $\gamma = 704 \frac{J}{m^3 K^2}$. Thus the maximum increase of electronic temperature can be estimated as

$$\Delta T_{e,max} = \sqrt{\frac{2F}{\gamma\delta}} = 2090K \tag{3.8}$$

The initial electron temperature is 300 K, the maximum temperature reached is 2390K. The electronic heat capacity changes an order of magnitude.
According to this approximation for the heat capacities, the following coupling equations between the electron and the phonon systems are obtained:

$$C_e \frac{dT_e}{dt} = -G_{el}(T_e - T_l) \tag{3.9}$$

$$C_l \frac{dT_l}{dt} = -G_{el}(T_l - T_e) \tag{3.10}$$

These equations are solved by

$$T_e(t) = T_2 + [T_1 - T_2]e^{\frac{-t}{\tau_E}} + T(0) \tag{3.11}$$

$$T_l(t) = T_2[1 - e^{\frac{-t}{\tau_E}}] + T(0) \tag{3.12}$$

where $T(0)$ is the starting temperature of the system, $T_2 + T(0)$ is the temperature at which both the electrons and phonons converge and $\tau_E = \frac{C_e C_l}{C_e + C_l} \frac{1}{G_{el}}$.
This solution for T_e considers the electron temperature to increase up to T_1 instantaneously after the laser pulse ($\tau_T = 0$); on the contrary assuming a finite electron thermalization time, τ_T, leads to the following empirical equation for electronic tem-

perature:

$$T_e = T_1[1 - e^{\frac{-t}{\tau_T}}]e^{\frac{-t}{\tau_E}} + T_2[1 - e^{\frac{-t}{\tau_E}}] \tag{3.13}$$

It is easy to check that converging τ_T at zero, we get equation 3.11. In the limit of $\tau_T \ll \tau_E$ equation 3.13 provides for the peak observed in experimental T_e, obtained through reflectivity measurement [47]. In figure 3.3 evolution of electronic temperature as defined in equation 3.13 is shown (blue curve).
This model implies that the thermalization process between electrons and phonons takes place *after* the thermalization in the electron system. This is of course an additional approximation since electron-phonon scatterings starts at $t = 0$, but it is true that $\tau_T \ll \tau_E$.

Spin scattering

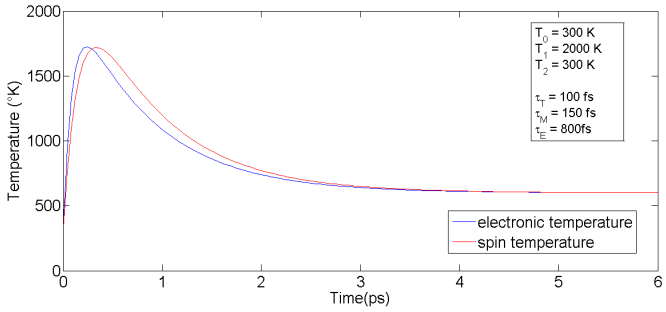

Figure 3.3: In the figure $T_e(t)$ and $T_s(t)$ are plotted as given by 3.13 and 3.15. In the text box parameters used are shown.

In order to obtain an equation for spin temperature we keep the same approximations used before for the heat capacities of the 3 subsystems and we consider $\tau_T = 0$, which means an instantaneous increase of electron temperature. This is equivalent to assume that the spin temperature is exclusively controlled by "hot" electrons and not by the thermalized ones.
The following equation [15] introduces two contributions for spin temperature, one due to electrons and the other to phonons, with two different timescales, $\tau_{M,e}$ and $\tau_{M,l}$

$$\frac{dT_s}{dt} = \frac{T_e - T_s}{\tau_{M,e}} + \frac{T_l - T_s}{\tau_{M,l}} \tag{3.14}$$

where $\frac{1}{\tau_{M,e}} = \frac{G_{es}}{C_S}$ and $\frac{1}{\tau_{M,l}} = \frac{G_{sl}}{C_S}$ according to equation 1.3.

Inserting the derived equation for electron and phonon temperature, we obtain:

$$T_s(t) = T_2 - \frac{(\tau_E T_1' - \tau_M T_2)e^{\frac{-t}{\tau_M}} + \tau_E(T_2 - T_1')e^{\frac{-t}{\tau_E}}}{\tau_E - \tau_M} + T_s(0) \tag{3.15}$$

where $T_1' = T_1 \frac{\tau_M}{\tau_{M,e}}$ and $\frac{1}{\tau_M} = \frac{1}{\tau_{M,e}} + \frac{1}{\tau_{M,l}}$.
This equation can be used to fit the MOKE signal, thanks to the linear relation between magnetization and spin temperature at low fluences. Due to the definition of τ_M, an *a priori* knowledge of which channel (electron or phonon) dominates in the spin temperature is not needed.
In figure 3.3 the function derived for $T_e(t)$ and $T_s(t)$ are plotted. Since $\tau_T \ll \tau_E$, the electron temperature has a quite steep increase at early times and then it decreases, thermalizing with phonons. It is therefore true that $\tau_T < \tau_M \ll \tau_E$. The spin temperature follows the electron temperature with a certain delay, presents again a peak and then thermalizes with the system.

3.2.2 Fitting functions found in literature

In this section, models used in literature to fit demagnetization curves are presented and explained.

Sum of two exponential functions

As previously stated, equation 3.15 for spin temperature can be used to describe the evolution of magnetization after a low intensity laser excitation.
For this purpose T_1 and T_2 must be converted into the two parameters A_1 and A_2, which will represent the fitting parameters together with τ_M and τ_E.
In addition, in order to describe the response function to the laser excitation, a convolution with a Gaussian $G(t)$ must be added, which it is assumed to represent the temporal evolution of the experimental set-up.
The fitting function, as given by Koopmans [14], will then be

$$\frac{\Delta M(t)}{M_0} = G(t) \otimes H(t) \left[A2 - \frac{(\tau_E A_1 - \tau_M A_2)e^{\frac{-t}{\tau_M}} + \tau_E(A_2 - A_1)e^{\frac{-t}{\tau_E}}}{\tau_E - \tau_M} \right] \tag{3.16}$$

$H(t)$ is the Heaviside step function, since it is assumed the excitation to be at $t = 0$.

Three exponentials used by Vodungbo [10]

Vodungbo et al. in [10] use the following function to fit their data.

$$\frac{\Delta M(t)}{M_0} = G(t) \otimes H(t) \left[A_1 (1 - e^{\frac{-t}{\tau_M}}) e^{\frac{-t}{\tau_E}} + A_2 (1 - e^{\frac{-t}{\tau_E}}) \right] \tag{3.17}$$

This is equivalent to equation 3.13 describing the electronic temperature, assuming a finite thermalization time. Vodungbo et al. take this function from Guidoni et al. [48]

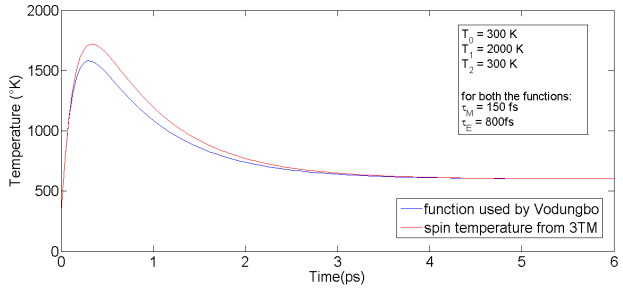

(a)

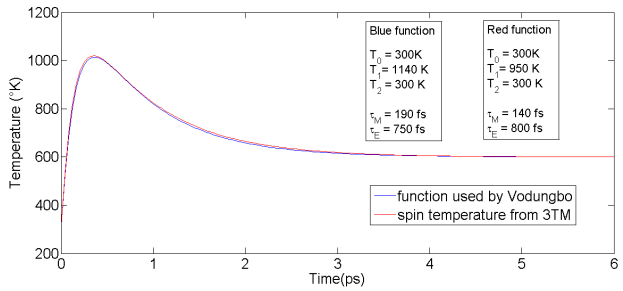

(b)

Figure 3.4: Comparison between the different expressions used for T_s in the 3TM and in Vodungbo et al.'s work. In a) the same value for τ_M was accounted. In b) time constants were chosen to make the two curves overlap each other.

where it is used to fit transmission and reflectivity data, which in a non-magnetic or non-magnetized sample represent the electronic temperature.
Equation 3.13 is derived considering the electronic system to internally thermalize with a timescale τ_T and then to thermalize with phonon with a timescale τ_E.
Concerning the spin system, in a complete parallelism with equation 3.13, one infers that τ_M represents a faster thermalization with electrons and τ_E the thermalization with phonons, or an external bath.

From figure 3.4, we have a hint on the results we can obtain using the two functions 3.16 and 3.17. The same value for τ_M in the two expressions leads to different curves (3.4a); to make the two curves overlap (as in figure 3.4b) a higher value for τ_M and T_1 in Vodungbo et al. function is needed. This discrepancy is expected when these two functions are used to fit the same data.
It should be mentioned that in [18] equation 3.17 is used without the second term in squared bracket:

$$\frac{\Delta M(t)}{M_0} = G(t) \otimes \left[C_0 + C_1 H(t)[1 - e^{\frac{-t}{\tau_M}}]e^{\frac{-t}{\tau_E}} \right] \tag{3.18}$$

The ignored term provides for the increase after the minimum, for this reason in [18] demagnetization curve are cut between 1 and 2 ps, and data are fitted just in this very small range. This function will thus not be used in this analysis, since it is preferred to keep the first increasing edge of demagnetization curves.

Heat diffusion

In demagnetization curves, the magnetization does not go back to M_S after the single increasing exponential function, which represents thermalization with phonons, because after this step the 3 subsystems will be at a higher temperature with respect to the starting temperature. Energy exchange with the surrounding of the excited area eventually re-establishes the initial condition on a longer time scale.
Looking at demagnetization curves (figure 3.1), it is clear that this heat diffusion must be considered in order to fit data measured for more than 4ps.
In literature there is no model to describe what happens in these later times. Heat diffusion is a complicated process to model, because it is not a 1D process and strongly depends on the geometry of the sample.
For this reason, functions to describe later times in demagnetization curves have been chosen only by checking if they describe the data appropriately; for instance in [15] a square root term is used, which is added to equation 3.16.
The resulting function is the following:

$$\frac{\Delta M(t)}{M_0} = G(t) \otimes H(t) \left[\frac{A_2}{\sqrt{1 + \frac{t}{\tau_0}}} - \frac{(\tau_E A_1 - \tau_M A_2)e^{\frac{-t}{\tau_M}} + \tau_E(A_2 - A_1)e^{\frac{-t}{\tau_E}}}{\tau_E - \tau_M} \right] \tag{3.19}$$

The additional constants τ_0 is related to the increasing rate of the square root term, which describes the last part of the curve. It must be thus true that $\tau_0 \gg \tau_M, \tau_E$.
For low excitation fluence, it is in general also sufficient to describe the slower changes of $\frac{\Delta M}{M_0}$ with a linear function:

$$\frac{\Delta M(t)}{M_0} = G(t) \otimes H(t) \left[A_0 t - \frac{(\tau_E A_1 - \tau_M A_2) e^{\frac{-t}{\tau_M}} + \tau_E (A_2 - A_1) e^{\frac{-t}{\tau_E}}}{\tau_E - \tau_M} \right] \tag{3.20}$$

To close with, we should highlight that the most natural choice for this third term would be a third exponential function, as done in [9]

$$\frac{\Delta M(t)}{M_0} = G(t) \otimes H(t) \left[A_0 e^{\frac{-t}{\tau_0}} + A_m e^{\frac{-t}{\tau_M}} + A_e e^{\frac{-t}{\tau_E}} \right] \tag{3.21}$$

It will be shown later that unfortunately this choice does not work, at least for the data presented in this thesis.

3.2.3 Analysis

In this analysis the data reported in figure 3.1 are fitted with the different functions summarized in the previous section. These demagnetization curves are taken on a sample based on Co/Pt multilayer (ML), with a thickness of 24.2nm and the following layer thickness [Ta(2 nm)/Pt(3 nm) /[Co(0.8 nm)/Pt(1.4 nm)]$_{\times 11}$/Pt(0.6 nm)]. Such thin multilayers of magnetic/non magnetic materials are often used in time resolved magnetism because, for particular layer thicknesses [49], they present a perpendicular anisotropy [50] [18], which makes the out of plane direction the easy magnetization axis and the polar MOKE set up can be used. The samples are deposited on the chosen substrate via ion-assisted DC magnetron sputtering.
The function used to fit these curves are here reported for clarity.

- *Functions for small temporal range data(from 0 up to 4 ps)*
  - sum of two exponential function derived by Koopmans, equation 3.16. From now on it will be referred as "exp + exp"

$$\frac{\Delta M(t)}{M_0} = G(t) \otimes H(t) \left[A2 - \frac{(\tau_E A_1 - \tau_M A_2) e^{\frac{-t}{\tau_M}} + \tau_E (A_2 - A_1) e^{\frac{-t}{\tau_E}}}{\tau_E - \tau_M} \right]$$

– function used in [10], equation 3.17 which will be called "Vodungbo" function.

$$\frac{\Delta M(t)}{M_0} = G(t) \otimes H(t) \left[A_1(1 - e^{\frac{-t}{\tau_M}})e^{\frac{-t}{\tau_E}} + A_2(1 - e^{\frac{-t}{\tau_E}}) \right]$$

- *Functions for large temporal range data (more than 4 ps range)* These functions are derived adding a third term to the two exponentials function 3.16, which describes the first picoseconds. The added term is chosen empirically and will represent heat diffusion.
  Data extending to over different temporal ranges will be fitted (10 ps, 18 ps or 30 ps) to investigate how the time constants change.
  We can distinguish these functions through the terms used for heat diffusion:

  – sum of two exponential functions + square root term, equation 3.19. It will be referred as "exp + exp + sqrt".

$$\frac{\Delta M(t)}{M_0} = G(t) \otimes H(t) \left[\frac{A_2}{\sqrt{1 + \frac{t}{\tau_0}}} - \frac{(\tau_E A_1 - \tau_M A_2)e^{\frac{-t}{\tau_M}} + \tau_E(A_2 - A_1)e^{\frac{-t}{\tau_E}}}{\tau_E - \tau_M} \right]$$

  – sum of two exponential functions + linear function, equation 3.20 named as "exp + exp + lin"

$$\frac{\Delta M(t)}{M_0} = G(t) \otimes H(t) \left[A_0 t - \frac{(\tau_E A_1 - \tau_M A_2)e^{\frac{-t}{\tau_M}} + \tau_E(A_2 - A_1)e^{\frac{-t}{\tau_E}}}{\tau_E - \tau_M} \right]$$

  – sum of three exponential functions, "exp + exp + exp"

$$\frac{\Delta M(t)}{M_0} = G(t) \otimes H(t) \left[A_0 e^{\frac{-t}{\tau_0}} + A_m e^{\frac{-t}{\tau_M}} + A_e e^{\frac{-t}{\tau_E}} \right]$$

3.2.4 Results

Fitting the curves in figure 3.1 with the different functions reported above leads to different results for τ_M and τ_E, which represents demagnetization and remagnetization times, respectively. Regarding the goodness of these best-fit, it should be emphasized that all of them, except the three exponentials function, are good and reliable. The confidence interval for fit parameters are not too large and the R-square adjusted to the degree of freedom, which must be 1 for a perfect fit function, is approximately the same for all the fits and higher than 0.995.
In figure 3.5 time constants obtained from all the different fitting functions reported in

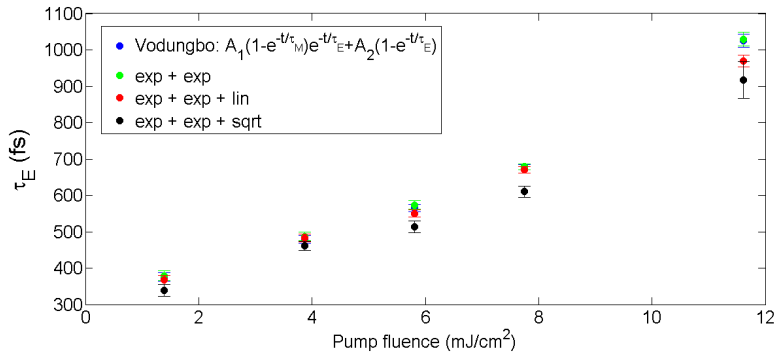

(a) Remagnetization time

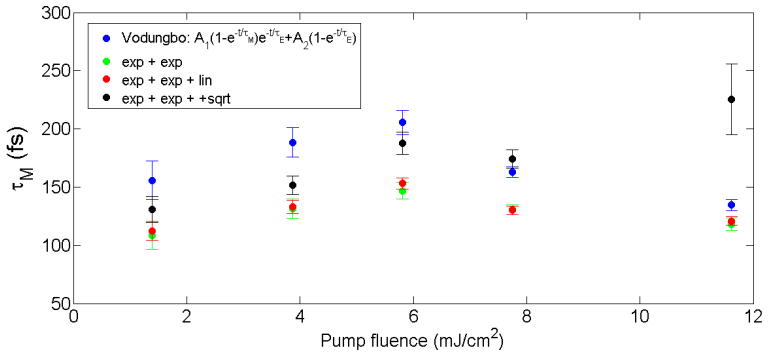

(b) Demagnetization time

Figure 3.5: Time constants as a function of fluence obtained from measurement on 24.2nm Co/Pt ML at different fluences. The different results are due to different fitting function used, as reported in the legend.

the previous section are shown.

The biggest discrepancy is found in the demagnetization times, which can differ by 50fs from one fit to another, for values of τ_M that varies from 100fs to 200fs.

Figure 3.6 allows one to focus only on the difference in τ_M obtained with the two small range functions ("exp+exp" eq. 3.16 and "Vodungbo" eq. 3.17). These two functions have a meaningful difference in describing the first picoseconds, in fact the difference in τ_M is the most remarkable (50fs) and the value is higher for the "Vodungbo" function. This is consistent with figure 3.4, where the two functions have the same shape but a difference of 50 fs for τ_M.

Changes in the remagnetization times are less dramatic: the absolute differences are similar but values for τ_E are included in the range [300 fs, 1000 fs]. Values obtained for

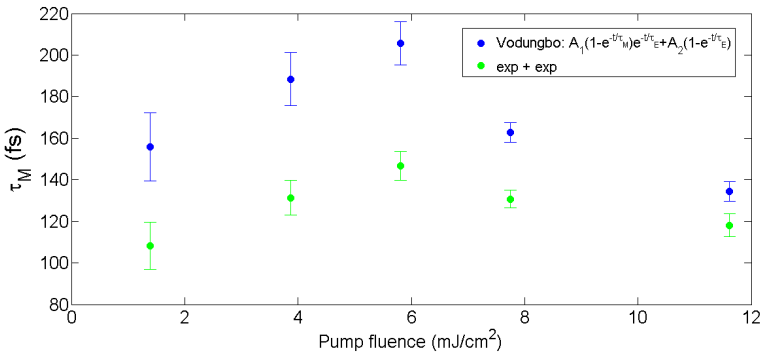

Figure 3.6: Demagnetization time τ_M as a function of fluence. The fitting function compared in this figure are 3.16 and 3.17.

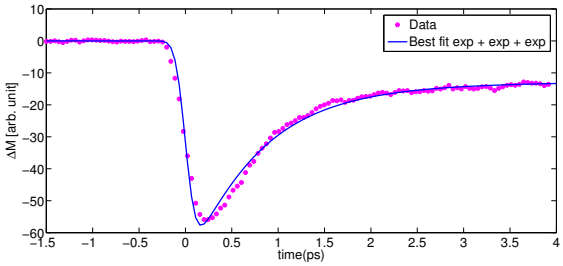

(a) fitting function "exp+exp+exp"

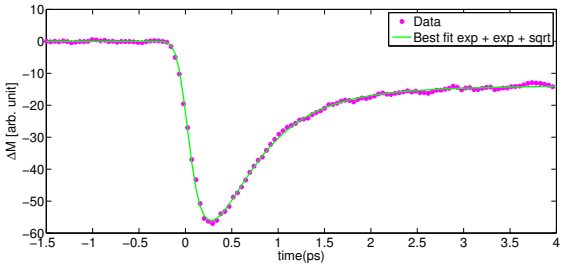

(b) fitting function "exp+exp+sqrt"

Figure 3.7: Best fit using in (a) the three exponential fit function and in (b) the two exponential plus a square root function of the curve taken with a fluence of 6 mJ/cm^2. In (a) the function does not fit the curve in the decreasing edge. The fits are done for a time range of 18 ps, here only the first 4 ps are shown.

τ_E using the two different small range functions ("exp + exp" eq. 3.16, "Vodungbo" eq. 3.17) are very similar to each other but they change consistently, fitting a long range curve. The trend of τ_E with fluence does not change in the different fits and we can

only see a shift in the absolute values; this is not true for the demagnetization time, especially at high fluences.

The next step is to focus on what happens adding a third term for later times.
To start with, it will be shown that the three exponential function, eq. 3.21, is not working well, as can be seen from the fits in figure 3.7, where only the first 4ps are shown.
This function does not fit the data especially in the decreasing edge, this does not permit to have meaningful value for τ_M.
In figure 3.7(b) an example of what is obtained when the function "exp + exp + sqrt" is used. Here the function follows appropriately the data point in the decreasing edge and τ_M given as a fit parameter is reliable. The value of the adjusted R-square

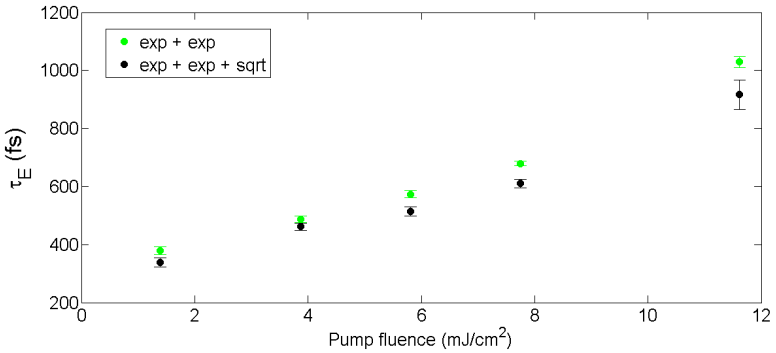

(a) Remagnetization time

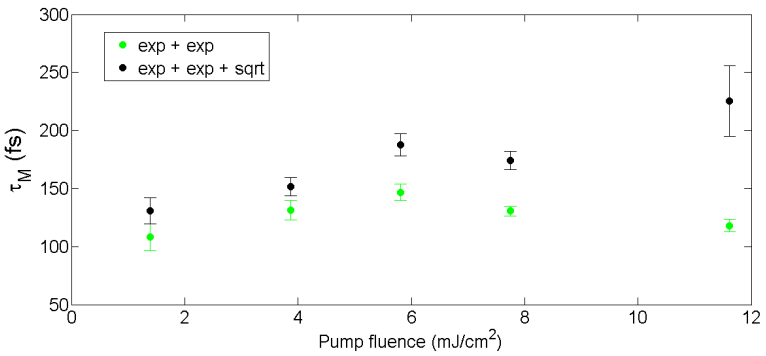

(b) Demagnetization time

Figure 3.8: Time constants as a function of fluence obtained as the fitting parameter for 3.19 and 3.16.

for the fit in figure 3.7(a) 0.9911 is not far worse than in (b) 0.9987, because the three

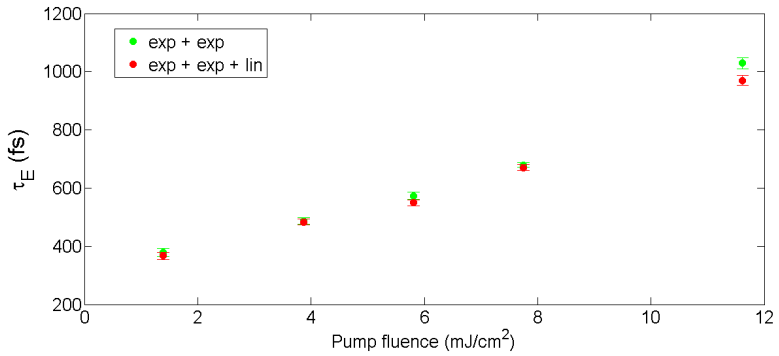

(a) Remagnetization time

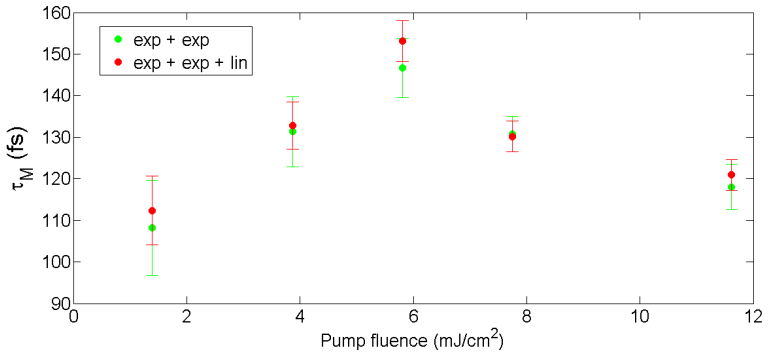

(b) Demagnetization time

Figure 3.9: Time constants as a function of fluence obtained with fitting function 3.20 and 3.16.

exponential function is only failing in the decreasing edge, whereas the rest of the curve is oversampled and shows good agreement. For a valid τ_M it is necessary to have a good fitting function for the decreasing edge. For this reason the "exp + exp + exp" function is not considered any further.

Adding a third term to describe the response at later time points can change the time constants for the first picoseconds behaviour considerably. Comparing the fit results obtained adding a square root (figure 3.8) or the linear function results (figure 3.9), it is clear that the most remarkable changes take place for the square root function. The linear function ("exp + exp + lin") influences τ_E and τ_M less than the square root ("exp + exp + sqrt").

It appears that adding the third term increases the demagnetization time and decreases the remagnetization time. Paying attention to figure 3.8 at the highest fluence, we

should highlight that this simple shift seems to not be enough to explain what happens fitting at higher fluences.

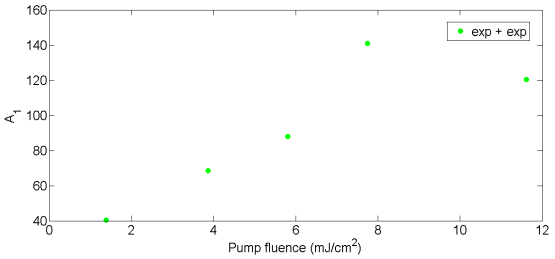

(a) A_1 parameter obtained with 3.16.

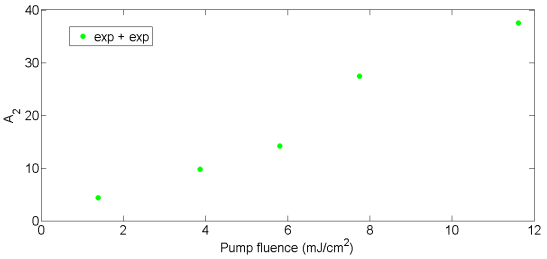

(b) A_2 parameter obtained with 3.16.

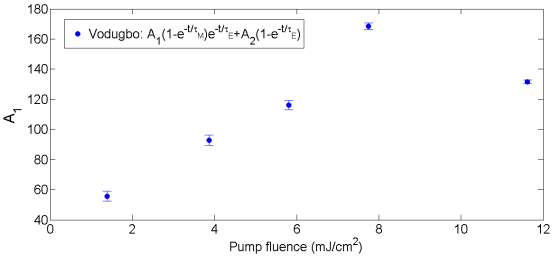

(c) A_1 parameter obtained with 3.17.

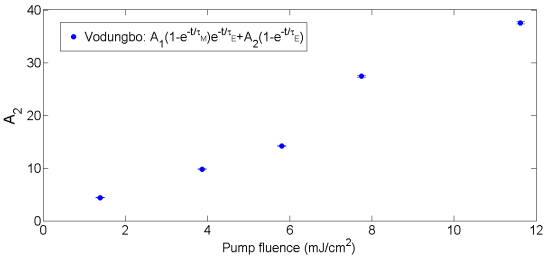

(d) A_2 parameter obtained with 3.17.

Figure 3.10: A_1 and A_2 parameters as resulting from best-fit to data using equation 3.16 in (a) and (b) and equation 3.17 in (c) and (d).

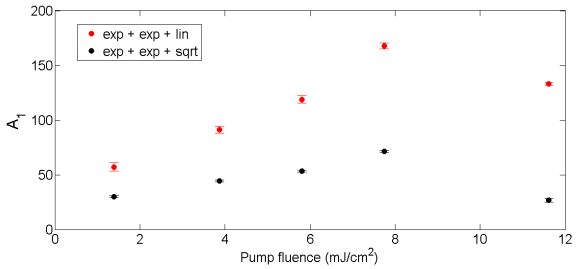

(a) A1

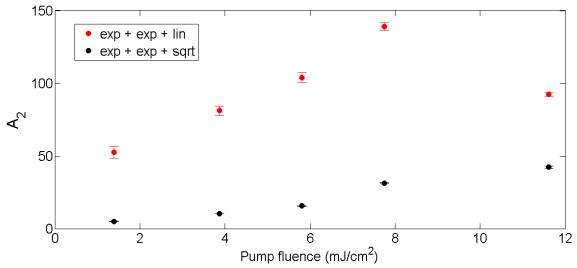

(b) A2

Figure 3.11: A parameters obtained fitting with 3.20 and 3.19.

Let's now focus on the parameters A_1 and A_2: they are proportional to the maximum increase in electron temperature and to the final rise in the temperature of the three subsystems, respectively. For this reason they should increase linearly with the absorbed power, within the approximation made in section 3.2.1.
Figure 3.10 and 3.11 show that this is true for the fitting results obtained with all the different functions.
As regards to the A parameters obtained with the two exponential functions 3.16, the confidence intervals are huge. This can be due to the fact that what determines the shape of this function is only the difference between A_1 and A_2 and the time constants. These two parameters may not be independent and the system is oversampled. This is the reason why they are plotted without error bars in 3.10 a) and b), where we can see that the linear relationship between A parameters and excitation power is satisfied.

Fitting different time ranges

It is interesting to check if the fitting parameters change, when one changes the time range of the data.
In figure 3.12, results obtained with data up to 30 ps, 18 ps, 10 ps, fitted with the

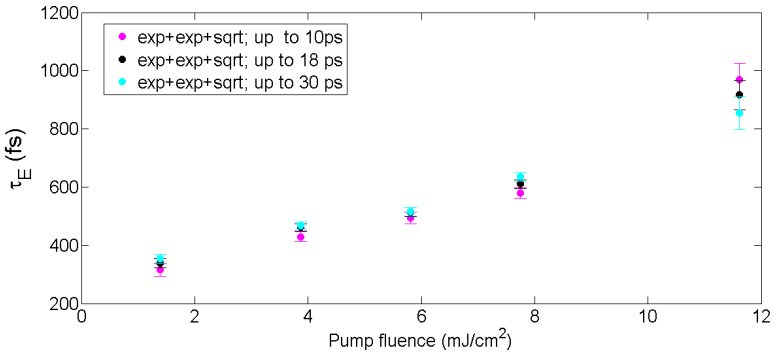

(a) Remagnetization time

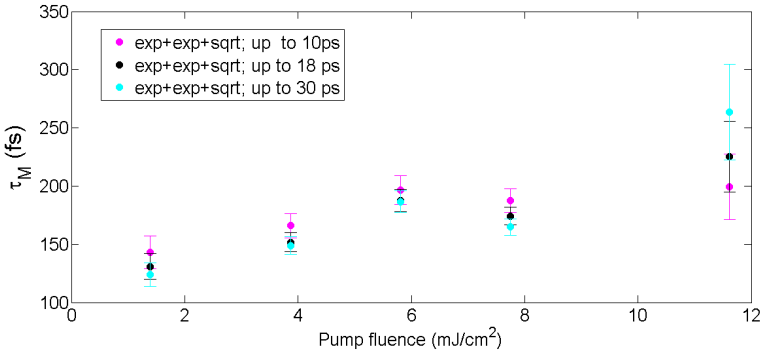

(b) Demagnetization time

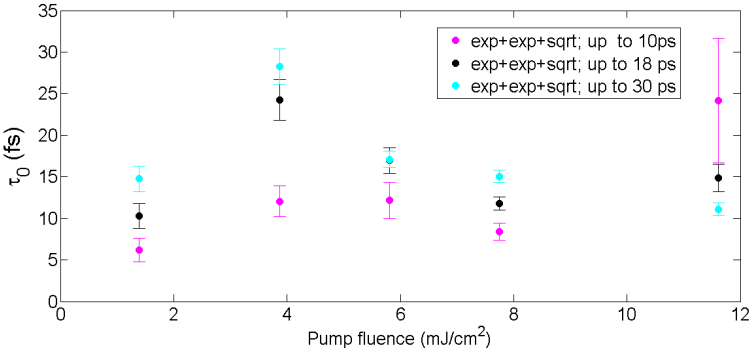

(c) Third time constant

Figure 3.12: Time constants as parameters in the fitting function 3.19. Data extending over different time range are analysed as reported in the legend.

two exponentials and a square root function ("exp + exp + sqrt") are compared. Alternatively, in figure 3.13 the same comparison is done using the two exponentials and a linear function as the later times term ("exp + exp + lin"). For both functions

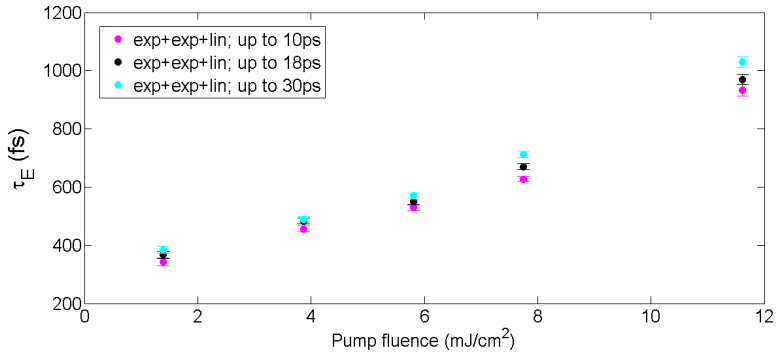

(a) Remagnetization time

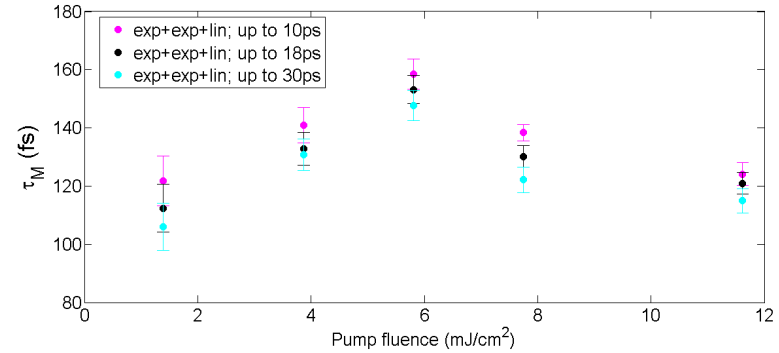

(b) Demagnetization time

Figure 3.13: Time constants as parameters in the fitting function 3.20 Data extending over different time range are analysed as reported in the legend.

we can observe that the demagnetization time decreases for a larger time range, while the remagnetization time increases over a longer time range.

Concerning τ_M it should be emphasized that for the two exponentials and a square root ("exp + exp + sqrt", figure 3.12(b)) changes are within the errorbars concerning the 30ps and 18ps data set (except that for the highest fluence), while they are larger for 10ps data set.

This means that for these fluences and this geometry 18 ps are sufficient to fit later times with the square root term.

In figure 3.12(c) the third time constant used in equation 3.19 is shown. Again, the

difference between the 10 ps data set and the other two (18 ps and 30 ps) is the most significant. For the 10 ps set, the errorbar at high fluence is huge, this range is not enough to fit later times at higher fluences.

3.2.5 Thin sample on insulator

The derivation of the spin temperature, used to fit demagnetization curves, needs some approximation. One of them excludes heat diffusion outside the probed region; it thus requires to have thin samples grown on insulators.
This is not the case of the sample analysed previously, which is 24nm thick, while the probe penetration depth is just 10nm.
To check if this plays any role in the above discussed results, the same analysis has been done for a sample which fulfils these requirements: a 8.8nm thick Co/Pt multilayer grown on the insulating Si_3N_4. The layers that compose this sample are [Cr(2 nm)/Pt(3 nm)/[Co(0.4 nm)/Pt(0.7 nm)]$_{\times 8}$/Pt(1.3 nm)].

In figure 3.14, remagnetization time (a) and demagnetization time (b) as obtained from fitting data from thin Co/Pt multilayer with different fitting functions are shown. Regarding remagnetization time, results obtained with all the different models are consistent. This is quite an improvement compared to results using thicker sample.
Unfortunately, differences in demagnetization times are not lower than when using thicker sample.
The incongruity in the models is thus not fully solved using a thin sample, where there is no transversal heat diffusion. However, things are better for remagnetization times. This is not unexpected, since it is in the recovery at later times where heat diffusion plays a role.

3.3 Slowing down of demagnetization process at high fluence

Looking at time constants for both of samples studied in this chapter, it can be seen that the whole process slows down with increasing excitation fluence, no matter which function is used.
Both in the thick (3.5a) and the thin sample (3.14a), remagnetization time is proportional to the excitation fluence.
For demagnetization time constants, the behaviour with respect to the excitation is not very clear. A slowing down is visible only at low fluences.

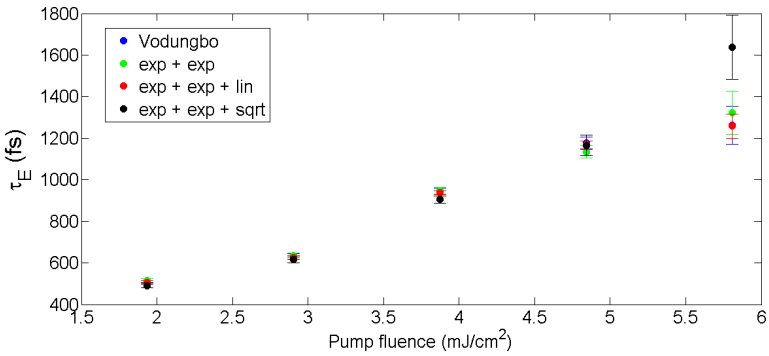

(a) Remagnetization time

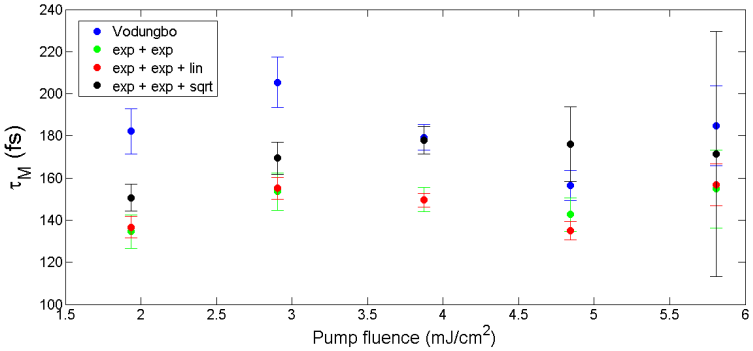

(b) Demagnetization time

Figure 3.14: Time constants as a function of fluence as obtained from measurement on 8.8nm Co/Pt ML at different fluences. The different results are due to different fitting functions used, as reported in the legend.

This behaviour has already been predicted and discussed in literature, by different groups and theories.

For example, figure 3.15 shows the results of a simulation performed by Koopmans et al. [6], using their Microscopic Three Temperature model (M3TM) discussed in Chapter 1. As already explained in the first chapter, within this model the magnetization $m(t)$ is described by the following differential equation [6]

$$\frac{dm(t)}{dt} = Rm(t)\frac{T_l}{T_C}\left(1 - m(t)coth(\frac{mT_C}{T_e})\right) \tag{3.22}$$

It depends thus on the electron T_e and lattice T_l temperature, which depend themselves on the excitation fluence. It should be reminded that T_C is the Curie temperature,

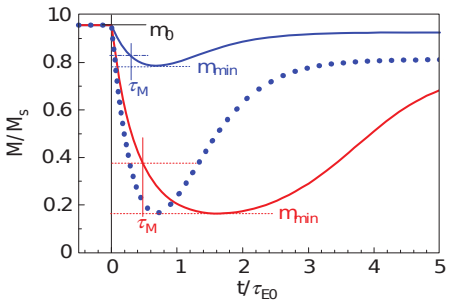

Figure 3.15: Theoretical demagnetization curve obtained with Koopman et al.'s theory [6] for a material with a large spin-flip rate. Blue line for low fluence, red line high fluence. The blue dotted line represents the scaled low fluence curve, that can be compared with the high fluence curve.

$m = \frac{M_{eq}(T)}{M_{eq}(0)}$ and $R \propto a_{sf} \frac{T_C^2}{\mu_{at}}$, being a_{sf} the spin flip scattering probability and μ_{at} the atomic magnetic moment. Solving the three equations 3.9, 3.10 and 3.22, with different initial electron temperature, gives a hint to what is happening at different fluences.
This is reported in the curves in figure 3.15. It can be seen that for high fluence (red line) the demagnetization is stronger and slower than at low fluence (blue line, the dotted one is scaled to compare with the high fluence), also the remagnetization is slower. The behaviour of demagnetization time is discussed in Chapter 5 with experimental data and solving the M3TM coupled equations.
With regard to remagnetization, this slowing down is explained in [16] and it is referred to the existence of a "memory" in the magnetic system: the more magnetic disorder is caused in the sample, the more time it needs to recover order.
For this reason the recovery of the magnetization could be slower than recovery of internal energy. For instance, if the sample were fully demagnetized by the laser pulse it would lose all of its magnetic order and magnetic "memory". After this full demagnetization, small regions of magnetic order of a lengthscale of the correlation length would grow, each of them being randomly aligned. The recovery would then be slower than having some "memory" of the initial state.
All data presented in this thesis confirm a linear relationship between remagnetization time and pump fluence, for the pump fluence range used here. This is very useful because it can be a further measure for the excitation, in addition to the pump fluence. This will be necessary for the samples analysed in the next chapter.
In general we can say that, the pump power is measured, the beam spot is known, the fluence can thus be calculated.

This value of fluence may not be exact. It depends on the position of the sample with respect to the microscope objective. As already reported in Chapter 2, this is fixed because it coincides with the focus position of the camera that is used to image the sample, with an uncertainty that corresponds to the Rayleigh length of the camera objective.

In figure 3.16 the data taken on the same sample, analyzed with the same function,

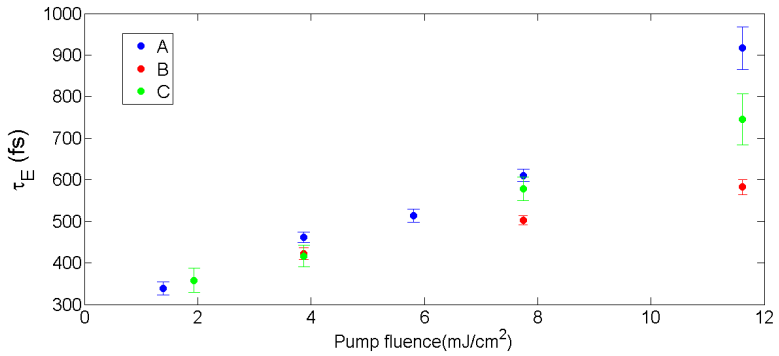

(a) Remagnetization time

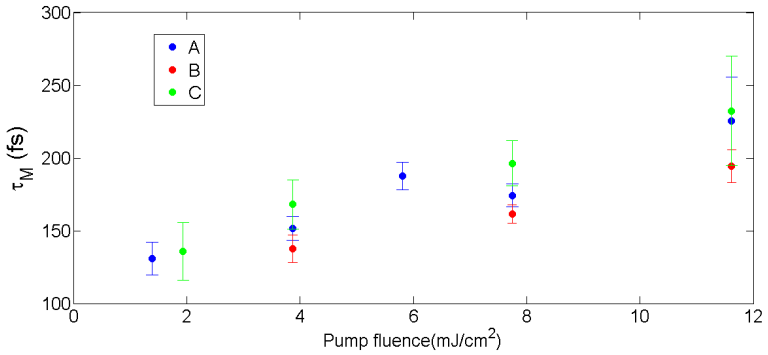

(b) Demagnetization time

Figure 3.16: Time constants as a function of fluence as obtained from measurement on 24nm Co/Pt ML at different fluences. Three different sets of measurement are reported, all of the analyzed with the two exponentials and a square root function 3.19.

but taken in different days are shown. In addition a data set labelled with C is taken without the PEM, but with a lambda quarter plate which allows us to measure the Kerr ellipticity even in this configuration.

The agreement is good for low excitation ranges both for remagnetization and demagnetization time constants, but there are some differences at high fluences. The differences

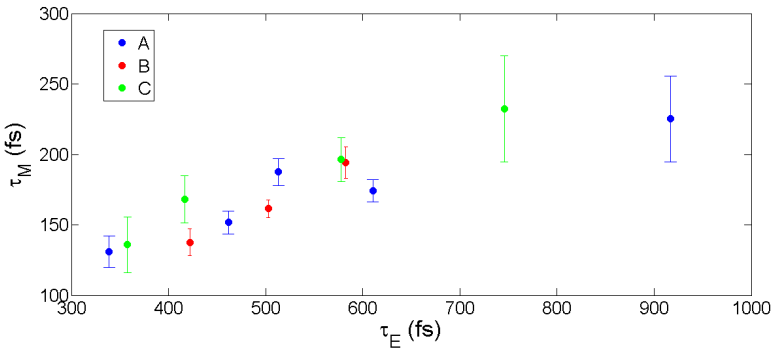

Figure 3.17: Demagnetization time versus remagnetization time as obtained from measurement on 24nm Co/Pt ML at different fluences. Three different sets of measurement are reported, all of the analyzed with the two exponentials and a square root function 3.19.

can represent the error in our measurements, which is expected to be larger at high fluences due to the fact that most of the approximations made in this chapter hold at low fluences. However the pump fluence through the pump power cannot be completely trustworthy as a measurement for excitation, at least not when you want to compare data taken in different days, when you must repeat the alignment procedure.
It must thus be highlighted that the pump fluence has a meaning when looking at data acquired in the same day, because the process of alignment is unique and the position is not changed.
In figure 3.17 demagnetization time is plotted versus remagnetization time, which constitutes the measurement of the excitation. We can see here that now the three sets of measurements are consistent and τ_M is proportional to τ_E at least for low fluences.

3.4 Conclusion

The process of ultrafast de- and re- magnetization is too complicated to be satisfactorily described by a simple analytical function.
Depending on which approximations are chosen, the extracted time constants differ significantly and values for demagnetization time have a difference up to 50fs.
This means that these time constants only make sense with a corresponding model. If the models are different, so will the time constants.
Whatever function is chosen to fit demagnetization curves, if different measurements on different samples or taken at different fluences must be compared, it is very important to use the same function and to analyse data taken in the same temporal range.

In the rest of this thesis, demagnetization curves will be fitted using the two exponentials and a square root function, 3.19, ("exp + exp + sqrt") for measurements taken up to 18 ps. It was indeed shown that results would not change adding later times and this ensures us that with data up to 18 ps we are already appropriately describing the last part of the curve, at least for this sample geometry, at the used fluences.

This analysis also showed that, no matter which function one uses, the demagnetization times depend on the fluence; at high excitation fluence demagnetization dynamics slows down.
This fact suggests that it is unreliable comparing demagnetization time for different samples, if they are not taken at the same pump fluence. It makes sense to perform for every sample a fluence dependence measurement.
Also the recovery of the magnetization slows down with fluence, it can be seen that it is linear and can thus be taken as a measure of excitation. At least for the two types of samples analysed in this chapter, which are the bases for all the samples discussed in this thesis.

Chapter 4

Gold grating on Co/Pt multilayer: the role of lateral diffusion

4.1 Motivation

After the publication of the first paper about superdiffusion [8], experimental efforts focusing on the role of spin transport have been undertaken. [13] [36]
Pfau et al. [9] and Vodungbo et al. [10] led to experimental evidence of the superdiffusive spin transport between domains, which was investigated with Free Electron Laser (FEL) pulses. The use of X-ray allows a sub-100 nm spatial resolution.

Regarding technology application, a lot of efforts and attention is focused on ultrafast demagnetization and all-optical switching, which can help magnetic recording with the goal of "faster and smaller". In attempting to make the area of one bit smaller, enhancement and localization of the light field become fundamentally important.
Even in the conventional magnetic recording technology, where a magnetic field is used to write, localization of the light field can have a fundamental role in increasing the density data storage. A promising technique is the heat assisted magnetic recording (HAMR) [51] which uses a laser source to heat the material and decrease the coercive field below the available writing field. Within this technology, localization of the light field makes the bit area smaller and thus the density data storage increases.
Localization of light in far field is unfortunately limited to the wavelength of visible radiation (hundreds of nm), for this reason phenomena of enhancement and localization of the field through gold structures that sustain localized plasmonic excitation or

interfaces effects are studied with increasing interest.

4.2 Samples

The samples studied and analysed in this chapter are based on Co/Pt multilayers (ML). Additional gold gratings with different space width were nano-structured on the sample surface.
For this measurement a multilayer based on Co/Pt formed by the following layers [Ta(2 nm)/Pt(3 nm) /[Co(0.8 nm)/Pt(1.4 nm)]$_{\times 11}$/Pt(0.6 nm)] was deposited via ion assisted DC magnetron sputtering on a silicon wafer.
Once the magnetic material was grown on the substrate, the sample was ready for the lift off technique which was performed in Lund, Sweden. This technique allows one to deposit structures of a target material (gold in the present case) on the surface of a substrate (here the Co/Pt ML).
First, a sacrificial material is deposited on the substrate and patterned through etching. Then deposition of the target material takes place, which attaches to the substrate only where the sacrificial material was etched. Finally, the sacrificial material is washed out, together with the target material on top of it. At this point you have a patterned target material deposited on the substrate. In our case this is in the form of gold stripes.
In figure 4.1 electronic microscope images of these samples are shown.
In the A structure, figure 4.1 (a) and (b), the grating has a spacing of 200 nm, and gold stripes are 200 nm width. While in the B structure, figure 4.1(c) and (d), the spacing is 120nm and the gold stripes 240 nm width.

Gold has a much higher reflectivity (97%) than the magnetic layer (70%), the absorbed power is thus far less in the region with the gold stripes, than what is absorbed by the magnetic layer (3% compared to 30%). In addition, gold stripes are 30nm thick, thus thicker than the penetration depth of the pump and probe signal; the light absorbed in this region is mainly absorbed by gold. Before presenting results and the discussion about this sample, the paper by Eschenlohr et al. in reference [35] should be mentioned. Here they have a Ni film covered with 30 nm of gold and study its ultrafast demagnetization after optical excitation with X-ray circular dichroism. This allows them to measure the magnetization of the buried structure with an element specificity. After the excitation of the gold layer a demagnetization is detected in the Ni layer. It is indeed excited by "hot" electrons of the gold, which through scattering events generate hot electrons in the magnetic layer. This is not expect to give a significant effect in this sample because they had to pump very strongly (at least 23mJ cm^{-2}) to reach such

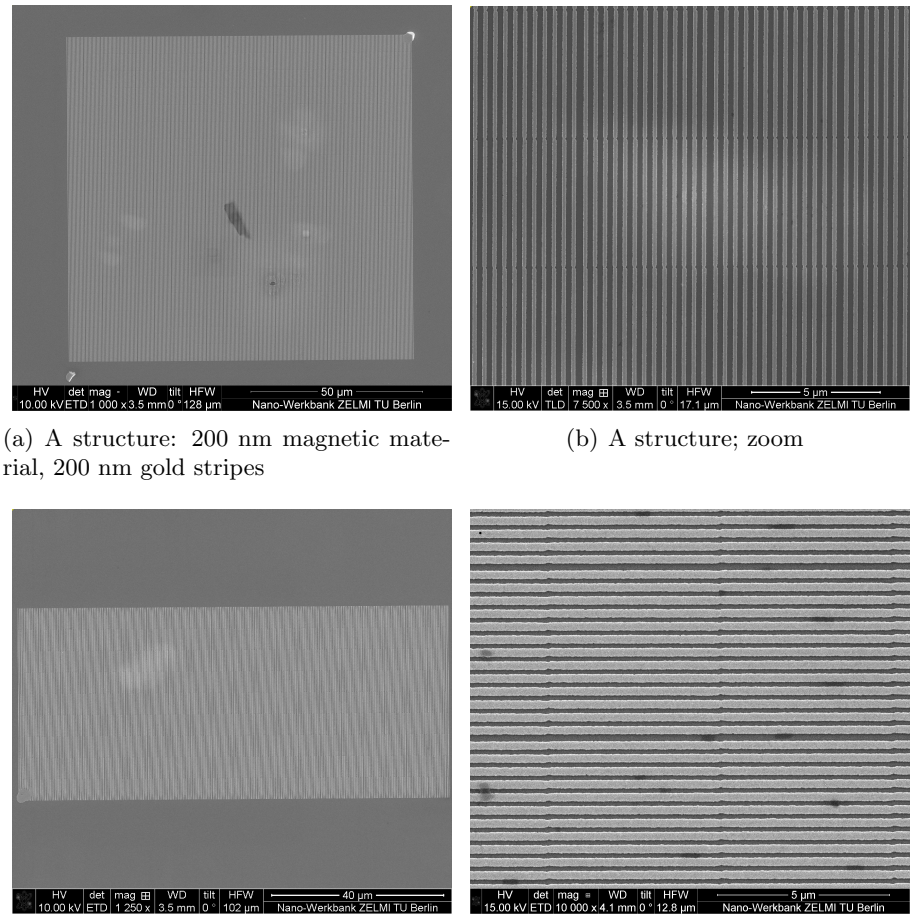

(a) A structure: 200 nm magnetic material, 200 nm gold stripes

(b) A structure; zoom

(c) B structure: 120 nm magnetic material, 240 nm gold stripes

(d) B structure; zoom

Figure 4.1: Electron microscope images of the samples here studied: the bright areas depict the gold stripes, the dark areas the magnetic layer.

a result, while in the present experiment these fluences are not reached in most of the data points.

For all these reasons, when one excites and probe a gold grating, a magnetic signal is produced only by the magnetic layer between the gold stripes.

This makes these samples useful to test the superdiffusive spin transport theory, which was discussed in Chapter 1.

In these samples, majority electrons have an additional channel to escape from the probe beam, i.e. under the gold stripes. Thus, if superdiffusion has a role the demagnetization should be faster and the more efficient.

It is here possible to test the role of lateral diffusion, which usually does not play any role in magneto optical experiment. Indeed, if the spot used to excite has dimensions in the μm range ($\sim$6 μm diameter in our case) there is not a lateral gradient of "hot" electrons on the length scale of interest, reminding that the electrons velocity is about 1nm/fs. The presence of gold stripes provides for the lateral gradient, since due to gold absorption the underlying magnetic material is not excited.
Lateral diffusion has been previously studied between domains [9] [10] exploiting the spacial resolution of X-ray provided by a FEL.

4.3 Excitation profiles of the gold structured Co/Pt ML

The intensity profile of incident light on a gold structure is altered by the gold stripes. In addition the anisotropy of the structure makes the response dependent on the light polarization.
A commercial-grade simulator based on the finite-difference time-domain method was used to perform the calculations of the electric field distribution in the gold structures. This software is a Maxwell equation solver based on the finite-difference-time-domain method (FDTD method), specifically developed for photonic applications. This numerical analysis method solves the Maxwell equations, in their partial derivative form, giving the evolution of the field with respect to time. The partial derivative are first approximate with a finite difference, then are solved with the *leapfrog* method. Within this method, the electric field vector components are solved in a certain space volume, for a certain instant of time. For the following instant of time (the time and the space domain are discretized to solve equations), the components of the magnetic field are characterized. This procedure is repeated until the steady state is fully solved. Lumerical program was run on the two different structures studied in this thesis and for each structure the electric field obtained impinging on both the sample with S and P polarization is calculated.
The P polarization is perpendicular to the stripe direction; a bigger field intensity enhancement is expected for this polarization, since it interacts with the interfaces in the samples.
Instead of simulating the Co/Pt ML, just a single layer of Co was modelled since the two material have similar optical properties.
In figure 4.2 the solution obtained for the intensity profile of the pump light at a depth of 6 nm is shown. The squared electric field is plotted, normalized to the value that would be obtained in the flat surface at a depth of 6 nm in the cobalt layer. For this

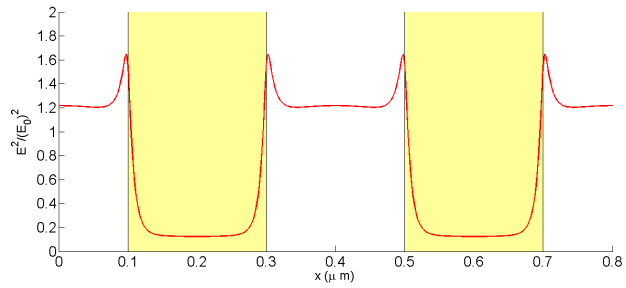

(a) A structure; P polarization

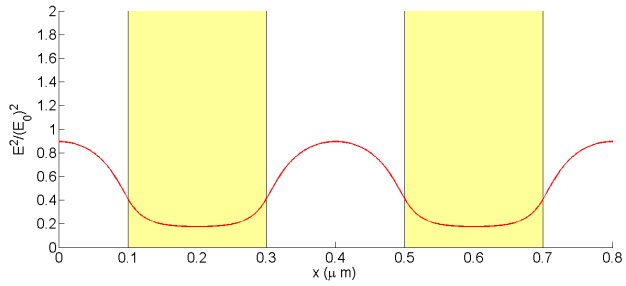

(b) A structure; S polarization

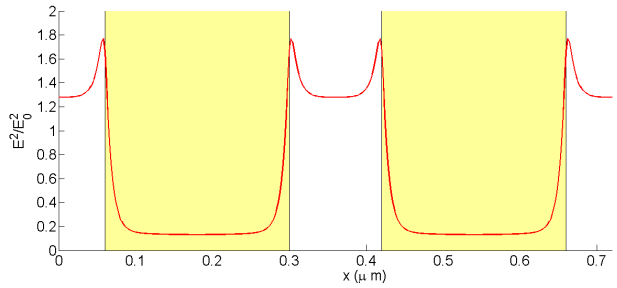

(c) B structure; P polarization

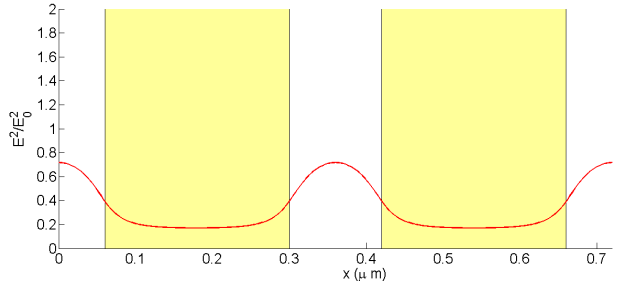

(d) B structure; S polarization

Figure 4.2: Field intensity profile for 800 nm impinging light on gold gratings. The yellow rectangles represent the position of a gold stripe. The value of the field is taken at a depth of 6 nm in the Co layer. For each space coordinate the field value is normalized to the value it would have in a flat surface with no structures.

reason the value can be interpreted as the enhancement or reduction of the field in the gold gratings.
As expected, the intensity using the P polarization is higher than the S polarization. Furthermore, a reduction of the field is observed with the S polarization.
It should be remembered that this light field is used to pump the magnetic layer, this means that we provide a higher excitation when we pump with a P polarized pump beam than with a S polarized one. We should thus see some difference in the remagnetization time, which depends on the excitation as explained in the previous chapter.

4.4 Results

In this section experimental results from this sample are presented. Demagnetization curves are measured using the experimental set up described in Chapter 2, exciting the magnetic layer with no structure(figure 4.3) and with the two different gold structures (figure 4.4), varying the polarization of the pump beam.

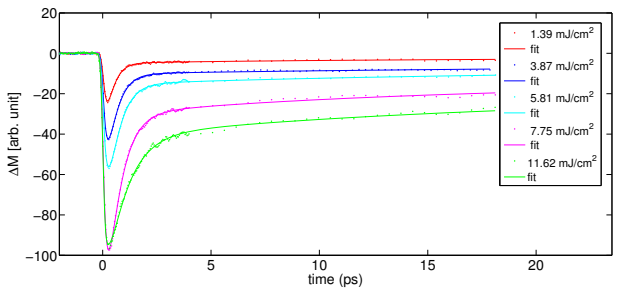

Figure 4.3: Demagnetization curves measured in the flat surface at different pump fluences as shown in the legend.

As pointed out in chapter 3 if we want to compare the time constants of different samples, different fluences and different pump and detection conditions, we must be sure that the same fitting function is used and that data taken in the same time range are analyzed. For this reason demagnetization curves taken from this sample are analyzed with the two exponentials and a square root function, keeping data up to 18 ps.
In figure 4.5 remagnetization and demagnetization time constants obtained measuring demagnetization curves exciting the flat surface are shown.
In figure 4.6 and 4.7 the results obtained for the two gold structures for both the polarization states (as in the legend) are reported.
It can be seen that the time constants obtained from the curves on the gold structures

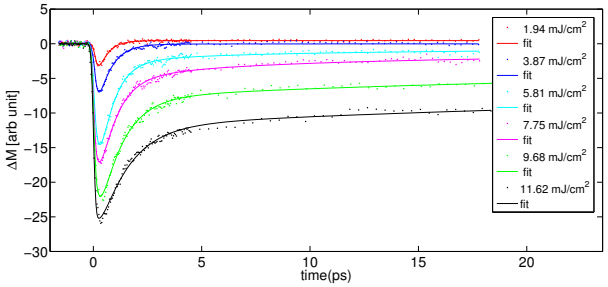

(a) A structure; P polarization

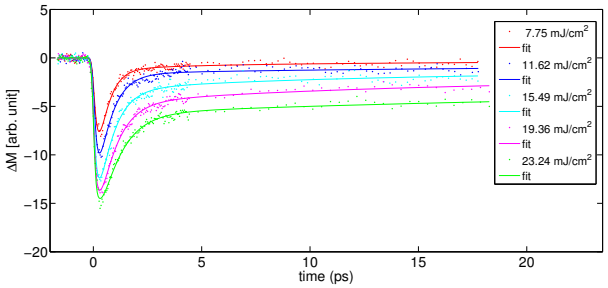

(b) A structure; S polarization

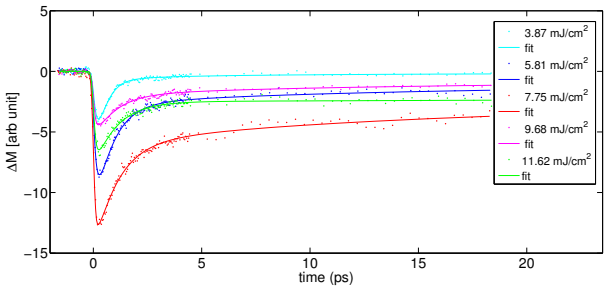

(c) B structure; P polarization

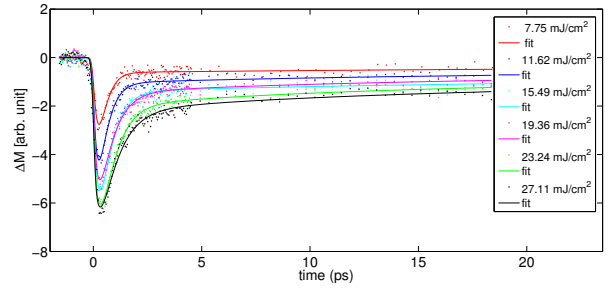

(d) B structure; S polarization

Figure 4.4: Demagnetization curves measured in the A structure (200nm spacing) for P (a) and S (b) polarization and in B structure (120 nm spacing) for P (c) and S (d) polarization at different pump fluences as shown in the legend.

have larger errorbars than the ones obtained from the flat surface. The curves from the gold gratings are more noisy, because the magnetic area which gives the signal is reduced. It can be seen, indeed, that the quality of the data from the B structure is worse than A structure, the former having more gold than magnetic material on the surface.
Concerning remagnetization times (figures (b) in 4.6 (A) and 4.7(B)), it is already possible to distinguish the two ranges of excitation corresponding to the two states of polarization; this will be further discussed in the next section.

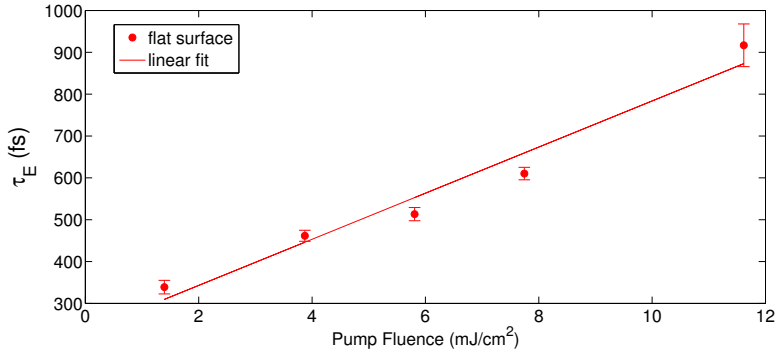

(a) Remagnetization time

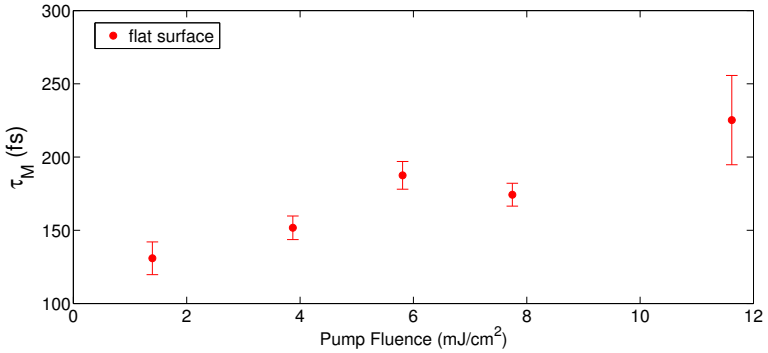

(b) Demagnetization time

Figure 4.5: Time constants as a function of fluence obtained fitting the demagnetization curves measured on the flat surface of a 24.2 nm Co/Pt ML. In (a) the best linear fit is shown.

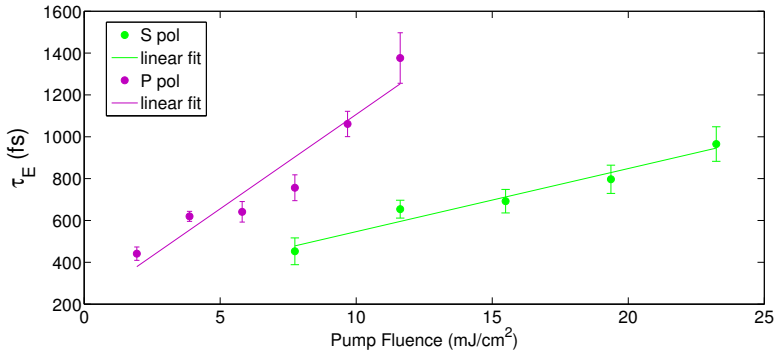

(a) Remagnetization time

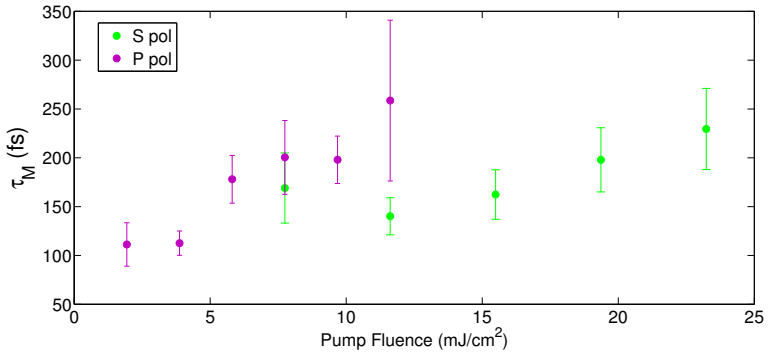

(b) Demagnetization time

Figure 4.6: Time constants as a function of fluence obtained fitting the demagnetization curves measured on the gold grating A (200nm space width) deposited on a 24.2 nm Co/Pt ML. In (a) the best linear fit is shown.

4.5 Linear relationship between remagnetization time and pump fluence

Figure 4.5(a), 4.6(a) and 4.7(a) show the best fit for remagnetization time vs pump fluence according to a straight line. In the following table the fit parameters are reported, with p1 being the slope of the straight line and p2 the y-intercept.

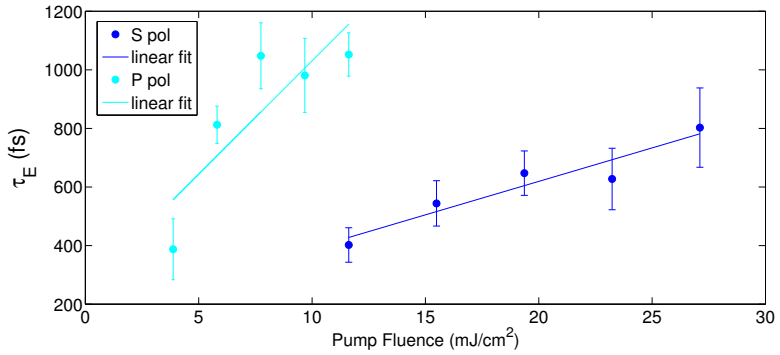

(a) Remagnetization time

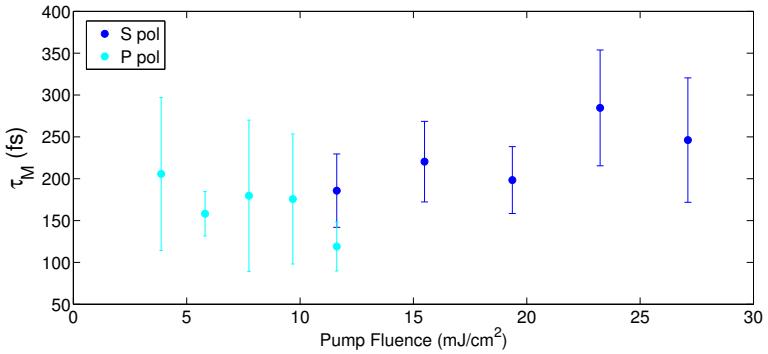

(b) Demagnetization time

Figure 4.7: Time constants as a function of fluence obtained fitting the demagnetization curves measured on the gold grating B (120nm space width) deposited on a 24.2 nm Co/Pt ML. In (a) the best linear fit is shown.

	p1 ($\frac{fs}{mJ/cm^2}$)	p2 (fs)
Flat surface	213 ± 29	233 ± 52
A structure P polarization	349 ± 62	205 ± 122
A structure S polarization	117 ± 17	245 ± 71
B structure P polarization	300 ± 129	257 ± 273
B structure S polarization	88 ± 19	162 ± 101

The linear relationship is not based on a physical model, but just to the observation of experimental results.

Such a linear behaviour has already been discussed in the previous chapter, as well as the possibility to use remagnetization time constants to calibrate excitation density.

As I previously showed, the excitation provided by the same fluence in the structure

and in the flat surface is different, it also depends on whether you excite with S or P polarized light. The pump fluence obtained measuring the pump power of the 800 nm beam cannot be a measure of the excitation acting on different samples.
In addition, the maximum demagnetization value cannot be measured with the experimental set up used in this thesis. Even if the value measured by the optical detector at the minimum of demagnetization curve is itself proportional to the maximum demagnetization value, this does not help when one wants to compare curves taken from the film and the structures. Light which experiences a Kerr rotation and gives a signal is the fraction impinging on the magnetic layer, which in case of incidence on gold structures is not the whole incident light as in the flat surface. Therefore less " Kerr rotated" light is collected by the detector.
For all these reasons, the remagnetization time constant has been chosen as a measure of excitation in the samples.
It is now possible to verify if the enhancement or reduction of the field in the structure is reflected in the excitation.
From Lumerical simulation, the value of the field intensity in the structure relative to the flat surface is given and shown in figure 4.2. In the third column of table 4.1 the mean intensity evaluated in the spacing between the gold gratings is reported for each configuration. To infer the value of the excitation compared to the flat surface, the slope of the remagnetization time versus pump fluence in the structure (called p1) for a given polarization is compared to the same slope in the flat surface. This is done in the second column of table 4.1.

	excitation	field intensity $\frac{E^2}{E_0^2}$
A structure P polarization	$\frac{p1_{A,Ppol}}{p1_{film}} = 1.6 \pm 0.5$	1.26
A structure S polarization	$\frac{p1_{A,Spol}}{p1_{film}} = 0.6 \pm 0.2$	0.74
B structure P polarization	$\frac{p1_{B,Ppol}}{p1_{film}} = 1.4 \pm 0.8$	1.38
B structure S polarization	$\frac{p1_{B,Spol}}{p1_{film}} = 0.4 \pm 0.2$	0.6

Table 4.1: In the second column of the table the ratio between the slope of τ_E vs pump fluence in a structure for a given polarization and the same slope for flat surface is reported as given from the linear fit. These values must be compared with the third column: ratio between mean field intensity in the spacing between gold stripes and field intensity in flat surface. These values are obtained from Lumerical simulation and the intensity profile has been previously shown in figure 4.2.

Within the experimental errors, values in the two columns are consistent.
An enhancement of the excitation can thus be reached in gold grating, which has an effect in magnetization reduction and recovery.

4.6 Demagnetization time

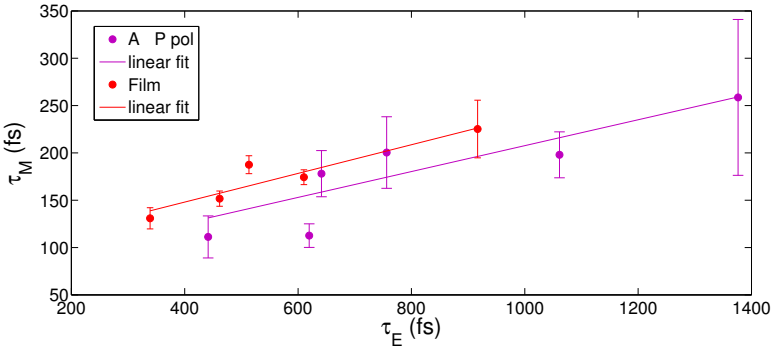

(a) P polarization

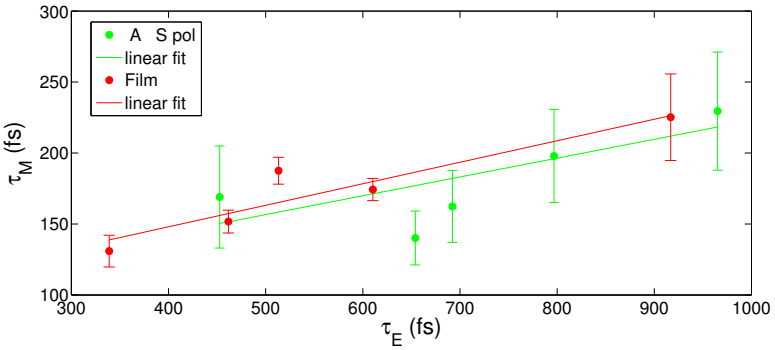

(b) S polarization

Figure 4.8: Demagnetization time τ_M as a function of remagnetization time τ_E. Comparison between A structure for P (a) and S (b) polarization and the film.

At this point a comparison between demagnetization time in the film and in the structure must be done. Therefore τ_M is plotted with respect to remagnetization time τ_E, which is an unambiguous measure of excitation.
In figure 4.8 demagnetization time in the A structure (200nm space width) is directly compared to the results from the film. From this plot, demagnetization time is propor-

tional to remagnetization time for both configurations. A linear fit is then performed as shown in the figures. This is useful to compare results from the A structure and from the film. As far as the P polarization (figure 4.8(a)), a difference is visible, demagnetization in the structure is faster than in the film. We interpret this as an indication that superdiffusive spin transport contributes to the process of ultrafast demagnetization. For S polarization (figure 4.8(b)) this difference is not as evident as in P. This can be due to the field distribution as shown in figure 4.2. For P polarization the field intensity gradient is very strong and this supports diffusion, whose effects are very visible. On the contrary, for S polarized impinging light, the field intensity has a weak gradient in the spacing between gold stripes and diffusion is less efficient.
In figure 4.9 comparison between the B structure (120nm spacing) and the film is done. Unfortunately, errorbars are too large to deduce a trend.

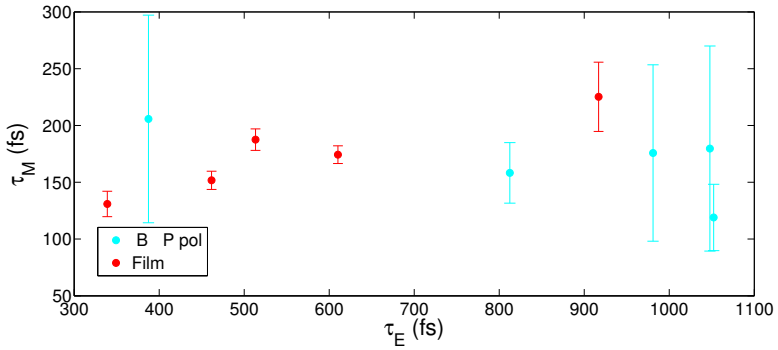

(a) P polarization

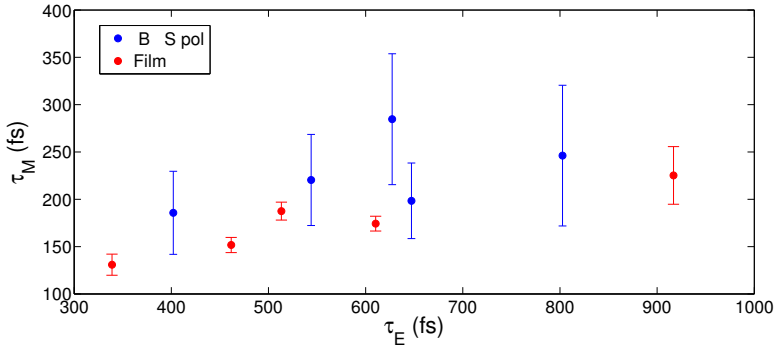

(b) S polarization

Figure 4.9: Demagnetization time τ_M as a function of remagnetization time τ_E. Comparison between B structure for P (a) and S (b) polarization and the film.

At least for A structure, the expected effects of lateral excitation gradient are evident, but weak. This can be due to the large dimension of 200 nm (space width) taken into account, since [8] refers to hot electrons velocity of 1nm/fs.

4.7 Conclusion

One of the ideas which led to the deposition of this sample was the possibility to enhance and localize the field.
Since remagnetization time is a measure of the excitation, it was possible to check the calculated ratio between the field intensity in the structures (for a given polarization) and in the flat surface.
With these length scales, an enhancement of 1.4 is already reached. Performing the Lumerical simulation with other grating dimensions keeping the same pump wavelength, it was found that with a spacing of 10nm the enhancement is of a factor of 2.5, as reported in figure 4.10.

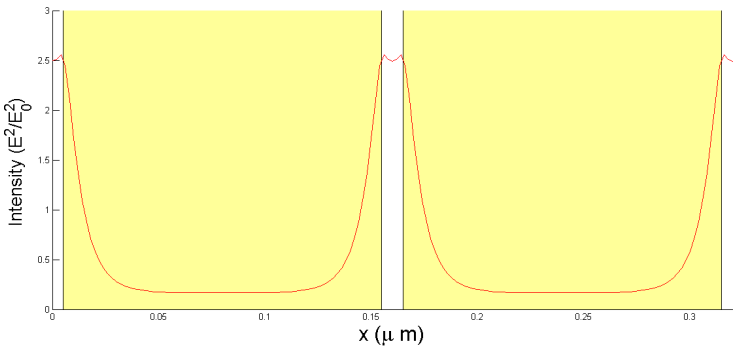

Figure 4.10: Pump intensity profile for a sample with the same composition of the one here studied but with a spacing of 10nm.

The 10 nm spacing can be obtained with the lift off technique, but also by etching the surface with focused ions.
Unfortunately, with such a narrow spacing and such few magnetic surface, demagnetization curves would be more noisy than what we have and it could be difficult to perform magneto-optic measurement.
As concerns the test of superdiffusive theory, we have found indications of a faster demagnetization in the A structure for P polarized pump beam. We propose to explain this difference by superdiffusive spin transport from the optically excited "hot" temper-

ature regions into the unexcited areas "cold" regions. However we have to concede that normal diffusion effects may also alter the dynamics for this sample geometry. This effect was not evident for the S polarization and for the B structure.
It could be a solution to use a different metal for the grating. Indeed it has been proven that in such a thin gold layer the electron transport is purely ballistic [52] and electrons have a velocity of 1 nm fs^{-1}. After the pump excitation, it took 30 fs for hot electrons to be uniformly distributed in the gold stripes, since they are 30 nm thick, and the effect discussed in ref. [35] may play a role.
A different material, e.g. aluminium, with a shorter penetration depth, could prevent this effect of additional demagnetization channel and thus only the optical excitation would provide demagnetization.

Chapter 5

Thin Co/Pt multilayers grown on different substrates: the role of diffusion

5.1 Motivation

In the previous chapter the lateral diffusion in magnetic ML was analysed by nanostructuring a gold grating on to the surface. In this chapter the influence of the transversal spin diffusion and transversal heat diffusion in ultrafast demagnetization processes are discussed for thin samples, i.e. with a thickness comparable to the laser penetration depth.

The finite penetration depth of the laser radiation leads to a transversal gradient of excited electrons. The penetration depth of optical wavelengths in the material is on the order of 10 nm, hence it lies on the lengthscales of superdiffusion (Chapter 1).

For the transversal gradient, the chosen substrate has an important role, both for heat diffusion and for spin superdiffusion. Regarding superdiffusion, the difference in ultrafast demagnetization for magnetic films grown on an insulator or a conductor was pointed out in Chapter 1. The insulating substrate cannot conduct a spin polarized current, the conducting substrate can. Therefore the latter is expected to provide for a stronger demagnetization.

According to M3TM, the demagnetization rate depends on electron and lattice temperatures, which are not homogeneous in the depth of the sample. The role of the substrate is studied in [25]. Here a larger maximum demagnetization value in the sample deposited on an insulating substrate is predicted, since electronic heat diffusion

in the perpendicular direction is weaker than for the conducting substrate. A slower demagnetization in the sample on insulator than in the sample on conductor is also predicted. Both of this effect are more pronounced at high fluences.

5.2 Samples

The samples studied here are again based on Co/Pt multilayers, which are grown on different substrates, conducting or insulating.
Two types of ML are made:

- [Cr(2 nm)/Pt(3 nm)/[Co(0.4 nm)/Pt(0.7 nm)]$_{\times 8}$/Pt(1.3 nm)];
- [Cr(2 nm)/Pt(13 nm)/[Co(0.4 nm)/Pt(0.7 nm)]$_{\times 8}$/Pt(1.3 nm)];

The layers are written in the growth order, therefore the top layer is the last one. The magnetic ML is the same [Co(0.4 nm)/Pt(0.7 nm)]$_{\times 8}$ with a total thickness of 8.8 nm, less than the penetration depth of the pump ($\sim$ 13 nm) and the probe beam ($\sim$10 nm). The difference in the two ML is the additional layer of Pt in the second one, 13 nm thick instead of the 3 nm in the first one. These two ML are then grown on Au or silicon nitride (Si_3N_4), which is an insulator.
For clarity, in figure 5.1 a sketch of the samples analysed in this chapter is shown. The different substrates for the magnetic ML are highlighted.

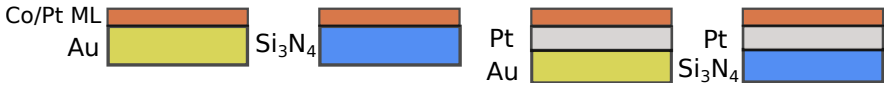

Figure 5.1: In the picture samples analysed in this chapter are schematically depicted. The same Co/Pt ML of thickness 8.8 nm is grown on different substrates. Each colour represents a material, as indicated in the figure.

5.3 Results

Demagnetization curves are acquired for all available samples for different fluences. A demagnetization is detected for all of them and in figure 5.2 the value corresponding to the maximum reduction of magnetization versus the pump fluence is shown. First thing to notice is that demagnetization values for all samples are quite similar, at least at low fluences. Even with such a small difference, a trend can be found. The largest

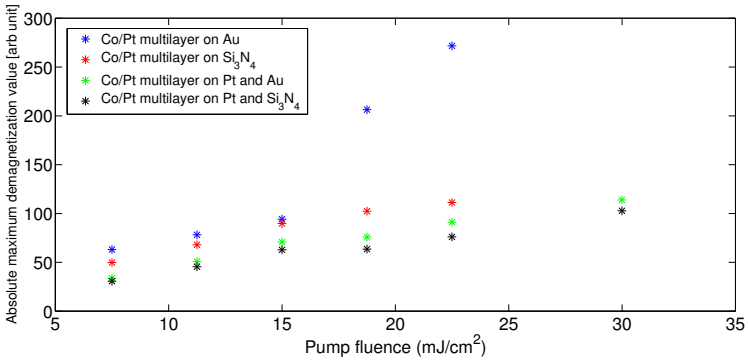

Figure 5.2: Absolute demagnetization amplitude versus pump fluence for the thin Co/Pt ML grown on different substrates, as shown in the legend.

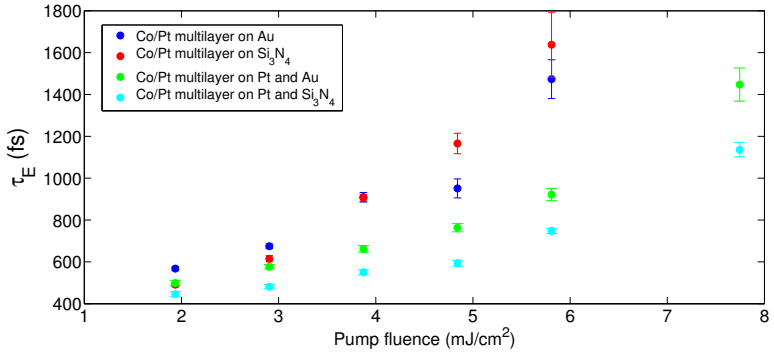

(a) Remagnetization time

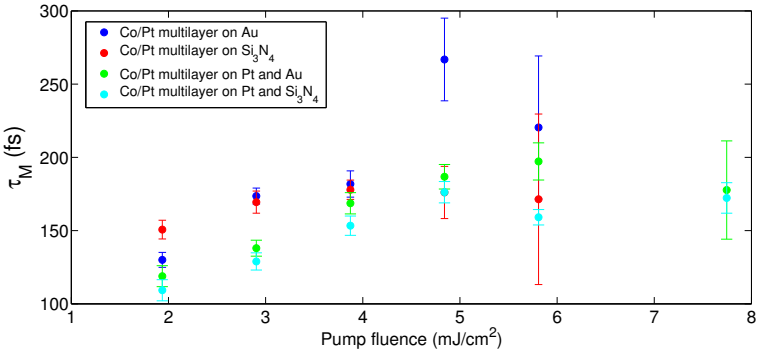

(b) Demagnetization time

Figure 5.3: Time constants obtained fitting demagnetization curves for a 8.8 nm Co/Pt ML grown on different substrates, according to the legend.

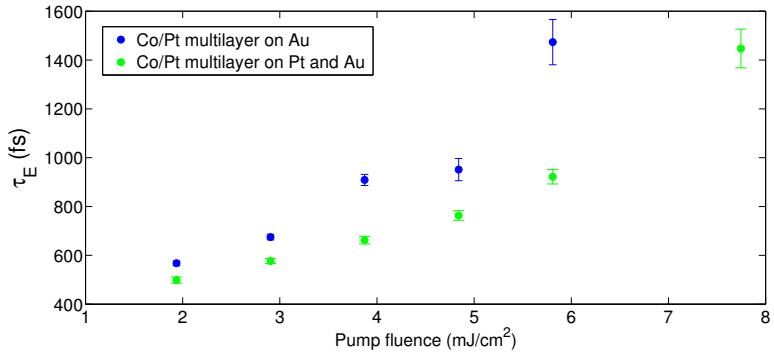

(a) Remagnetization time

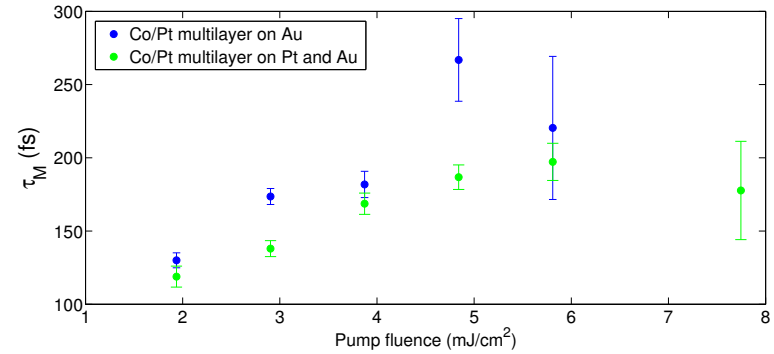

(b) Demagnetization time

Figure 5.4: Time constants obtained from the fitting of demagnetization curves for a 8.8 nm Co/Pt ML grown on Au and on PtAu, according to the legend.

reduction is found in the sample deposited on Au; at high fluence the different is more pronounced. The two samples deposited on the additional Pt layer have very similar demagnetization amplitude, slightly smaller for the one on Si_3N_4. Demagnetization reduction for the magnetic layer grown directly on Si_3N_4 lays at intermediate values between the one on Au and the ones with Pt.

Demagnetization curves are fitted with the two exponentials plus a square root function ("exp + exp + sqrt" as called in chapter 3) in order to obtain τ_M and τ_E, demagnetization and remagnetization time constant respectively.

In figure 5.3 τ_M and τ_E obtained for all samples are shown.

For remagnetization time constants, the more consistent difference is found to be between the sample with and without the additional Pt layer. Hence, in figure 5.4(a) a comparison between the ML grown on Au and on Pt and Au is shown, this makes

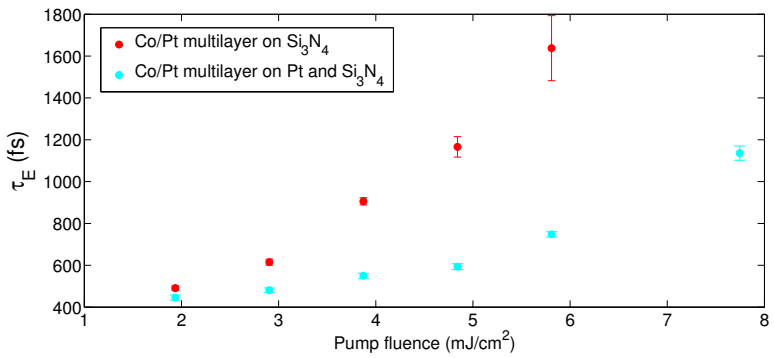

(a) Remagnetization time

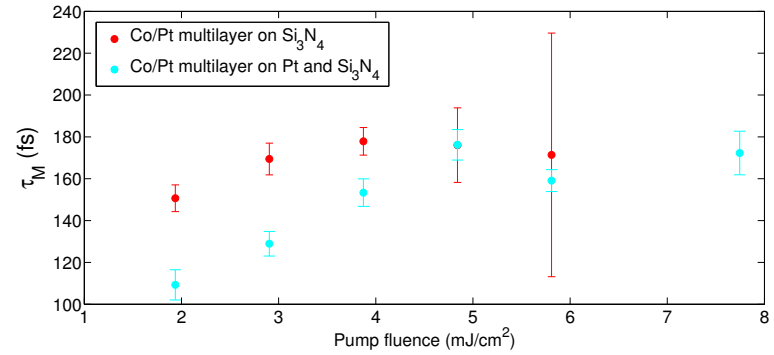

(b) Demagnetization time

Figure 5.5: Time constants obtained from the fitting of demagnetization curves for a 8.8 nm Co/Pt ML grown on Si_3N_4 and on $PtSi_3N_4$, according to the legend.

clear that remagnetization is faster for the sample on Pt and Au layer. Here τ_E is approximately 150 fs smaller than in the sample directly grown on Au, the difference slightly increases with fluence.

Figure 5.5(a) shows that even comparing the remagnetization time for the magnetic ML grown on Si_3N_4 and on Pt and Si_3N_4 the remagnetization is found faster for the sample with the additional Pt layer. In this case the difference increases considerably with fluence.

For demagnetization time constants, the more evident differences are again between samples with and without the Pt layer, at low fluences. Figure 5.4(b) shows a faster demagnetization in the sample grown on Pt and Au than in the samples grown on Au. Figure 5.5(b) compares the sample on Si_3N_4 and on $PtSi_3N_4$ and shows again a faster demagnetization in the latter. For all the samples, τ_M increases with pump fluence up

to a maximum, where it reaches a saturation. This maximum is approximately at 5 $\frac{mJ}{cm^2}$ for all samples.

5.4 Discussion

The first important note to make about the experimental results is that a demagnetization is reached even in the sample on the insulating substrate, where spin diffusion can be neglected. The demagnetization amplitude is very similar for all samples, at least at low fluence. This is a clear indication that superdiffusion alone is not the mechanism underlying ultrafast demagnetization, but other microscopic mechanisms must be taken into account.
In the following the present results are analysed without assuming spin superdiffusion, instead the data is explained according to the M3TM model. In this way the process of equilibrium recovery can also be discussed.
M3TM, as reported in Chapter 1 and 3, is based on coupled differential equations for the time evolution of electron temperature T_e, lattice temperature T_l and magnetization m. These equations can be used to simulate the response of the discussed thin samples on different substrates.
In the derivation of M3TM in Chapter 3, the material is taken to be homogeneous, so is the excitation. Here, due to the finite penetration depth and the different substrate, a non homogeneous heating must be considered. Equations 3.9, 3.10 and 3.22 are now written with the dependence on the transversal dimension z. In addition a term which describes the heat diffusion in the electrons and lattice system is added. Concerning the lateral dimension, the laser spot is too large to give any gradient in the probed area. Hence, the following differential equations follow:

$$C_e(T_e)\frac{dT_e(z,t)}{dt} = \frac{d}{dz}\left(\kappa_e(T_e)\frac{dT_e(z,t)}{dz}\right) - G_{el}(T_e(z,t) - T_l(z,t)) \quad (5.1)$$

$$C_l\frac{dT_l(z,t)}{dt} = \frac{d}{dz}\left(\kappa_l\frac{dT_l(z,t)}{dz}\right) - G_{el}(T_l(z,t) - T_e(z,t)) \quad (5.2)$$

$$\frac{dm(z,t)}{dt} = Rm(z,t)\frac{T_l(z,t)}{T_C}\left(1 - m(z,t)coth\left(\frac{mT_C}{T_e(z,t)}\right)\right) \quad (5.3)$$

Equations 5.1 and 5.2 provide for the electron and lattice thermalization through the coupling constant G_{el}. Heat diffusion in each system is described by the heat conductivity parameters κ_e and κ_l, for electron and lattice respectively.
C_e is the electronic heat capacity, which depends linearly on the electronic temperature:

$C_e(T_e) = \gamma T_e$. C_l is the phononic heat capacity.
As regard parameters found in the magnetization equation 5.3: T_C is the Curie Temperature, which for such a Co/Pt multilayer is approximately 900K [53], while for bulk Co is 1388 K. The m in the argument of the *coth* is the equilibrium magnetization at the ambient temperature T, relative to the value at T=0 K, i.e. $m = \frac{M_{eq}(T)}{M_{eq}(0)}$. The R parameter, already described in chapter 1, will be discussed in the next section.
The different material constants, entering as parameters in equations 5.1, 5.2 and 5.3, are reported in table 5.1. Here heat capacity is expressed as the volumetric heat capacity ($\left[\frac{J}{Km^3}\right]$) and the electron thermal diffusivity α_e is reported instead of the thermal conductivity κ_e. It is defined as $\alpha_e = \frac{\kappa_e}{C_e}$, where again C_e is the volumetric heat capacity.

	Co	Pt	Co(0.4nm)/Pt(0.7nm) ML	Au	Si_3N_4
$\gamma \left[\frac{J}{K^2m^3}\right]$	704	740	727.04	71	0
$G_{el} \left[\frac{W}{m^3K}\right]$	93×10^{16}	25×10^{16}	49.48×10^{16}	2×10^{16}	0
$\alpha_e \left[\frac{m^2}{s}\right]$	2.5×10^{-5}	2.6×10^{-5}	2.56×10^{-5}	12.8×10^{-5}	0
$C_l \left[\frac{J}{Km^3}\right]$	3.73×10^{6}	2.8×10^{6}	3.13×10^{6}	2.5×10^{6}	2.13×10^{6}
$\kappa_l \left[\frac{W}{mK}\right]$	100	73	82.72	318	30

Table 5.1: Constants to be used in the equations 5.1, 5.2 and 5.3 for the elements which compose the samples. The third column refers to the Co/Pt ML: the constants for Co and Pt are weighted with the relative concentration in the multilayer.

These values can be found in [54], regarding the coupling constants, values reported in [55] are used.
Instead of having a source term to describe the laser pulse, an initial electron temperature higher than the temperature of the lattice ($T_l(x,0) = 300K$) is set. In order to consider the non homogeneous pump heating, a temperature profile is given by the pump penetration depth δ: $T_e(x,0) = \Delta T_{e,max} e^{\frac{-x}{\delta}} + 300\text{K}$, where for radiation at 800 nm in Co $\delta = 13.26nm$ [56] (this parameter is very similar for Pt). $\Delta T_{e,max}$ depends on the energy given to the system as reported in equation 3.8: $\Delta T_{e,max} = \sqrt{\frac{2F}{\gamma\delta}}$, where F is the fluence.
A different value must be set for Au. In [52] transient reflectivity measurements in optically excited Au are performed. The response depends on the Au layer thickness

and the mean free path for excited electrons is inferred to be 100 nm. Hence, in this model a penetration depth of 100 nm is used for Au.
These equations and parameters are used to build a Matlab script, which gives the time evolution of electron and lattice temperature distribution as well as magnetization distribution.
To be compared to the measured magnetization, the magnetization distribution is weighted spatially with the probe beam profile $M(z,t) = m(z,t)e^{\frac{-x}{\delta_{probe}}}$, where the penetration depth for 400 nm in Co is $\delta_{probe} = 10.76$ nm [56] and is very similar for Pt. To simulate the magneto-optic response during time $M(t)$, for each instant of time the weighted magnetization distribution is summed along the transversal direction.
It is useful now to comment on the numbers reported in the table, above all about the difference in the electronic properties between Au and the other two metals, Co and Pt.
The Au heat conductivity is larger than the other two. Regarding the coupling constant, it is far smaller in Au than in Co and Pt. This means that electrons diffusing into the Au stay hot for longer times than in the Co/Pt ML. For this reason Au is not expected to favour the equilibrium recovery.

5.4.1 The R parameter

Let's focus on the pre-factor R, which was firstly described in Chapter 1.

$$R = \frac{8a_{sf}G_{el}k_B T_C^2 V_{at}\mu_B}{\mu_{at}E_D^2} \tag{5.4}$$

where μ_{at} is the atomic magnetic moment in units of Bohr magneton μ_B, V_{at} the atomic volume and E_D the Debye energy. a_{sf} is the probability of a spin-flip scattering in a Elliot-Yafet process.
In bulk Co, $T_C = 1388$K and in [6] the value given for R is R=25.3ps^{-1}, where $a_{sf} = 0.15$, as found from fitting.
This value should be calculated now for the Co/PT ML here measured. The material constants different from the bulk Co are T_C and G_{el}. $T_C = 900$K according to [53]. No data for a_{sf} are given in literature so $a_{sf} = 0.15$ is used. The R parameter becomes R=0.98 ps^{-1}.
To start with a direct comparison between calculated and experimental ultrafast magnetization transients is performed in order to make sure the R parameter describes our data appropriately. In figure 5.6(a) the experimental curve is acquired at 2 mJ/cm^2,

which corresponds to $\Delta T_{e,max}$ = 2000K. This is used in the script, together with R=0.98 ps^{-1}. Unfortunately there is no accordance at all with the experimental curve. Calculations are run with increasing values of R until a satisfactory agreement with the experimental curve is obtained. In figure 5.6(b) for R=25 ps^{-1} there is accordance in the decreasing edge, but not in the recovery. To find accordance in the increasing edge, $\Delta T_{e,max}$ must be decreased until $\Delta T_{e,max}$=500 K, as in figure 5.6(c).

The increase in R parameter cannot be ascribed exclusively to a larger a_{sf} value, because, keeping the Co/Pt parameters, R=25ps^{-1} means $a_{sf} > 1$, which is not possible, being a_{sf} a probability. Parameters are not really known for such a ML, in particular G_{el} and for instance T_C has not been measured in this sample. For this reason it is not clear how easily one can transfer Koopmans et al.'s model [6], optimized for bulk Co, to the case of ML.

5.4.2 Distribution of electron temperature, lattice temperature and demagnetization

The electron temperature distribution, obtained implementing the M3TM, gives some interesting results. In figure 5.7 the electron distribution for all samples is reported. The simulation is run on 100 nm total layer thickness and for 10 ps, but here only 50 nm are shown for T_e, since there is not heat diffusion at larger depth, and only the first 4 ps. An initial higher electron temperature is set, weighted by the pump penetration depth. The insulating substrate remains cold, while the conductor acquires a higher temperature. In the case of Au, T_e is large in all the depth due to the high mean free path. Focusing on 5.7(a) and 5.7(b), in a depth between 10 and 20 nm, a difference can be seen for the Au and Pt adjacent to the Co/Pt ML. For the first substrate not only the "hot" electrons are distributed in all the depth, but they remain excited for longer times than in Pt, because of the lower coupling constant G_{el} in Au than in Pt and Co. As regard the ML directly grown on insulator, the equilibrium recovery takes longer than in the other samples, because heat cannot diffuse. This can help in understanding the different behaviour of remagnetization time in the different samples. In figure 5.4(a) and 5.5(a) it is shown that the remagnetization is faster in the sample with the additional Pt than in the sample without it. The Pt substrate favours heat dissipation and makes the recovery process faster. On the contrary, the insulating substrate cannot accept "hot" electrons, which do not diffuse out of the Co/Pt ML. The most interesting result is for the Au substrate: in this sample remagnetization is as slow as in the insulating substrate. Au does not favour equilibrium recovery because

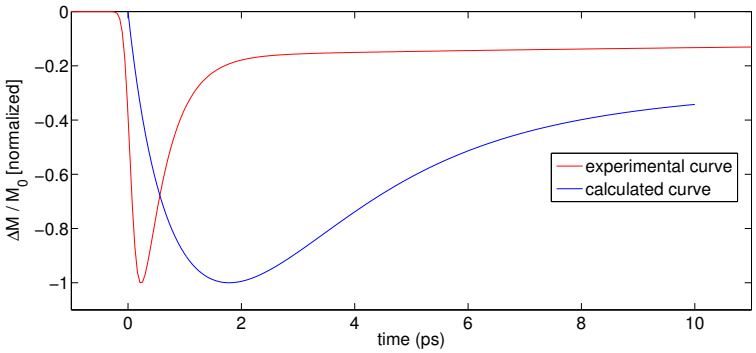

(a) R=0.98 ps^{-1} $\Delta T_{e.max} = 2000K$

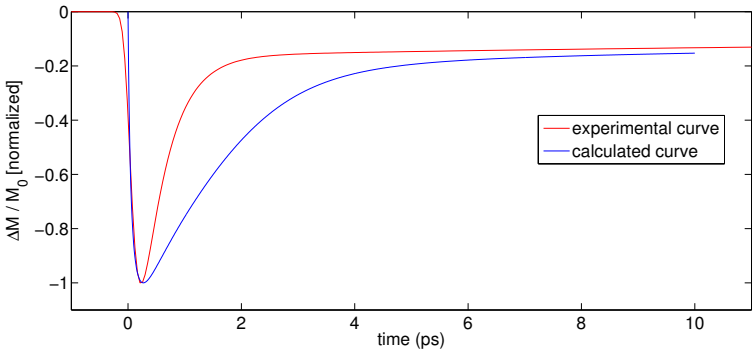

(b) R=25 ps^{-1} $\Delta T_{e.max}$=2000 K

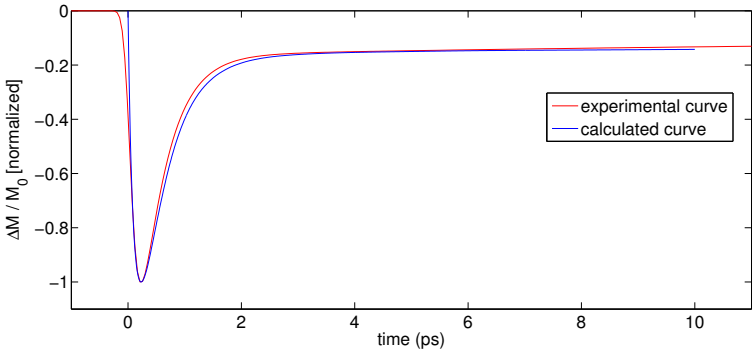

(c) R=25 ps^{-1} $\Delta T_{e,max}$=500 K

Figure 5.6: Blue line: Theoretical demagnetization curves in a Co/Pt ML on Pt/Si_3N_4 for different values of the R parameter and $\Delta T_{e,max}$. Red line: fitting function of experimental demagnetization curve acquired on the same sample.

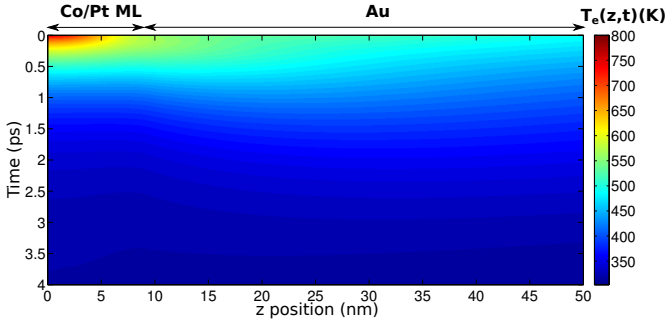

(a) Co/Pt ML on Au

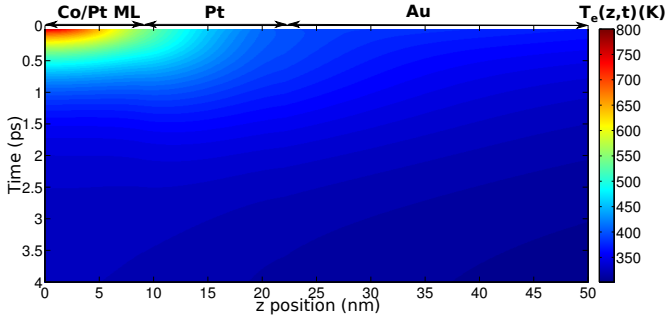

(b) Co/Pt ML on Pt/Au

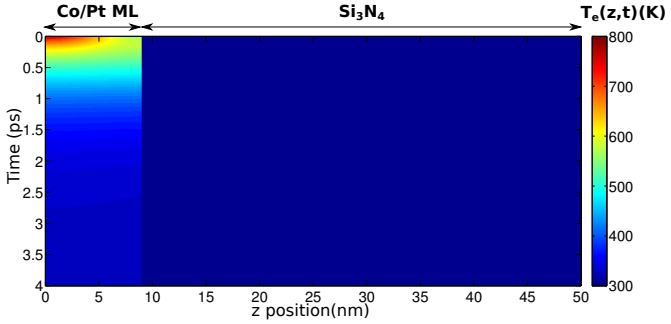

(c) Co/Pt ML on Si_3N_4

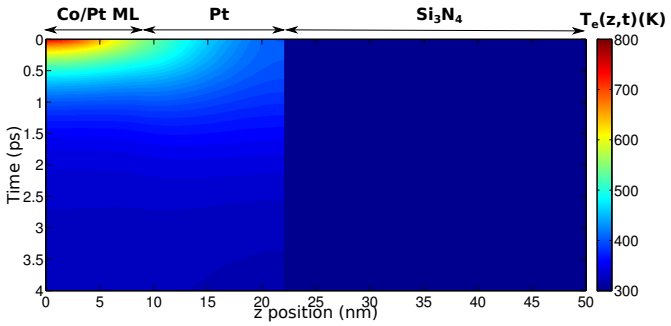

(d) Co/Pt ML on Pt/Si_3N_4

Figure 5.7: Electron distribution T_e(z,t) in all the different samples as calculated according to M3TM.

of the considerably lower electron phonon coupling constant than in Co/Pt. Even demagnetization amplitude is bigger in the sample on Au than in the others. This is more pronounced at high fluence. The Au electron conductivity is proportional to C_e, hence also to T_e. Therefore the conduction in Au increases at high fluences, giving a stronger effect.

5.4.3 Demagnetization time constants as a function of initial electron temperature

It has been highlighted that it is not straightforward to transfer the M3TM, optimized for bulk Co, to the case of a Co/Pt ML, with different T_C and different transport properties. Nonetheless, it is interesting to check if M3TM can give some hint on the behaviour of those samples.
In the present section M3TM is applied through equations 5.1, 5.2, 5.3 to the case of bulk Co. Here the M3TM has been validated by experimental results and the parameters have been deduced from them. Hence, it can be considered reliable. Results will no be fully comparable with our experimental results on a Co/Pt ML, however the procedure can be useful to infer trends, in particular regarding the behaviour of demagnetization time with fluence. The calculated curve $M(t)$ is analysed to infer demagnetization time constants. The curves obtained cannot be fitted with the function used for experimental curves, because the coupled equations are not solved by exponential functions. For this reason, demagnetization time τ_D is defined arbitrarily as the time interval during which the magnetization runs from the 80% to the 20% of its total reduction.
An interest lays on the behaviour of τ_D with fluence. Therefore each simulation is run for different values of $\Delta T_{e,max}$. In figure 5.8 τ_D as a function of $\Delta T^2_{e,max}$ in bulk Co as calculated by the M3TM is reported. $\Delta T^2_{e,max}$ is directly proportional to the pump fluence, as discussed above. Therefore the behaviour shown in figure 5.8 is directly comparable to the experimental behaviour of demagnetization time with pump fluence. τ_D increases linearly and then reaches a saturation, in accordance with experimental results, where the maximum is reached between $5\frac{mJ}{cm^2}$ and $6\frac{mJ}{cm^2}$ that means $\Delta T_{e,max} \approx 3250 - 3500$ K . For bulk Co the maximum at τ_D is for $\Delta T^2_{e,max} \approx 6 \times 10^6$ K^2, i.e. $\Delta T_{e,max} \approx 2500$ K smaller than in the ML experimental results. We remark once more that it is not possible to compare the absolute values, since the two systems are different, especially in the transport properties.
Demagnetization is faster in the samples with the additional Pt layer, than in the other

two. This is in accordance with the experimental results.
In this model the demagnetization rate follows to certain extent the electron temperature. In [25] a stronger demagnetization and a larger demagnetization time in the case of insulating substrates has been predicted compared to conducting substrates. For τ_D this is confirmed by the present calculation and it is true even for τ_M in experimental results (figure 5.5b), when results from the samples on Si_3N_4 and on Pt/Si_3N_4 are compared. Both in calculations and in experimental results (figure 5.4b), demagnetization is slower in the sample on Au than in the one on Pt. It must be reminded that Au does not favour heat dissipation and for this reason it has a role similar to the insulator. However, the model predicts a difference even between the insulating and the Au substrate, which is not found in experiments.

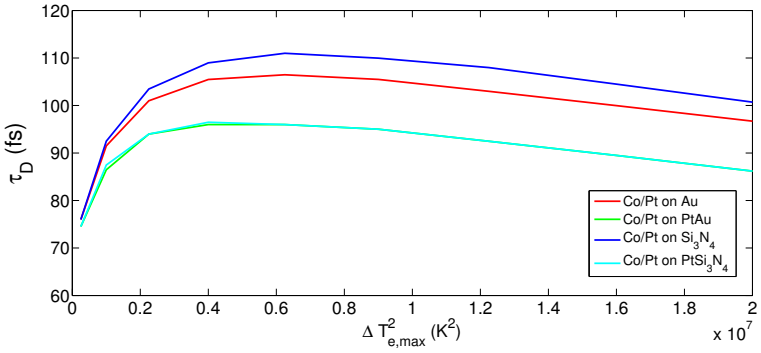

Figure 5.8: Demagnetization time obtained with the MatLab simulation for bulk Co grown on different substrates.

5.5 Conclusion

In this chapter the demagnetization process in Co/Pt ML grown on different substrates has been discussed. The fact that a demagnetization has been detected in the sample on insulator gives clear evidence that spin superdiffusion is not the only mechanism which drives the ultrafast demagnetization. The M3TM gives coupled equations that can be solved numerically to simulate demagnetization curves. The model and its parameters have been optimized in bulk Co and are not easily transferable to the case of Co/Pt ML. Nonetheless the solution for the electron temperature distribution gives an indication that explains why the remagnetization is faster in the sample with the additional Pt layer than in the samples without it. Pt is a sink that favours electrons heat dissipation,

on the contrary Au is a reservoir of "hot" electron and prevents equilibrium recovery, as well as the insulating substrate that cannot accept electrons.
The M3TM on bulk Co represents the experimental behaviour of demagnetization time with respect to the pump intensity. Here again the demagnetization is slower in the insulating substrate, as already predicted by Kuiper et al. in [25] and it is also slower in Au.
The discussion presented in this chapter gives valuable results, starting with the fact that superdiffusion is not the only mechanism present in ultrafast demagnetization. Subsequently, M3TM is used to explain experimental results and it gives motivation and prediction for them. However the discussion is not completed, firstly because it is still not clear how to transfer the M3TM equations to the case of a ML. Most importantly, both the mechanisms should be considered at the same time to explain results. There is the necessity to quantify their role and to develop a model which consider both.

Conclusions

The process of ultrafast demagnetization in optically excited ferromagnetic metals has intrigued solid-state physicists due to the complexity of the fundamental microscopic electron-phonon-spin interactions and for promising technological applications.
A unique and complete model which explains ultrafast magnetization dynamics has not been developed yet. The presently available models describing ultrafast demagnetization are too complicated to be satisfactorily described by an analytical function. In literature this has lead to a number of different functions used to describe and fit experimental data. Here, we analyse ultrafast demagnetization curves to infer demagnetization and remagnetization time constants. These parameters are very important to characterize the underlying demagnetization process. For this reason an analysis of these different models has been carried out in this work. All different functions found in literature are used to fit demagnetization curves acquired on the same sample in our experimental conditions. Noteworthy, the results change considerably according to which function is used, especially for demagnetization time constants. Furthermore, they change according to the temporal range in which the curves are analysed and are a function of excitation fluence. Hence, absolute values for time constants are expected to be unreliable and difficult to compare. Different results can be compared only if the same model has been used to obtain them, the fluence is well characterized and a sufficient temporal range is analysed.
Not only the macroscopic description of ultrafast demagnetization lacks a universally accepted model, but also the underlying microscopic processes responsible for the femtosecond loss of magnetization has not been achieved. The role played by spin-flip electron-phonon scattering and superdiffusive spin transport as microscopic mechanisms responsible for ultrafast demagnetization is indeed still being debated. The experimental results obtained in this work are aimed to contribute to this ongoing discussion.
The gold structured samples gave indications that spin superdiffusion does contribute

to the demagnetization process and hence is a process which is determined by the heterogeneity of the sample. The nano-structured gold grating on top the magnetic sample surface leads to a lateral excitation gradient, because the surface underneath the gold stripes are not excited. There is experimental evidence that this acts as an additional channel for spin diffusion and makes the demagnetization process faster compared to the process on the flat (unstructured) surface. Additionally the experimental results clearly demonstrate that the grating structure enhances the electric field and depend on the polarization of the excitation pulses.

Our experimental results on ultrathin Co/Pt multilayer (ML) grown on different substrates evidently show that superdiffusive spin transport cannot be the only mechanism which leads to ultrafast demagnetization. A significant demagnetization is detected for the sample on an insulating substrate, where all diffusion processes are inhibited. The experimental magnetization transients are then analysed according to the microscopic three temperature model (M3TM). Differential equations which describe the coupling of the electronic, phononic and spin degrees of freedom have been developed in the M3TM and are optimized for bulk Co. The numerical solution for our sample geometries are found to give the time evolution of the electron temperature, lattice temperature and magnetization. Unfortunately, it is found that the model cannot be easily transferred to the case of a Co/Pt ML and predict the time constants which describe the process within the M3TM framework. Nonetheless, some important aspects of this model can be used to understand the behaviour of the investigated samples. The calculated electron temperature evolution can explain the experimental remagnetization time, which is faster for the sample on Pt compared to the sample on Au and Si_3N_4, an insulator. This behaviour is due to a faster heat dissipation, i.e. a faster equilibrium recovery, in the sample on Pt compared to the other two.
Regarding the demagnetization time constants, M3TM, numerically solved for bulk Co, reproduces the behaviour of demagnetization time with respect to the excitation fluence. It also predicts a faster demagnetization in the samples on Pt compared to Au and Si_3N_4, as found in the experimental results. This means that also M3TM successfully describes the ultrafast demagnetization process.
This work gives interesting results regarding the microscopic mechanisms underlying the ultrafast dynamics in ferromagnetic metals excited by an optical femtosecond pulse. The presented experimental results, analysed considering the predictions of both the theories, give evidence for the coexistence of the superdiffusive spin transport and spin flip mechanism in ultrafast demagnetization. This seems to suggest that tailored sam-

ple geometries may lead to the domination of one mechanism over the other. The future efforts in ultrafast magnetism research should thus focus on the development of a model which includes both the microscopic mechanisms and to quantify the contribution of the two.

List of abbreviations

3TM Three Temperature Model

CP Circularly Polarized

FDTD Finite Difference Time Domain

FEL Free Electron Laser

FWHM Full Width Half Maximum

HAMR Heat Assisted Magnetic Recording

LCP Left Circularly Polarized

M3TM Microscopic Three Temperature Model

ML MultiLayer

MOKE Magneto-Optical Kerr Effect

NEQ Non Equilibrium

PEM Photo-Elastic Modulator

RCP Right Circularly Polarized

SOC Spin-Orbit Coupling

TR Time Resolved

XMCD X-ray Magnetic Circular Dichroism

Bibliography

[1] E. Beaurepaire, J.-C. Merle, A. Daunois, and J.-Y. Bigot, "Ultrafast Spin Dynamics in Ferromagnetic Nickel," *Physical Review Letters*, vol. 76, pp. 4250–4253, May 1996.

[2] T. Gerrits, H. a. M. Van Den Berg, J. Hohlfeld, L. Bär, and T. Rasing, "Ultrafast precessional magnetization reversal by picosecond magnetic field pulse shaping.," *Nature*, vol. 418, pp. 509–12, Aug. 2002.

[3] I. Tudosa, C. Stamm, a. B. Kashuba, F. King, H. C. Siegmann, J. Stöhr, G. Ju, B. Lu, and D. Weller, "The ultimate speed of magnetic switching in granular recording media.," *Nature*, vol. 428, pp. 831–3, Apr. 2004.

[4] B. Koopmans, H. Kicken, M. van Kampen, and W. de Jonge, "Microscopic model for femtosecond magnetization dynamics," *Journal of Magnetism and Magnetic Materials*, vol. 286, pp. 271–275, Feb. 2005.

[5] B. Koopmans, J. Ruigrok, F. Longa, and W. de Jonge, "Unifying Ultrafast Magnetization Dynamics," *Physical Review Letters*, vol. 95, p. 267207, Dec. 2005.

[6] B. Koopmans, G. Malinowski, F. Dalla Longa, D. Steiauf, M. Fähnle, T. Roth, M. Cinchetti, and M. Aeschlimann, "Explaining the paradoxical diversity of ultrafast laser-induced demagnetization.," *Nature Materials*, vol. 9, pp. 259–265, Mar. 2010.

[7] K. Carva, M. Battiato, D. Legut, and P. M. Oppeneer, "Ab initio theory of electron-phonon mediated ultrafast spin relaxation of laser-excited hot electrons in transition-metal ferromagnets," *Physical Review B*, vol. 87, p. 184425, May 2013.

[8] M. Battiato, K. Carva, and P. M. Oppeneer, "Superdiffusive Spin Transport as a Mechanism of Ultrafast Demagnetization," *Physical Review Letters*, vol. 105, p. 027203, July 2010.

[9] B. Pfau, S. Schaffert, L. Müller, C. Gutt, a. Al-Shemmary, F. Büttner, R. Delaunay, S. Düsterer, S. Flewett, R. Frömter, J. Geilhufe, E. Guehrs, C. M. Günther, R. Hawaldar, M. Hille, N. Jaouen, a. Kobs, K. Li, J. Mohanty, H. Redlin, W. F. Schlotter, D. Stickler, R. Treusch, B. Vodungbo, M. Kläui, H. P. Oepen, J. Lüning, G. Grübel, and S. Eisebitt, "Ultrafast optical demagnetization manipulates nanoscale spin structure in domain walls.," *Nature communications*, vol. 3, p. 1100, Jan. 2012.

[10] B. Vodungbo, J. Gautier, G. Lambert, A. B. Sardinha, M. Lozano, S. Sebban, M. Ducousso, W. Boutu, K. Li, B. Tudu, M. Tortarolo, R. Hawaldar, R. Delaunay, V. López-Flores, J. Arabski, C. Boeglin, H. Merdji, P. Zeitoun, and J. Lüning, "Laser-induced ultrafast demagnetization in the presence of a nanoscale magnetic domain network.," *Nature communications*, vol. 3, p. 999, Jan. 2012.

[11] E. Turgut, C. La-o vorakiat, J. M. Shaw, P. Grychtol, H. T. Nembach, D. Rudolf, R. Adam, M. Aeschlimann, C. M. Schneider, T. J. Silva, M. M. Murnane, H. C. Kapteyn, and S. Mathias, "Controlling the Competition between Optically Induced Ultrafast Spin-Flip Scattering and Spin Transport in Magnetic Multilayers," *Physical Review Letters*, vol. 110, p. 197201, May 2013.

[12] A. J. Schellekens, W. Verhoeven, T. N. Vader, and B. Koopmans, "Investigating the contribution of superdiffusive transport to ultrafast demagnetization of ferromagnetic thin films," *Applied Physics Letters*, vol. 102, no. 25, p. 252408, 2013.

[13] D. Rudolf, C. La-O-Vorakiat, M. Battiato, R. Adam, J. M. Shaw, E. Turgut, P. Maldonado, S. Mathias, P. Grychtol, H. T. Nembach, T. J. Silva, M. Aeschlimann, H. C. Kapteyn, M. M. Murnane, C. M. Schneider, and P. M. Oppeneer, "Ultrafast magnetization enhancement in metallic multilayers driven by superdiffusive spin current.," *Nature communications*, vol. 3, p. 1037, Jan. 2012.

[14] B. Koopmans, "Timeresolved Kerr effect and Spin Dynamics in Itinerant Ferromagnets," *Handbook of Magnetism and Advanced Magnetic Materials*, 2007.

[15] F. Dalla Longa, *Laser-induced magnetization dynamics in Co.* Phd thesis, Technische Universiteit Eidhoven, 2008.

[16] N. Kazantseva, U. Nowak, R. W. Chantrell, J. Hohlfeld, and a. Rebei, "Slow recovery of the magnetisation after a sub-picosecond heat pulse," *EPL (Europhysics Letters)*, vol. 81, p. 27004, Jan. 2008.

[17] C. Stamm, T. Kachel, N. Pontius, R. Mitzner, T. Quast, K. Holldack, S. Khan, C. Lupulescu, E. F. Aziz, M. Wietstruk, H. a. Dürr, and W. Eberhardt, "Femtosecond modification of electron localization and transfer of angular momentum in nickel.," *Nature materials*, vol. 6, pp. 740–3, Oct. 2007.

[18] C. Boeglin, E. Beaurepaire, V. Halté, V. López-Flores, C. Stamm, N. Pontius, H. a. Dürr, and J.-Y. Bigot, "Distinguishing the ultrafast dynamics of spin and orbital moments in solids.," *Nature*, vol. 465, pp. 458–61, May 2010.

[19] F. Dalla Longa, J. Kohlhepp, W. de Jonge, and B. Koopmans, "Influence of photon angular momentum on ultrafast demagnetization in nickel," *Physical Review B*, vol. 75, p. 224431, June 2007.

[20] A. Einstein and W. D. Haas, "Experimental proof of the existence of Ampere's molecular currents," Tech. Rep. September, Huygens Institute - Royal Netherlands Academy of Arts and Sciences (KNAW), Amsterdam, 1915.

[21] R. J. Elliott, "Theory of the Effect of Spin-Orbit Coupling on Magnetic Resonance in Some Semiconductors," *Physical Review*, vol. 96, pp. 266–279, Oct. 1954.

[22] F. Beuneu and P. Monod, "The Elliott relation in pure metals," *Physical Review B*, vol. 18, pp. 2422–2425, Sept. 1978.

[23] S. Blundell, *Magnetism in Condensed matter*. Oxford University Press, 2001.

[24] J. Fabian and S. Das Sarma, "Spin Relaxation of Conduction Electrons in Polyvalent Metals: Theory and a Realistic Calculation," *Physical Review Letters*, vol. 81, pp. 5624–5627, Dec. 1998.

[25] K. C. Kuiper, G. Malinowski, F. D. Longa, and B. Koopmans, "Nonlocal ultrafast magnetization dynamics in the high fluence limit," *Journal of Applied Physics*, vol. 109, no. 7, p. 07D316, 2011.

[26] A. Vaterlaus, T. Beutler, D. Guarisco, M. Lutz, and F. Meier, "Spin-lattice relaxation in ferromagnets studied by time-resolved spin-polarized photoemission," *Physical Review B*, vol. 46, pp. 5280–5286, Sept. 1992.

[27] A. Melnikov, H. Prima-Garcia, M. Lisowski, T. Gieß el, R. Weber, R. Schmidt, C. Gahl, N. Bulgakova, U. Bovensiepen, and M. Weinelt, "Nonequilibrium Magnetization Dynamics of Gadolinium Studied by Magnetic Linear Dichroism in

Time-Resolved 4f Core-Level Photoemission," *Physical Review Letters*, vol. 100, p. 107202, Mar. 2008.

[28] J. Hohlfeld, J. Güdde, U. Conrad, O. Dühr, G. Korn, and E. Matthias, "Ultrafast magnetization dynamics of Nickel," *Applied Physics B: Lasers and Optics*, vol. 68, pp. 505–510, Mar. 1999.

[29] M. Battiato, K. Carva, and P. M. Oppeneer, "Theory of laser-induced ultrafast superdiffusive spin transport in layered heterostructures," *Physical Review B*, vol. 86, p. 024404, July 2012.

[30] V. Zhukov, E. Chulkov, and P. Echenique, "Lifetimes and inelastic mean free path of low-energy excited electrons in Fe, Ni, Pt, and Au: Ab initio GW+T calculations," *Physical Review B*, vol. 73, p. 125105, Mar. 2006.

[31] V. Zhukov, E. Chulkov, and P. Echenique, "GW+T theory of excited electron lifetimes in metals," *Physical Review B*, vol. 72, p. 155109, Oct. 2005.

[32] M. Battiato, *Superdiffusive Spin Transport and Ultrafast Magnetization Dynamics*. Phd dissertation, Uppsala Universitet, 2013.

[33] M. Aeschlimann, M. Bauer, S. Pawlik, W. Weber, R. Burgermeister, D. Oberli, and H. Siegmann, "Ultrafast Spin-Dependent Electron Dynamics in fcc Co," *Physical Review Letters*, vol. 79, pp. 5158–5161, Dec. 1997.

[34] A. Goris, K. M. Döbrich, I. Panzer, a. B. Schmidt, M. Donath, and M. Weinelt, "Role of Spin-Flip Exchange Scattering for Hot-Electron Lifetimes in Cobalt," *Physical Review Letters*, vol. 107, p. 026601, July 2011.

[35] A. Eschenlohr, M. Battiato, P. Maldonado, N. Pontius, T. Kachel, K. Holldack, R. Mitzner, A. Föhlisch, P. M. Oppeneer, and C. Stamm, "Ultrafast spin transport as key to femtosecond demagnetization.," *Nature materials*, vol. 12, pp. 332–6, Apr. 2013.

[36] G. Malinowski, F. Dalla Longa, J. H. H. Rietjens, P. V. Paluskar, R. Huijink, H. J. M. Swagten, and B. Koopmans, "Control of speed and efficiency of ultrafast demagnetization by direct transfer of spin angular momentum," *Nature Physics*, vol. 4, pp. 855–858, Sept. 2008.

[37] R. P. Feynman, *The Feynman lectures on physics*, vol. Feynman R. Addison Wesley Longman, 1970.

[38] C.-Y. You and S.-C. Shin, "Generalized analytic formulae for magneto-optical Kerr effects," *Journal of Applied Physics*, vol. 84, no. 1, p. 541, 1998.

[39] J. Zak, E. Moog, C. Liu, and S. Bader, "Magneto-optics of multilayers with arbitrary magnetization directions," *Physical Review B*, vol. 43, pp. 6423–6429, Mar. 1991.

[40] J. Zak, E. Moog, C. Liu, and S. Bader, "Universal approach to magneto-optics," *Journal of Magnetism and Magnetic Materials*, vol. 89, no. 107, 1990.

[41] Z. Q. Qiu and S. D. Bader, "Surface magneto-optic Kerr effect," *Review of Scientific Instruments*, vol. 71, no. 3, p. 1243, 2000.

[42] P. Bruno, Y. Suzuki, and C. Chappert, "Magneto-optical Kerr effect in a paramagnetic overlayer on a ferromagnetic substrate: A spin-polarized quantum size effect," *Physical Review B*, vol. 53, pp. 9214–9220, Apr. 1996.

[43] H. Bennett and E. Stern, "Faraday Effect in Solids," *Physical Review*, vol. 137, pp. A448–A461, Jan. 1965.

[44] S. Polisetty, J. Scheffler, S. Sahoo, Y. Wang, T. Mukherjee, X. He, and C. Binek, "Optimization of magneto-optical Kerr setup: analyzing experimental assemblies using Jones matrix formalism.," *The Review of scientific instruments*, vol. 79, p. 055107, May 2008.

[45] W.-S. Kim, *Influence of interfaces on magnetization reversal and perpendicular magnetic anisotropy of Fe/Tb multilayers*. Phd thesis, Universitaet Dusburg Essen, 1998.

[46] M. van Kampen, *Ultrafast spin dynamics in ferromagnetic metals*. Phd thesis, Technische Universiteit Eindhoven, 2003.

[47] R. Schoenlein, W. Lin, J. Fujimoto, and G. Eesley, "Femtosecond studies of nonequilibrium electronic processes in metals," *Physical Review Letters*, vol. 58, pp. 1680–1683, Apr. 1987.

[48] L. Guidoni, E. Beaurepaire, and J.-Y. Bigot, "Magneto-optics in the Ultrafast Regime: Thermalization of Spin Populations in Ferromagnetic Films," *Physical Review Letters*, vol. 89, p. 017401, June 2002.

[49] H. Stillrich, C. Menk, R. Fromter, and H. P. Oepen, "Magnetic anisotropy and the cone state in Co/Pt multilayer films," *Journal of Applied Physics*, vol. 105, no. 7, p. 07C308, 2009.

[50] G. Daalderop, P. Kelly, and M. Schuurmans, "First-principles calculation of the magnetic anisotropy energy of (Co)n/(X)m multilayers," *Physical Review B*, vol. 42, pp. 7270–7273, Oct. 1990.

[51] M. Kryder, E. Gage, T. McDaniel, W. Challener, R. Rottmayer, and M. Erden, "Heat Assisted Magnetic Recording," *Proceedings of the IEEE*, vol. 96, pp. 1810–1835, Nov. 2008.

[52] J. Hohlfeld, J. Müller, S.-S. Wellershoff, and E. Matthias, "Time-resolved thermoreflectivity of thin gold films and its dependence on film thickness," *Applied Physics B: Lasers and Optics*, vol. 64, pp. 387–390, Mar. 1997.

[53] H. van Kesteren and W. Zeper, "Controlling the Curie temperature of Co/Pt multilayer magneto-optical recording media," *Journal of Magnetism and Magnetic Materials*, vol. 120, pp. 271–273, Mar. 1993.

[54] D. R. Lide, *CRC Handbook of Chemistry and Physics*. CRC Press, 89th ed., 2008.

[55] J. Hohlfeld, S. Wellershoff, J. Güdde, U. Conrad, V. Jähnke, and E. Matthias, "Electron and lattice dynamics following optical excitation of metals," *Chemical Physics*, vol. 251, pp. 237–258, Jan. 2000.

[56] "refractiveindex.info."